

Search for Beyond the Standard Model signals in a  
quark-gluon tagged dijet final state with the ATLAS  
detector



Ben Whitmore  
Department Of Physics  
Lancaster University

A thesis submitted for the degree of Doctor of  
Philosophy

September 2019

## **Abstract**

A study into the impact of quark-gluon tagging on a dijet search was performed using simulated dijet invariant mass spectra from the ATLAS detector. Monte Carlo simulations were compared to data from the 2015-2018 data taking periods. The analysis covered a mass range between 2 TeV and 7 TeV and found improvements to the expected 95% CL upper mass limits for a singlet scalar model decaying to a gluon-gluon final state in the region of  $\sim 30\%$  at 4.5 TeV compared to an untagged search. Improvements to an excited quark model of  $\sim 10\%$  were obtained for a mass above 6 TeV.

## Acknowledgements

Special thanks should obviously go to my supervisor, Iain Bertram, who helped both with all of the technical aspects of this thesis, and was also kind enough to keep me informed of the cricket score whenever Australia were winning.

Also of great help were the discussions and meetings with Ben Nachman, who was a constant source of insight into the ongoing quark-gluon tagging studies.

On the Dijet team, both Ben Allen and Nishu were invaluable contacts. Ben actually suggesting the topic for this thesis. It was especially helpful to have people to go to whenever SWIFT proved disagreeable.

Closer to home, thanks, and I suppose encouragement, should go to Katherine Rybacki and Neža Ribaric. Both already know at least as much ATLAS physics as I do, and if I can complete a thesis, they certainly can. Just try to forget about the various git comments I wrote, you can both do better.

Also thanks to all my friends/fellow Spanish Inquizitors in Lancaster and Geneva, who can't begin to appreciate my gratitude. Special thanks to Charlotte Owen and Adam Lister, who started at the same time as me, and naturally finished much earlier. In a similar sentiment, I would also like to thank Kevin, and Lancaster Brewery for all their resolute support over the years. I couldn't have done this without them.

## Declaration of Authorship

This thesis is a presentation of original research performed by the author. It has not been previously submitted for the award of a higher degree.

The work presented in this thesis was ultimately made possible by a large number of ATLAS collaborators. The specific contributions of the author are summarised below:

- The specific implementation of quark-gluon tagging using the track multiplicity used in this thesis, and development of specific selections.
- Generation and presentaion of SWIFT backgrounds relating specifically to quark-gluon tagging.
- Kinematic comparisons between data and MC, Figures 4.13-4.16, for both the tagged and untagged samples.
- Generation of expected significance plots, following work of my supervisor, Iain Bertram.
- Comparisons between signal models and QCD, presented in chapter 6. All figures except 6.1 in section 6.1. Section 6.2 represents external work.
- Generation of limit comparisons between tagged and untagged samples.

# List of Figures

2.1	Feynman diagrams contributing to $q^*$ production . . . . .	7
2.2	Gauge interactions of light and excited fermions. . . . .	9
2.3	Transitions between ordinary and excited fermions via gauge-boson emission. From [1]. . . . .	9
2.4	Feynman diagrams contributing to $q^*$ production . . . . .	10
2.5	Invariant mass distributions $d\sigma/dm$ of excited quarks in the jet-jet channel . . .	11
2.6	The formation of two jets from a parton collision. . . . .	14
2.7	Hadronisation Models. . . . .	15
2.8	Illustration of collinear safety . . . . .	18
2.9	Configurations illustrating IR unsafety . . . . .	18
2.10	An example parton-level event clustered with four different jet algorithms. . . .	21
2.11	The formation of two jets from qq, qqg initiating partons. . . . .	23
3.1	Cumulative luminosity delivered, recorded and certified good quality by ATLAS in 2015-2018. . . . .	27
3.2	Cut-away view of the ATLAS detector. . . . .	29
3.3	EM Calorimeter barrel module schematic . . . . .	33
3.4	Cut-away view of the ATLAS liquid argon calorimeters. . . . .	34
3.5	ATLAS tile calorimeter module schematic . . . . .	36

3.6	Flow diagram of the readout signal path of the different TileCal calibration systems [2]. . . . .	39
4.1	Trigger efficiencies and their corresponding fits for HLT_j420 and HLT_j225_gsc420_boffperf_split triggers, 2018 data . . . . .	44
4.2	Calibration stages for EM-scale jets. . . . .	48
4.3	Average energy response and $\eta$ difference between truth and reconstructed jets . . . . .	51
4.4	The average jet response in MC simulation as a function of the GSC variables for three ranges of truth jet $p_T$ . . . . .	54
4.5	The average jet response in MC simulation as a function of the GSC variables for three ranges of truth jet $p_T$ . . . . .	55
4.6	Combined data-to-MC EM+JES jet response ratio for Z+jet, $\gamma$ +jet, and multijet channels. . . . .	57
4.7	Combined uncertainty of fully calibrated jets in the JES . . . . .	61
4.8	Variables used in the bi-sector technique . . . . .	63
4.9	Distributions of (a) $\langle Q \rangle$ , (b) $f_Q^{LAr}$ , (c) $f_Q^{HEC}$ and (d) $E_{neg}$ for good jets in 2015 data (black points), simulation (blue histogram) and a fake jet enriched sample from 2015 data (red points) [3]. . . . .	71
4.10	Distributions of (a) $f_{EM}$ , (b) $f_{HEC}$ , and (c) $f_{max}$ for good jets in 2015 data (black points), simulation (blue histograms) and a fake jet enriched sample from 2015 data (red points) [3]. . . . .	72
4.11	Distributions of (a) $f_{ch}$ and (b) $f_{ch} / f_{max}$ is very efficient for $ \eta  < 2.4$ in the good jets enriched sample for both data (black points) and simulation (blue histograms). Distributions from the fake jet enriched samples are also superimposed (red points). From Ref [3]. . . . .	73
4.12	Distribution of $f_{ch}$ as a function of the electromagnetic fraction ( $f_{EM}$ ) for (a) good jets and (b) fake jet enriched samples in data. From Ref [3]. . . . .	74
4.13	Data/MC comparisons . . . . .	75

4.14	Data/MC comparisons . . . . .	76
4.15	Data/MC comparisons for several event variables: (a) number of jets, (b) number of primary vertices, (c) rapidity boost, and (d) the angular separation of the two jets, $y^*$ . . . . .	77
4.16	Data/MC comparisons of charged track multiplicity for (a) & (b) QQ, (c) & (d) QG and (e) & (f) GG tagged events, both leading and sub-leading jets. . . . .	78
5.1	Global fits with 3-, 4-, and 5-parameter functions . . . . .	82
5.2	Bin-by-bin construction of the SWIFT background . . . . .	84
6.1	Distribution of the jet reconstructed track multiplicity ( $n_{\text{track}}$ ) in different $p_T$ ranges	87
6.2	Simulated dijet samples produced using the Pythia 8 generator . . . . .	89
6.3	Simulated 4.5 TeV Excited Quark sample . . . . .	90
6.4	Truth $n_{\text{Track}}$ distributions at different ranges of $p_T$ between 500 and 1200 GeV from QCD MC samples . . . . .	91
6.5	Truth $n_{\text{Track}}$ distributions at different ranges of $p_T$ between 1200 and 6000 GeV from QCD MC samples . . . . .	92
6.6	Truth $n_{\text{Track}}$ distribution in all $p_T$ bins for QCD . . . . .	93
6.7	Truth $n_{\text{Track}}$ distributions at a range of $p_T$ from the excited quark MC samples, 1000-4000 GeV . . . . .	94
6.8	Truth $n_{\text{Track}}$ distributions at a range of $p_T$ from the excited quark MC samples, 4500-7000 GeV . . . . .	95
6.9	The expected significance for a $H'$ for values of $\epsilon_{g\mathbf{G}}$ from 0.9 to 0.3 compared to the significance with no selection applied. . . . .	97
6.10	The expected significance for a $q^*$ compared to the significance with no selection applied. . . . .	99
6.11	The expected significance for a $q^*$ compared to the significance with no selection applied where no selection is required on the gluon jet. . . . .	100

6.12	The $n_{\text{track}}$ distribution of truth Quark jets (blue) and truth Gluon jets (red) for QCD (solid line) compared to a 5 TeV $H'$ signal (solid markers). . . . .	101
6.13	The $n_{\text{track}}$ distribution of truth Quark jets (blue) and truth Gluon jets (red) for QCD (solid line) compared to a 5 TeV $q^*$ signal (solid markers). . . . .	102
6.14	The $n_{\text{track}}$ distribution of truth Quark jets (blue) and truth Gluon jets (red) for QCD (solid line) compared to a 5 TeV $Z'$ signal (solid markers). . . . .	102
6.15	(a) Simulated jet fractions as a function of jet $p_T$ , (b) average charged track multiplicity as a function of jet $p_T$ . . . . .	104
6.16	An illustration of the closure test from the central-forward method for jets with $p_T \lesssim 50$ GeV . . . . .	105
6.17	The systematic uncertainties on the particle-level charged particle distribution for a 60% quark jet efficiency working point. From Ref [4]. . . . .	106
6.18	A comparison of the particle-level charged particle multiplicity for the more forward jet from data and PYTHIA 8 with the A14 and AZNLO tunes from Ref. [4]. The data and uncertainties are from Ref. [5] via HEPData [6]. . . . .	107
6.19	Experimental systematic uncertainties on the track reconstruction for the 60% quark jet efficiency working point of the quark-gluon tagger. From Ref. [4] . . . .	109
6.20	The total systematic uncertainty for the 60% quark jet efficiency working point for the quark-gluon tagger for (a) gluon jets and (b) quark jets. From Ref. [4] . .	110
7.1	Data/MC comparison of $m_{jj}$ distributions for the Sel1 selection . . . . .	115
7.2	SWIFT background from PYTHIA, JJ sample . . . . .	116
7.3	$\sigma \times A \times \text{BR}$ limits for $q^*$ signal . . . . .	117
7.4	Ratio of $\sigma \times A \times \text{BR}$ limits for $q^*$ signal . . . . .	117
7.5	$\sigma \times A \times \text{BR}$ limits for $H'$ signal . . . . .	119
7.6	Ratio of $\sigma \times A \times \text{BR}$ limits for $H'$ signal . . . . .	120

# List of Tables

2.1	The bosons of the standard model . . . . .	4
2.2	The fermions of the Standard Model . . . . .	5
3.1	Selected LHC parameters for pp collisions at $\sqrt{s} = 13$ TeV in 2015 - 2018. . . . .	26
3.2	Geometry of the ATLAS calorimeter system. . . . .	37
4.1	Parameters used to build the two types of topological cluster available in the standard ATLAS reconstruction. . . . .	46
4.2	The five observables used to improve the resolution of the JES. . . . .	52
4.3	Summary of the systematic uncertainties in the JES from in situ calibration. . . . .	58
4.4	Additional systematic uncertainties in the JES . . . . .	60
4.5	Jet selection criteria used in this analysis . . . . .	68
6.1	The efficiency for truth quark or gluon jets being selected by the <b>Q (G)</b> selection $\epsilon_{q\mathbf{Q}}, \epsilon_{g\mathbf{Q}}$ ( $\epsilon_{qG}, \epsilon_{gG}$ ). . . . .	96
6.2	The efficiency for truth quark or gluon jets being selected by the <b>Q (G)</b> selection $\epsilon_{q\mathbf{Q}}, \epsilon_{g\mathbf{Q}}$ ( $\epsilon_{qG}, \epsilon_{gG}$ ). . . . .	98

# Contents

<b>List of Figures</b>	<b>iv</b>
<b>List of Tables</b>	<b>viii</b>
<b>Contents</b>	<b>ix</b>
<b>1 Introduction</b>	<b>1</b>
<b>2 Theoretical Motivation and Background</b>	<b>3</b>
2.1 The Standard Model . . . . .	3
2.2 Benchmark Signals . . . . .	6
2.3 Jet Phenomenology . . . . .	12
<b>3 The ATLAS Detector</b>	<b>24</b>
3.1 CERN and the Large Hadron Collider . . . . .	24
3.2 The ATLAS Detector . . . . .	27
<b>4 Data Quality</b>	<b>42</b>
4.1 Triggering . . . . .	42
4.2 Event Selection . . . . .	43
4.3 JET Reconstruction and Calibration . . . . .	45
4.4 Jet energy resolution uncertainties . . . . .	60
4.5 Jet Cleaning . . . . .	62

4.6	Quality Cuts . . . . .	66
4.7	Monte Carlo Samples . . . . .	67
4.8	Data MC comparisons . . . . .	69
<b>5</b>	<b>SWiFt: Fitting the Background</b>	<b>79</b>
5.1	Pseudo Data . . . . .	79
5.2	SWiFt . . . . .	81
<b>6</b>	<b>Signal Selection: Quark-Gluon Tagging</b>	<b>86</b>
6.1	Tagging . . . . .	86
6.2	Systematic Uncertainties . . . . .	103
<b>7</b>	<b>Limit Setting</b>	<b>111</b>
7.1	Limit Setting . . . . .	111
7.2	Results . . . . .	114
<b>8</b>	<b>Conclusion</b>	<b>121</b>
	<b>Bibliography</b>	<b>123</b>

# Chapter 1

## Introduction

Modern particle physics theory has been astonishingly successful at explaining and predicting a range of observations from experiments. In order to further test the limits of theory, new techniques, more data, and higher energies are required. Physicists hope that by testing our current understanding in this way, extensions to the theory can be found that will help to explain what is currently unaccounted for.

The Large Hadron Collider (LHC) provides unprecedented energies and statistics for particle physics researchers, allowing us hope that in coming years clues can be found which will guide us by uncovering more fundamental laws of nature. Already, the LHC and two of its general purpose detectors, ATLAS and CMS, have validated our understanding of the Higgs mechanism, by discovering the particle (the Higgs Boson) associated with the Higgs scalar field. Since this discovery, these detectors have been accumulating more data, allowing us to probe more sensitively for new physics.

The most abundant final state objects produced in proton-proton collisions in the ATLAS detector are collimated sprays of particles called jets. These objects are the result of colored partons, either quarks or gluons, being produced in the collisions. Chapter 2 will introduce the theoretical background of how jets are produced, as well as two theoretical models which produce final states likely to benefit most from the techniques introduced in this thesis to

discriminate between the two types of initiating parton.

The LHC and ATLAS detector are described in Chapter 3, with special focus on those areas of the detector important for the detection of jets. Chapter 4 will describe the methods used to calibrate the signals in the detector, and compare the simulated data samples to kinematic variables obtained from data. Background estimation techniques are described in Chapter 5, and the actual process of distinguishing quark- and gluon-initiated jets is explained in Chapter 6. The statistical work involved in setting cross section limits on the two benchmark signals used, and the results obtained from this work is discussed in Chapter 7. Finally, conclusions from this work, and discussion of next steps are outlined in Chapter 8.

## Chapter 2

# Theoretical Motivation and Background

### 2.1 The Standard Model

Modern particle physics theory is encapsulated in the Standard Model. The Standard Model is a theoretical framework which describes 3 of the 4 fundamental forces and their interactions with the known particles. Several phenomena are unaccounted for in the Standard Model, including the indirect observation of Dark Matter, neutrino masses, and the observed matter antimatter asymmetry.

#### The Standard Model

The Standard Model describes the interactions of the Strong, Weak and Electromagnetic forces. It is a quantum field theory belonging to the gauge group  $U(1)_Y \times SU(2)_L \times SU(3)$ .

Force carrying particles (bosons) arise as the generators of each group, and possess integer spin. These are the particles which mediate interactions. The  $U(1)_Y$  and  $SU(2)_L$  groups have associated fields  $B_\mu(x)$  and  $W_\mu^a(a = 1, 2, 3)$  respectively.  $L$  reflects the experimental observation that only left handed particles have been observed to be members of the group.

Force	Boson(s)	Charge
Electromagnetic	$\gamma$	none
Weak Nuclear	$W^\pm$	weak, electromagnetic
	$Z$	weak
Strong	$g$	colour

Table 2.1: The force carrying particles (bosons) in the Standard Model.

Additional quantum numbers are the weak hypercharge,  $Y$ , and weak isospin,  $T$ . The third component of weak isospin,  $T_3$  is conserved in weak, strong and electromagnetic interactions, but not in interactions with the Higgs field, discussed below. The combination  $Q = T_3 + \frac{1}{2}Y$  is conserved.

These fields are not observed in isolation, instead a linear combination forms the familiar particles of electromagnetism - the photon, and weak nuclear force - the  $W$  and  $Z$  particles.

The third group,  $SU(3)$ , corresponds to the strong nuclear force with *colour* as its quantum number. The generators of this group are the gluons,  $A_\mu^{\alpha=1\dots 8}$ . The strong and electroweak forces are not unified, and so the full Standard Model can be separated into two components,  $U(1)_Y \times SU(2)_L$ , and  $SU(3)$ .

Gravity is not accounted for in the Standard Model.

The other category of fundamental particle is the *fermion*, the constituents of matter, which possess half integer spin. These are subdivided into those which interact via the strong nuclear force, *quarks*, and *leptons*, which do not. A further subdivision can be made between the charged leptons - the electron ( $e$ ), muon ( $\mu$ ), and tau ( $\tau$ ) - and the neutrinos -  $\nu_e$ ,  $\nu_\mu$ , and  $\nu_\tau$ . The neutrinos are electrically neutral,  $Q = 0$ , the electron, muon and tau do carry electric charge,  $Q = -1$  and their corresponding anti-particles a charge of  $Q = +1$ .

The fermions are arranged into three families, following the observation that weak decays preserve this family number.

Quarks possess electric charges of  $+2/3$  or  $-1/3$  (and their corresponding anti-quarks have

$Q = -2/3$  or  $+1/3$ ). Quarks also possess colour, interacting with the strong nuclear force. Families of quark contain two different types, or flavours: up (u) and down (d) in the first, charm (c) and strange (s) in the second, and top (t) and bottom (b) in the third. Table 2.2 summarises the fermions.

	1 <sup>st</sup>	2 <sup>nd</sup>	3 <sup>rd</sup>	T	T <sub>3</sub>	Y	Q	C
Quarks	$u_L$	$c_L$	$t_L$	1/2	+1/2	+1/3	+2/3	r,g,b
	$d_L$	$s_L$	$b_L$	1/2	-1/2	+1/3	-1/3	r,g,b
	$u_R$	$c_R$	$t_R$	0	0	+4/3	+2/3	r,g,b
	$d_R$	$s_R$	$b_R$	0	0	-2/3	-1/3	r,g,b
Leptons	$e_L$	$\mu_L$	$\tau_L$	1/2	-1/2	-1	-1	none
	$\nu_{e,L}$	$\nu_{\mu,L}$	$\nu_{\tau,L}$	1/2	+1/2	-1	0	none
	$e_R$	$\mu_R$	$\tau_R$	0	0	-2	-1	none

Table 2.2: The fermions of the standard model with their quantum numbers.

The Standard Model contains an additional scalar boson, the Higgs, which is a consequence of the Higgs mechanism, which explains the masses of the other gauge bosons and fermions. The Higgs boson is not a force carrier, but arises from symmetry breaking of the electroweak sector. This symmetry breaking splits the massless gauge bosons of the underlying symmetry into the massless photon and the massive W and Z bosons, separating the electromagnetic and weak components of the theory.

### Beyond the Standard Model

Despite the success of the Standard Model in accounting for the forces of nature and their interactions with the familiar forms of matter, we lack a complete understanding of nature. Measurements of galactic rotation speeds in 1970 suggested more mass was present in galaxies than could be directly detected [7]. Dark Matter (DM) is a proposed solution - a form of matter which interacts via gravity, but very weakly or not at all with the electromagnetic force. This explains why direct visual observations of galaxies fail to detect the extra mass, while also allowing for the possibility that DM interacts sufficiently for detectors such as ATLAS.

If DM particles are subject to the strong nuclear force, there is a finite probability of their creation in collisions such as those taking place in the ATLAS detector, and subsequent decay into a dijet final state. Several theoretical candidates are proposed for such DM particles, and the dijet search allows for cross section limits to be placed on these benchmark models.

## 2.2 Benchmark Signals

### Excited Quarks

The existence of three generations of quarks and leptons has motivated speculation that these particles may not be fundamental, but instead exist as composite structures. These structures would be identified as bound states of more fundamental constituents called *preons* [8]. A common assumption underlying composite models is that there exists a new strong gauge interaction, sometimes called metacolor. It is speculated that a non-Abelian metacolor theory should be both asymptotically free and infrared-confining. Below a characteristic energy scale,  $\Lambda^*$ , this interaction is sufficiently strong to bind the preons into metacolor-singlets, identifiable as the observed quarks and leptons. This theory can be seen as a natural extension to technicolor models of composite Higgs scalars.

Composite models of quarks and leptons generally predict the existence of excited states. Production and decay of excited quarks ( $q^*$ ) via gauge interactions would provide a signal potentially accessible to the dijet resonance search. A variety of mechanisms have been proposed for excited quark production at p-p colliders. The most obvious of these is quark-antiquark annihilation or gluon-gluon fusion, however predicted cross sections from these processes are so small that any potential signal is likely to be hidden in the ordinary QCD and electroweak background. Alternatively, production via gluonic excitation of quarks, or even through contact interactions provides an alternative mechanism with larger corresponding cross sections. These mechanisms are shown in Figure 2.1.

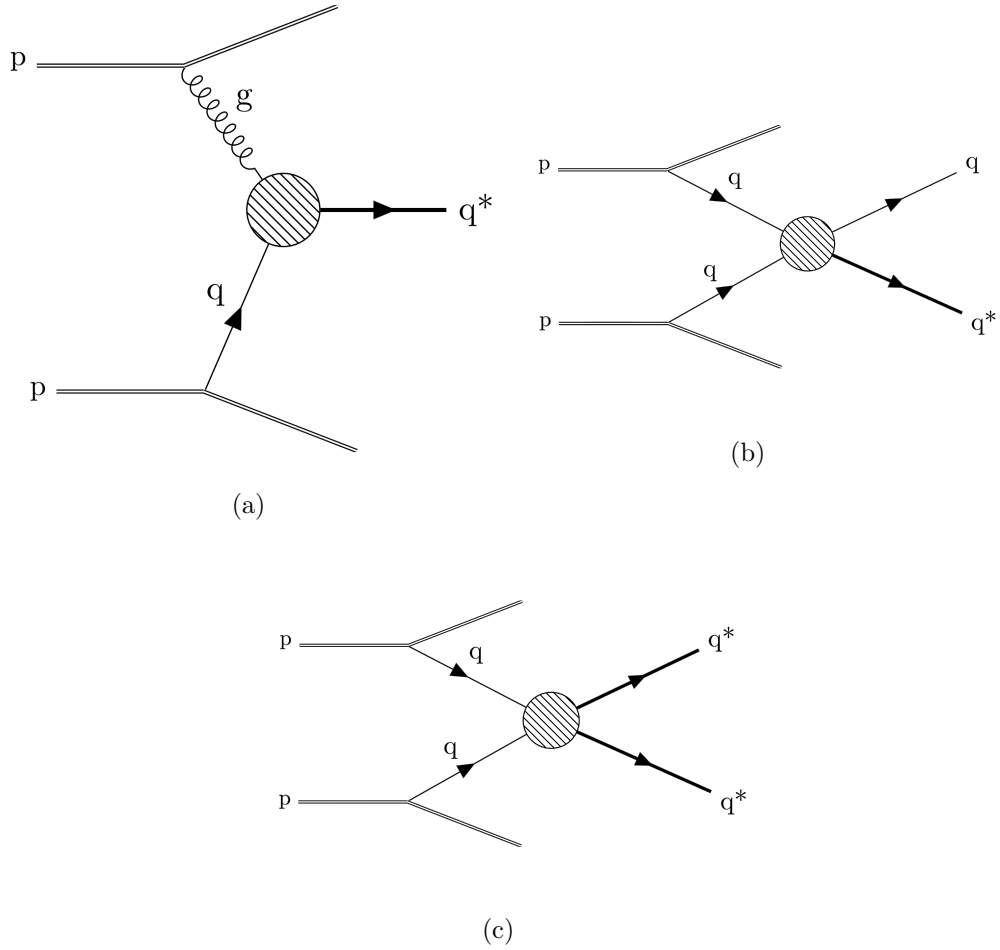


Figure 2.1: Generic diagrams contributing to  $q^*$  production in hadronic collisions: (a) quark gluon fusion, (b)  $qq^*$  production via contact interactions, and (c)  $q^*$  pair production via contact interactions.

$$q + \bar{q} \rightarrow q^* + \bar{q} \quad (2.1)$$

$$g + g, g + q \rightarrow q^* \quad (2.2)$$

$$q + q \rightarrow q^* + q \quad (2.3)$$

Such excited quarks are expected to decay to quarks and gluons via gauge interactions, and hence to produce multi-jet final states. These decays have provided a common benchmark

signal for dijet searches in the past [9]. The theoretical models behind their production and decay are described in detail in [1, 10].

Here, the  $qg \rightarrow q^*$  production model is used, assuming the excited quark possesses spin and isospin  $= \frac{1}{2}$  and quark-like SM coupling constants. These assumptions are made for simplicity - there are no theoretical constraints preventing the lowest lying excited quark having, for instance spin  $\frac{3}{2}$  and an isospin other than  $\frac{1}{2}$  [10].

The assignment of all excited states to isosinglets allows for non-zero masses prior to  $SU(2) \times U(1)$  symmetry breaking. This can also be achieved by the assignment of left- and right-handed components to isodoublets,

$$\begin{bmatrix} u \\ d \end{bmatrix}_L, \begin{matrix} u_R \\ d_R \end{matrix}, \begin{bmatrix} u^* \\ d^* \end{bmatrix}_L, \begin{bmatrix} u^* \\ d^* \end{bmatrix}_R \quad (2.4)$$

The coupling of excited quark states  $u^*, d^*$ ... to gluons, photons,  $W^\pm$  and the Z is vectorlike (Figure 2.2), and given by the Lagrangian:

$$L_{gauge} = \bar{f}^* \gamma^\mu \left[ g_s \frac{\lambda^a}{2} G_\mu^a + g \frac{\tau}{2} \cdot W_\mu + g' \frac{Y}{2} B_\mu \right] f^* \quad (2.5)$$

The weak hypercharge  $Y$  of the excited states is  $\frac{1}{3}$  for the quarks,  $g_s$ ,  $g = e/\sin \theta_W$  and  $g' = e/\cos \theta_W$  are the strong and electroweak gauge couplings.  $\sin \theta_W$  is the weak mixing angle, the angle by which spontaneous symmetry breaking rotates the W and B fields.  $G_\mu^a$ ,  $W_\mu$ , and  $B_\mu$  describe the gluon, the  $SU(2)$ , and the  $U(1)$  gauge fields. Each of the vertices can be modified by form factors.

Additionally, gauge bosons can mediate transitions between the left-handed ground state, and right-handed excited state fermions (Figure 2.3). The form of the effective Lagrangian is fixed by gauge invariance to be of magnetic-moment type:

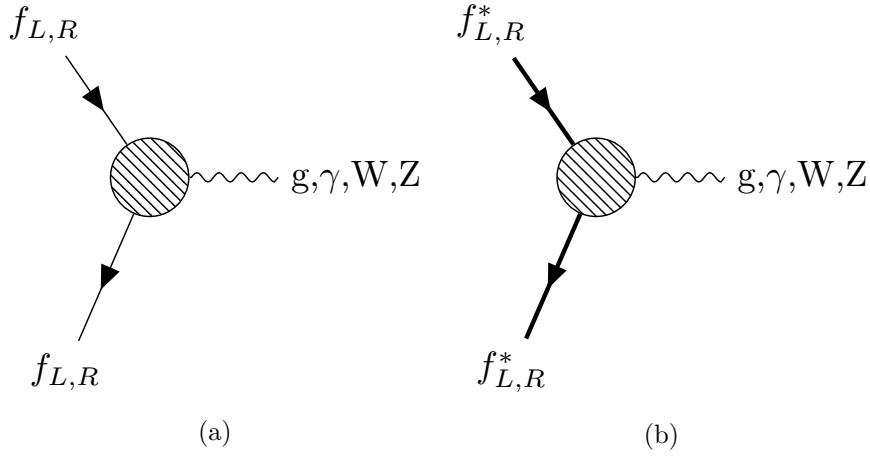


Figure 2.2: Gauge interactions of light and excited fermions. The W boson couples to left- and right-handed excited fermions, but only to left-handed ordinary fermions.

$$L_{\text{trans}} = \frac{1}{2\Lambda} \bar{f}_R^* \sigma^{\mu\nu} \left[ g_s f_s \frac{\lambda^a}{2} G_{\mu\nu}^a + g f \frac{\tau}{2} \cdot W_{\mu\nu} + g' f' \frac{Y}{2} B_{\mu\nu} \right] f_L + H.C. \quad (2.6)$$

where  $G_{\mu\nu}^a$ ,  $W_{\mu\nu}$ , and  $B_{\mu\nu}$  are the field strength tensors of the gluon, the SU(2), and the U(1) gauge fields respectively.  $f_s$ ,  $f$ , and  $f'$  are parameters determined by the composite dynamics, naively expected to be of order 1. These factors can be changed to form factors,  $f_s(q^2)$ ,  $f(q^2)$ , and  $f'(q^2)$  to incorporate higher-dimensional operators.  $\Lambda$  is the compositeness scale.

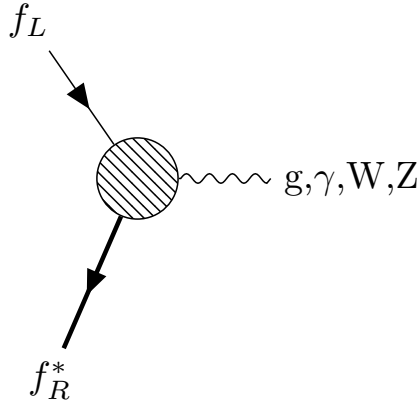


Figure 2.3: Transitions between ordinary and excited fermions via gauge-boson emission. From [1].

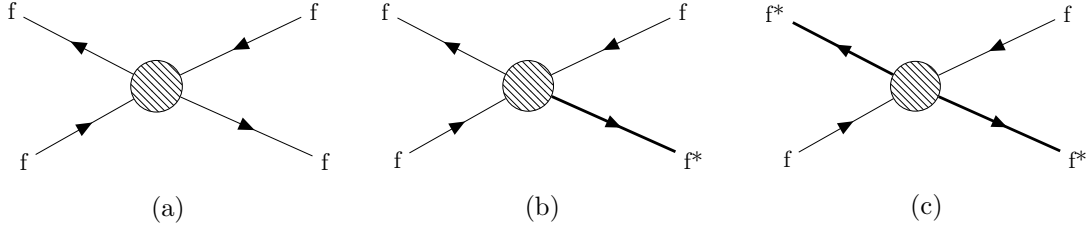


Figure 2.4: Generic diagrams contributing to  $q^*$  production in hadronic collisions: (a) quark gluon fusion, (b)  $qq^*$  production via contact interactions, and (c)  $q^*$  pair production via contact interactions.

Contact interactions such as those in Figure 2.4 provide an additional production mechanism, resulting from novel strong preon interactions. Below the compositeness scale,  $\Lambda$ , they are described by an effective four-fermion Lagrangian of the form

$$L_{\text{contact}} = \frac{g_*^2}{\Lambda^2} \frac{1}{2} j^\mu j_\mu \quad (2.7)$$

with

$$j_\mu = \eta_L \bar{f}_L \gamma_\mu f_L + \eta'_L \bar{f}_L^* \gamma_\mu f_L^* + \eta''_L \bar{f}_L^* \gamma_\mu f_L + H.C. \quad (2.8)$$

$$\eta_R \bar{f}_R \gamma_\mu f_R + \eta'_R \bar{f}_R^* \gamma_\mu f_R^* + \eta''_R \bar{f}_R^* \gamma_\mu f_R + H.C.$$

Such interactions would be expected to produce multijet signatures (see Figure 2.4), and so are not directly relevant in the dijet search. Quark-gluon tagging techniques may provide benefits to such searches in future however.

Since current limits on the  $q^*$  mass place it much higher than the mass of the electroweak gauge bosons, the dominant branching ratio is via the strong force to a SM quark and a gluon.

$$q^* \rightarrow q + g \quad (2.9)$$

$$\Gamma(q^* \rightarrow qg) = \frac{1}{3} \alpha_s f_s^2 \frac{m^{*3}}{\Lambda^2}. \quad (2.10)$$

The  $jj$  mass distributions for various  $q^*$  masses are shown in Figure 2.5

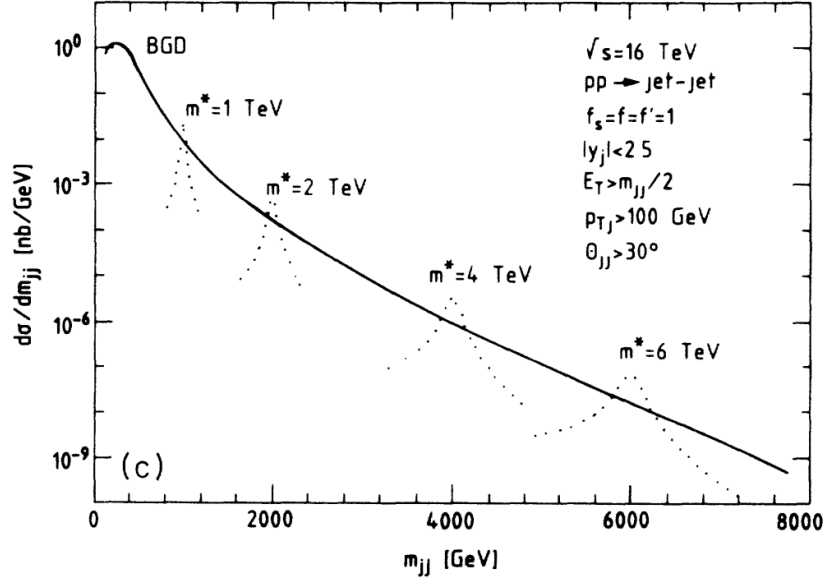


Figure 2.5: Invariant mass distributions  $d\sigma/dm$  of excited quarks in the jet-jet channel for various values of  $m^*$  (dotted lines) and  $pp$  collisions at  $\sqrt{s} = 16$  TeV. The solid curve represents the Standard Model background. From [1].

### Singlet Scalar decaying to two gluons

Several BSM models predict the existence of particles which decay to gluon-gluon final states. Many of these were originally motivated by an attempt to explain an apparent excess in the diphoton invariant mass distribution observed around  $m_{\gamma\gamma} \sim 750$  GeV [11]. Some of the models predicting  $\gamma\gamma$  final states also predict a strong preference for  $gg$  final states. Whilst the resonance was later found to be the result of statistical fluctuations, such models are still of interest in exploring possible BSM resonances.

One such model, a pseudo-Nambu-Goldstone (pNG) boson of a new QCD-like theory is produced by gluon fusion and decays into a pair of the Standard Model gauge bosons [12]. The

scalar boson,  $\phi$ , produced by gluon-gluon fusion, has relevant interaction terms parametrised as

$$\mathcal{L}_{eff} = \frac{\alpha}{4\pi} \frac{k_\gamma}{\Lambda_\gamma} \phi F_{\mu\nu} \tilde{F}^{\mu\nu} + \frac{\alpha_s}{4\pi} \frac{k_g}{\Lambda_g} \phi G_{\mu\nu}^a \tilde{G}^{a\mu\nu} \quad (2.11)$$

where  $F$  is the field strength of the photon,  $\tilde{F}^{\mu\nu} \equiv \frac{1}{2}\epsilon^{\mu\nu\rho\sigma} F_{\rho\sigma}$ ,  $G$  is the gluon field strength,  $k_\gamma$  and  $k_g$  are dimensionless constants and  $\Lambda_\gamma$  and  $\Lambda_g$  are mass parameters.

Widths of decays  $\phi \rightarrow gg$  and  $\phi \rightarrow \gamma\gamma$  following the effective interactions of equation 2.11 are calculated as in [13],

$$\Gamma(\phi \rightarrow gg) = \frac{\alpha_s^2}{8\pi^3} \frac{k_g^2 m_\phi^3}{\Lambda_g^2} \quad (2.12)$$

$$\Gamma(\phi \rightarrow \gamma\gamma) = \frac{\alpha^2}{64\pi^3} \frac{k_\gamma^2 m_\phi^3}{\Lambda_\gamma^2} \quad (2.13)$$

where  $m_\phi$  is the scalar boson mass. With the assumption  $k_\gamma/\Lambda_\gamma \sim k_g/\Lambda_g$ , the dominant decay is into two gluons. No decays to  $qg$  or  $qq$  would be expected.

## 2.3 Jet Phenomenology

The Large Hadron Collider is now able to reach a centre-of-mass energy of 13 TeV, producing copious hard-scatter events - defined as processes in which the momentum transfer is large compared to the proton mass. A measure of ‘‘hardness’’ is provided by the component of momentum transverse to the beam,  $p_T$ .

### Hadronisation and Jets

Isolated quarks and gluons are not observed in isolation in ATLAS, due to colour confinement. The strength of the gluon field between particles possessing colour charge does not decrease rapidly unlike the electric field between electrically charged particles. Instead, the gluon field forms a QCD flux tube, and the strong force is constant between the two particles. As the two particles increase their separation, it becomes energetically favourable for a new quark-antiquark pair to form, Figure 2.6. In high energy collisions, this process continues many times, resulting in a collimated spray of colour-neutral particles (mesons and baryons) called jets. Gluon bremsstrahlung can contribute to this process.

The underlying event includes many low- $p_T$  interactions between the two hadronic remnants of a p-p collision. These semi- or non-perturbative interactions cannot be unambiguously separated from the process of hadronisation.

In the SM, jet pairs produced from hadronic collisions primarily result from  $2 \rightarrow 2$  parton scattering by strong interactions. QCD predicts the invariant mass spectrum of such jets is smooth and monotonically decreasing [14].

Simulations of jet formation typically rely on two different models of hadronisation (Figure 2.7), the Cluster Model and the String Model:

- Cluster Model - The model splits gluons non-perturbatively into  $q\bar{q}$  pairs after the initial “preconfinement” stage of the parton shower [16]. These colour-singlet combinations are assumed to form clusters decaying isotropically into hadron pairs [17]. The Cluster Model is used in the Herwig event generator, see for instance [18].
- String Model - The quarks are treated as being connected by a relativistic gluonic “string” representing the colour flux stretched between the  $q\bar{q}$  pair. It has a linearly increasing potential as the partons become separated, with an area law for matrix elements:

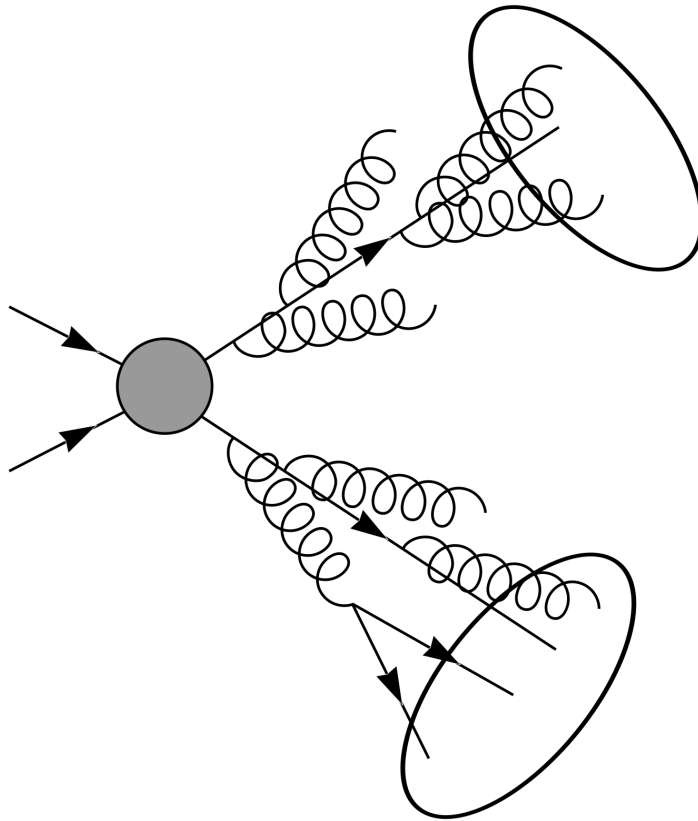


Figure 2.6: The formation of two jets from a parton collision. The jets are formed by the grouping together of collinear radiation. From [15].

$$|M(q\bar{q} \rightarrow h_1 \dots h_n)|^2 \propto e^{-bA} \quad (2.14)$$

where  $h_1 \dots h_n$  are the resultant hadrons, and  $A$  is the area of space-time swept out by the string. The hadrons are formed when the string breaks up via  $q\bar{q}$  production [19]. The model has extra parameters for the transverse momentum distribution and heavy particle suppression, but fewer problems describing baryon production than the cluster model [17].

The PYTHIA event generator [20] used in this analysis uses a specific implementation of the string model called the Lund String Model [21, 22]. This implements the Lund Symmetric

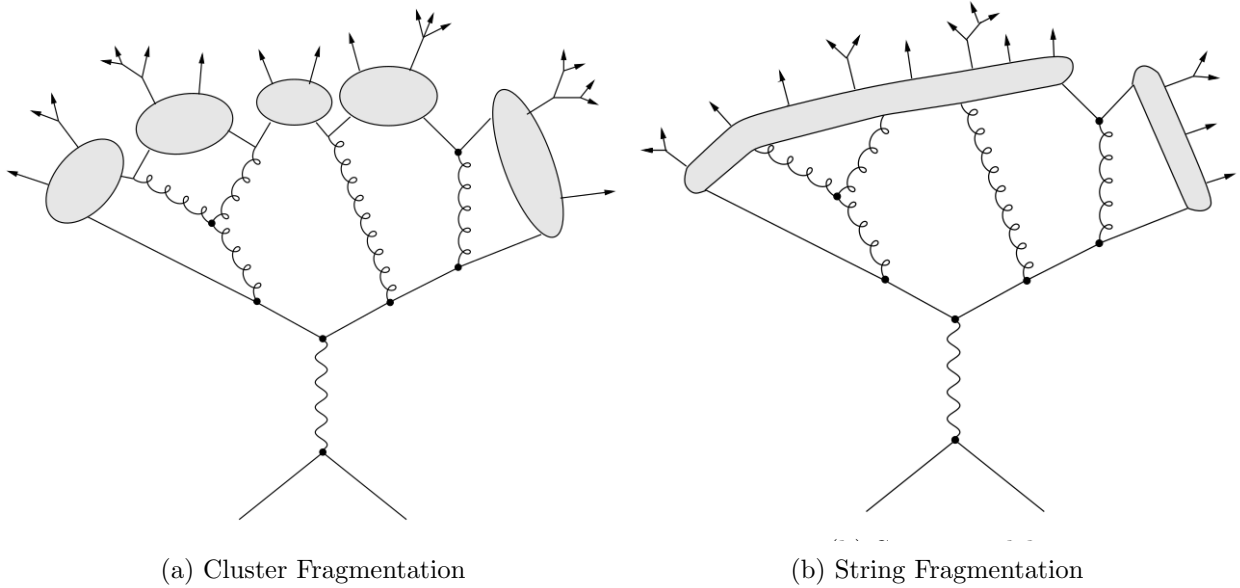


Figure 2.7: Hadronisation Models. Figures from [17].

Fragmentation Function,

$$f(z) = \frac{(1-z)^a}{z} e^{-\left(\frac{bm_\perp^2}{z}\right)} \quad (2.15)$$

where  $z$  is the particle momentum fraction, and  $m_\perp$  is the hadron transverse mass.

### Jet Reconstruction Algorithms

Whilst jets can often be observed in an ATLAS event display, precise definitions are required for any quantitative analysis [23, 24]. Characterisation of jets in ATLAS is done using sequential clustering algorithms. The purpose of these algorithms is to reduce the final state to just a few jets from the more complex input of a large number of particle tracks. A number of properties are desired of these algorithms [25], which were set out in the “Snowmass accord” in 1990 [26]:

1. Simple to implement in an experimental analysis

2. Simple to implement in the theoretical calculation
3. Defined at any order of perturbation theory
4. Yields finite cross section at any order of perturbation theory
5. Yields a cross section that is relatively insensitive to hadronisation

To satisfy the final two points, algorithms are preferred which are infrared and collinear (IRC) safe [23]. This means that the value of the final observable cannot change in the event of a collinear splitting, or the emission of a soft particle. IRC safety is important for a variety of reasons [24]:

- Accurate SM predictions at ATLAS rely on fixed-order perturbative QCD calculations in which collinear splitting and soft emissions are associated with divergent tree-level matrix elements. These should cancel with opposite sign divergent loop matrix elements. In the case of IRC unsafe jets, these tree-level splittings and loop diagrams can lead to different sets of jets, breaking cancellation and leading to infinite cross sections (this is point 4 of the Snowmass conditions).
- The motivation for constructing jets is that we want to avoid using observables which are sensitive to the effectively random and unpredictable dynamics within jet formation. This includes the collinear splittings from fragmentation and non-perturbative dynamics, as well as emission of soft particles in QCD events. Even the average properties are hard to predict due to the involvement of non-perturbative phenomena. This is linked to point 5 of the Snowmass conditions.
- Each experimental detector has a particular combination of tracking and calorimetry equipment which provide a different set of resolutions and thresholds. Comparing experimental results from, for example ATLAS and CMS, can be difficult if IRC unsafe algorithms are used.

Two main families of jet algorithm exist. The first is based on a “top-down” approach, relying on the idea that QCD branching and hadronisation do not change the bulk features of an event’s energy flow into a cone. These “cone” algorithms are the oldest type, having first been developed in the 1970s by Sterman and Weinberg [27].

### Cone Algorithms

Cone algorithms have historically been plagued by issues of IRC safety [24]. These originate from an inability to adequately deal with instances in which the cones obtained from two distinct seeds share particles, i.e. overlap. Two broadly defined solutions to this problem exist, progressive removal and split-merge.

In the progressive removal (IC-PR) approach, once a stable cone has been found, having been seeded from the particle with the largest transverse momentum, it is called a jet, and all particles it contains are removed from the event. The next seed is taken as the highest  $p_T$  particle left and the process is repeated. The use of the hardest particle for each seed leads to collinear unsafety, since the splitting of the highest  $p_T$  particle into a collinear pair can lead to another lower  $p_T$  particle pointing in a different direction becoming the seed particle. This leads to a different set of final jets, Fig. 2.8. Here, all diagrams represent the same initial state, however (b) and (d) include an additional splitting of the highest  $p_T$  particle. The collinear unsafe IC-PR algorithm on the right therefore assigns the leftmost particle in (d) as the seed, and produces a second jet from the rightmost particle. This has additional consequences in perturbative QCD: after integration over loop variables in (a) and the splitting angle in (b), whilst both diagrams have infinite weights, the signs are opposite, and the infinities cancel. This is not the case in (c) and (d), where the infinities contribute separately to the 1-jet and 2-jet cross sections, making them divergent.

An alternative approach to the IC-PR algorithms is the split-merge procedure, IC-SM. Here, one finds all the stable cones obtained by iterating over all of the particles. One merges two cones if the softer cone has more than a fraction,  $f$  (generally 0.5-0.75 [28]), of its transverse

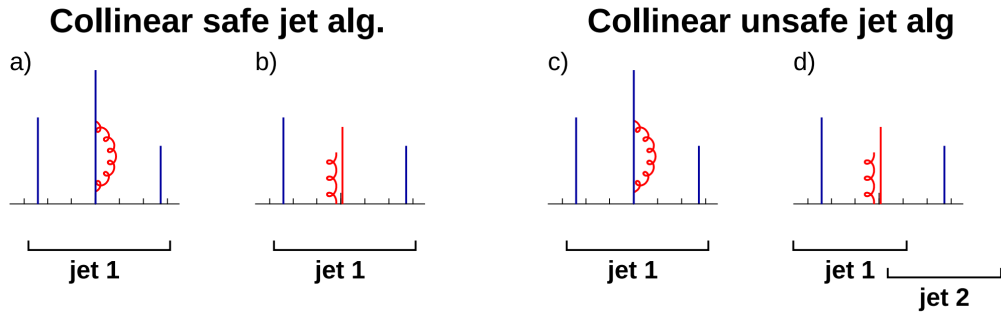


Figure 2.8: Illustration of collinear safety (left) and collinear unsafety in an IC-PR type algorithm (right). Partons are vertical lines, their height is proportional to their transverse momentum, and the horizontal axis indicates rapidity. From [24].

momentum shared with the harder cone (otherwise particles are assigned to the cone to which they are closer). This has the drawback that a new soft seed particle can cause the algorithm to find new stable cones, altering the final set of jets (infrared unsafety). For illustration, consider Fig. 2.9. In (a), two hard partons both act as seeds, and two stable jets are found. This is true also in (b), where there is an additional loop present. In (c) however, the extra soft gluon provides a new seed, and so a new stable cone is found containing both original hard partons. Since this stable cone overlaps with the two original ones, only one jet is found.

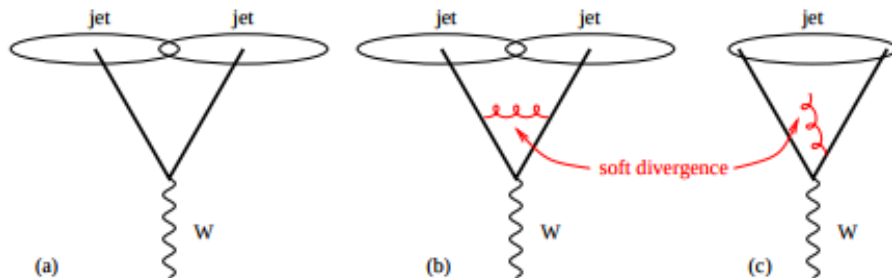


Figure 2.9: Configurations illustrating IR unsafety of IC-SM algorithms in events with a  $W$  and two hard partons. The addition of a soft gluon converts the event from having two jets to just one jet. In contrast to fig. 2.8, here the explicit angular structure is shown (rather than  $p_T$  as a function of rapidity). From [24].

### Sequential Clustering Algorithms

A second family, the sequential clustering algorithms are now generally favoured at ATLAS. These have the advantage of being IRC safe [29, 30] and modern computer techniques have led to much improved performance [31]. The only IRC safe cone algorithm is SIScone, however this has proven poor at resolving multijets [29].

All sequential clustering algorithms use a similar method, requiring two distance variables,  $d_{ij}$ ,  $d_{iB}$ .

$$d_{ij} = \min(p_{ti}^a, p_{tj}^a) \times \frac{R_{ij}^2}{R}, \quad (2.16)$$

$$d_{iB} = p_{ti}^a, \quad (2.17)$$

where  $a$  is an exponent corresponding to the particular algorithm used, and  $R_{ij}^2 = (\eta_i - \eta_j)^2 + (\phi_i - \phi_j)^2$  is the  $(\eta - \phi)$  space distance between the particles: The ATLAS detector (described in detail in chapter 3) uses a cylindrical coordinate system.  $\phi$  is the azimuthal angle around the beampipe, and  $\eta$  is a convenient observable called the pseudorapidity, defined in terms of the polar angle  $\theta$ :

$$\eta = -\ln \left( \tan \left( \frac{\theta}{2} \right) \right). \quad (2.18)$$

$R$  is the radius parameter determining the final size of the jets, usually  $\sim 0.4 - 0.7$  (0.4 in this analysis [9]).  $d_{iB}$  is the momentum space distance between beam axis and detected particle.

First, the minimum of the entire set  $\{d_{ij}, d_{iB}\}$  is found. If  $d_{ij}$  is the minimum, then particles  $i$  and  $j$  are combined into one particle using the summation of four-vectors, after which  $i$  and  $j$  are removed from the list of particles. If  $d_{iB}$  is the minimum,  $i$  is labelled a final jet and removed from the list of particles. This process is then repeated, and continues until

either of two conditions are met. In inclusive clustering, all particles must be a part of a jet with distance between the jet axes  $R_{ij} > R$ . In Exclusive clustering, the process ends when the desired number of jets have been found.

The most common algorithm used at ATLAS, and that used in this analysis, is the anti- $k_t$  algorithm, which uses an exponent  $a = -2$ , resulting in the following equations:

$$d_{ij} = \min \left( \frac{1}{p_{ti}^2}, \frac{1}{p_{tj}^2} \right) \times \frac{R_{ij}^2}{R}, \quad (2.19)$$

$$d_{iB} = p_{ti}^{-2}. \quad (2.20)$$

Equation 2.19 leads to an algorithm dominated by high- $p_T$ , preferring to cluster hard particles first. This means that the algorithm is poor for studying jet substructure, but is only weakly affected by pileup and the underlying event, and so very good at resolving jets.

Alternatives to anti- $k_t$  are the  $k_t$  ( $a = 2$ ) and Cambridge/Aachen ( $a = 0$ ) algorithms. Examples of these alternative jet reconstruction algorithms are shown in Figure 2.10 using the same input data.

## Jet Tagging

Several theorised extensions of the Standard Model include new particles decaying preferentially to either quarks or gluons. Techniques which help discriminate between quark-initiated and gluon-initiated jets can therefore be used to increase the sensitivity of searches for these new states. Gluons are in the adjoint representation of SU(3) whilst quarks are in the fundamental representation. This means that gluons carry both a colour and anti-colour charge, while quarks carry only a single colour charge [4]. The Altarelli-Parisi splitting functions [33] contain different factors for gluon radiation from a gluon ( $C_A$ ) and from a quark ( $C_F$ ), coming from the two colour charges of gluons compared to the one of quarks. The Casimir Ratio drives the difference between patterns of radiation between quarks and gluons [34],

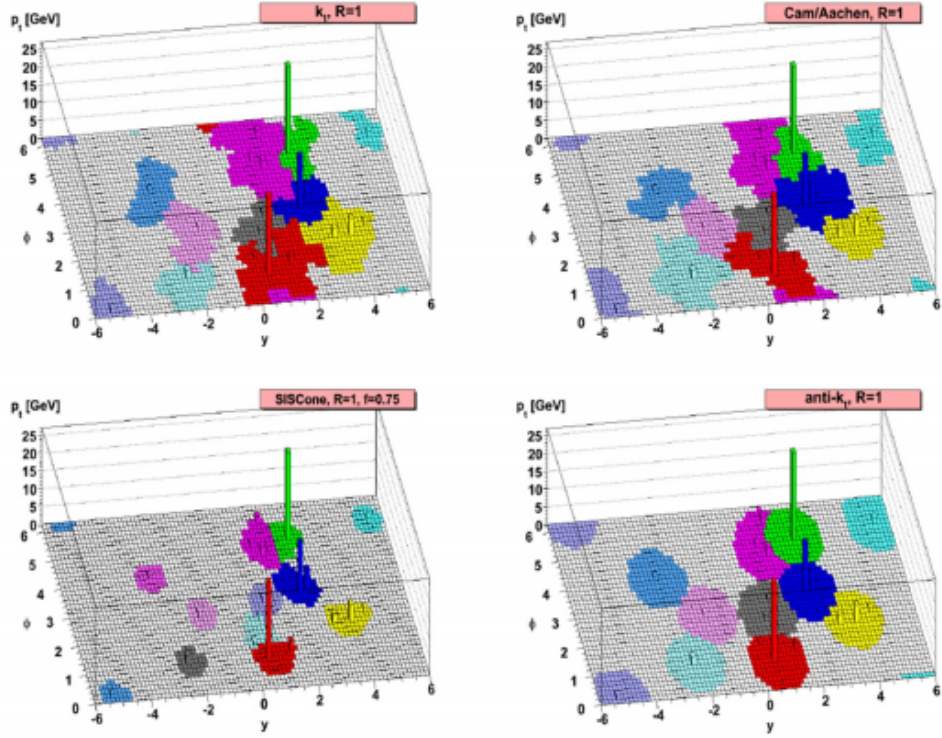


Figure 2.10: An example parton-level event (generated with HERWIG++ [32]), together with many random soft “ghosts”, clustered with four different jet algorithms. Note the conical shape of the anti- $k_t$ ’s jets illustrating the algorithm’s preference for hard radiation. From Ref. [30].

$$\frac{C_A}{C_F} = \frac{9}{4} \sim 2. \quad (2.21)$$

The result is that gluon jets have on average more constituents than quark jets, and a broader radiation pattern. The number of particles in quark and gluon jets was measured at LEP [35, 15]. It was found that the average multiplicity of any type of particle (and its variance) can be approximated by

$$\frac{\langle N_g \rangle}{\langle N_q \rangle} = \frac{C_A}{C_F}, \quad (2.22)$$

$$\frac{\sigma_g^2}{\sigma_q^2} = \frac{C_A}{C_F}. \quad (2.23)$$

To leading order, the angular width of the gluon-jet,  $\delta_g$ , and quark-jet,  $\delta_q$ , using the Sterman-Weinberg definition [27] is

$$\delta_g = \delta_q^{C_F/C_A}. \quad (2.24)$$

Intuitively, one can consider a quark jet as being dominated by the first gluon emission, after which the jet continues to shower like a gluon jet. At a given energy, the gluon jets contain more particles, and so fewer corresponding hard particles.

At LEP, it was found that B-jets behave more similarly to gluon jets than to light quark jets [36]. The number of particles and angular spread was larger than in the light quark jets due to the longer decay chain of B-hadrons overwhelming the effect of the perturbative parton shower. This effect is less in the higher energy of the LHC, due to the higher  $p_T$  of the jets, and more boosted B-hadrons. At higher  $p_T$ , the QCD shower produces more particles, whereas the particle multiplicity from the B-hadron decay is relatively fixed [15].

Jet flavour is not necessarily well defined: in the parton-shower picture, the shower products from two hard partons could significantly overlap. Depending on the jet reconstruction used, the resulting jets may merge or have strange shapes, and the jet properties may not be distributed such that they correspond to isolated quark or gluon jets.

The semi-classical parton-shower picture differs from the quantum level when one considers NLO quantum effects. Here, there is interference between diagrams with the same final particle flavour and momentum. Figure 2.11 illustrates the case where collinear gluon emission from unambiguous quark-initiated jets is combined with the quantum mechanically

indistinguishable correction where the gluons originate from an unrelated hard parton splitting. Fortunately, the parton-shower-like diagram has a much larger amplitude than the hard-gluon-splitting diagram, and so dominates the matrix element calculation, thus the uncertainty on labelling the configuration is small.

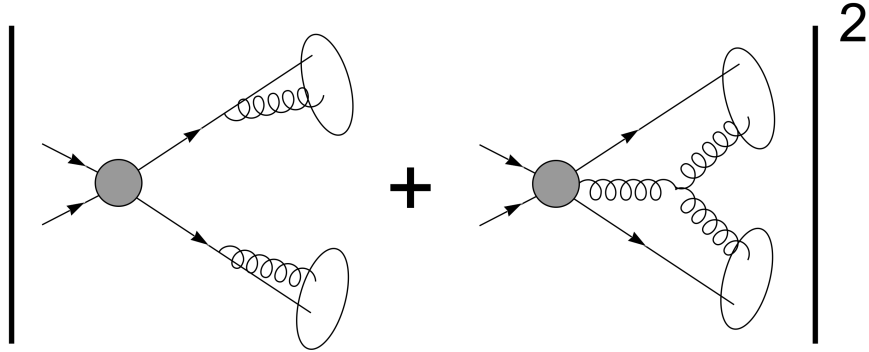


Figure 2.11: In the left diagram, the quark jets have properties largely determined by the emitted gluons. The same configuration can be produced from the right diagram, in which a third hard parton, a gluon, splits into two gluons with momenta comparable to the showered gluons. These two amplitudes interfere, and so it may not make sense to describe the final state configuration as having two quark jets. In this case, the amplitude for the shower diagram on the left is much larger than the hard-gluon-splitting event for the same final state kinematics. As the gluons become more collinear with the quarks, the first amplitude is divergent. From [15].

Up to some overall normalisation, the NLO effects are reproduced by merging the parton shower with matrix element corrections. In fully matched samples, each jet is associated unambiguously with exactly one hard parton of known flavour. The final distributions depend only weakly on the merging scale, thus the conclusions one can draw regarding quark and gluon discrimination are the same as for many other applications, such as kinematic reconstruction - the answers are unambiguous when the final state jets are clearly separated [15]. Ambiguous final states are avoided through the topological selection criteria.

## Chapter 3

# The ATLAS Detector

### 3.1 CERN and the Large Hadron Collider

The Large Hadron Collider (LHC) is a 27 km superconducting particle accelerator designed to collide bunches of protons. The proton bunches are accelerated to an energy of 450 GeV before being injected into the LHC. There are two beam pipes each containing proton bunches travelling in opposite directions. At the four crossing points of the proton beam reside the largest detectors at CERN. ATLAS is situated at Point 1, close to the main CERN site at Meyrin, Switzerland.

#### Running conditions 2015 - 2018

Two key figures define the LHC's ability to deliver pp collisions for analysis with ATLAS, the centre-of-mass energy and luminosity [37]. Any new particles created in a collision are limited in their mass by the centre-of-mass energy, and interaction cross sections will be determined by this energy. The instantaneous luminosity defines the interaction rate, and hence the statistics available for analysis:  $N_{events} = \mathcal{L}\sigma_{events}$  where  $N_{events}$  is the number of events collected per second for a process with corresponding cross section  $\sigma_{events}$ . The luminosity of a beam with a Gaussian profile is given by

$$\mathcal{L} = f_r N_b^2 n_b \frac{\gamma_r}{4\pi\epsilon_n\beta^*} F \quad (3.1)$$

where  $f_r$  is the revolution frequency of  $n_b$  bunches of  $N_b$  protons each.  $\gamma_r = E/m$  is the relativistic factor for the protons.  $\beta^*$  characterises the spread of the beam, and  $\epsilon_n$  is the normalised transverse beam emittance - a measure of the distance between protons and the spread of their momenta. Both  $\beta^*$  and  $\epsilon_n$  have units of length.  $F$  is a factor defining the loss in luminosity due to the crossing angle of the beams.

The data-taking conditions during Run 2 evolved significantly. The LHC peak instantaneous luminosity at the start of fills increased from  $5 \times 10^{33} \text{cm}^{-2} \text{s}^{-1}$  to  $19 \times 10^{33} \text{cm}^{-2} \text{s}^{-1}$ . This was the result of increasing the number of colliding bunch pairs ( $n_b$ ) and the average bunch current ( $N_b$ ), as well as progressively stronger focusing in ATLAS (characterised by  $\beta^*$ ) - see table 3.1 [38] and Figure 3.1.

Measurement of luminosity is based on an absolute calibration of the primary luminosity-sensitive detectors in low-luminosity runs with conditions specially tailored for the LHC using the van der Meer (vdM) method [39, 40].

This vdM calibration was performed once per year during Run 2 data-taking. Relative comparisons of the luminosities measured by different detectors were used to set limits on any possible change of the calibration through the year. During Run 2, the primary measurements of the bunch-by-bunch luminosity was provided by LUCID2 [41], consisting of 16 photomultiplier tubes (PMTs) in each forward arm of ATLAS (A and C sides). These are placed approximately  $z = \pm 17$  m from the interaction point.

Data is recorded in *runs* - events generated within the same proton fill of the LHC, typically over about 12 hours. These runs are then subdivided into *luminosity blocks*, the smallest period of data taking for which the integrated luminosity can be determined reliably [42].

Parameter	2015	2016	2017	2018
Maximum number of colliding bunch pairs ( $n_b$ )	2232	2208	2544/1909	2544
Bunch Spacing (ns)	25	25	25/8b4e	25
Typical bunch population ( $10^{11}$ protons)	1.1	1.1	1.1/1.2	1.1
$\beta^*(m)$	0.8	0.4	0.3	0.3 - 0.25
Peak Luminosity $\mathcal{L}_{peak}$ ( $10^{33} cm^{-2} s^{-1}$ )	5	13	16	19
Peak number of inelastic interactions/crossing ( $\langle \mu \rangle$ )	$\sim 16$	$\sim 41$	$\sim 45/60$	$\sim 55$
Luminosity-weighted mean inelastic interactions/crossing	13	25	38	36
Total delivered integrated luminosity ( $fb^{-1}$ )	4.0	38.5	50.2	63.4

Table 3.1: Selected LHC parameters for pp collisions at  $\sqrt{s} = 13$  TeV in 2015 - 2018. The values shown are representative of the best accelerator performance during normal physics operation. In 2017, the LHC was run in two modes: standard 25 ns bunch train operation with long trains, and ‘8b4e’, denoting a pattern of eight bunches separated by 25 ns followed by a four bunch-slot gap. Values are given for both configurations. The instantaneous luminosity was levelled by beam separation to about  $\mathcal{L}_{peak} = 16 \times 10^{33} cm^{-2} s^{-1}$  for part of the 8b4e period (using a beam injection scheme with 8 bunches filled and 4 empty). 0.1  $fb^{-1}$  of physics data delivered during 2015 with 50 ns bunch spacing is not included [38].

## Pileup

The high luminosity available at the LHC results in several proton-proton collisions being recorded in a single event. This is referred to as pileup, divided into two different types depending on its origin:

- In-time pileup: Multiple particle collisions occur in each bunch crossing, each producing their own primary vertices and corresponding tracks.
- Out-of-time pileup: With only 25 ns between bunch crossings, the products of a previous bunch crossing can still be detected during the present bunch crossing, and contribute to the same recorded event.

Pileup,  $\mu$ , defined as the number of collisions per bunch crossing, is predicted from the present run conditions using the following equation,

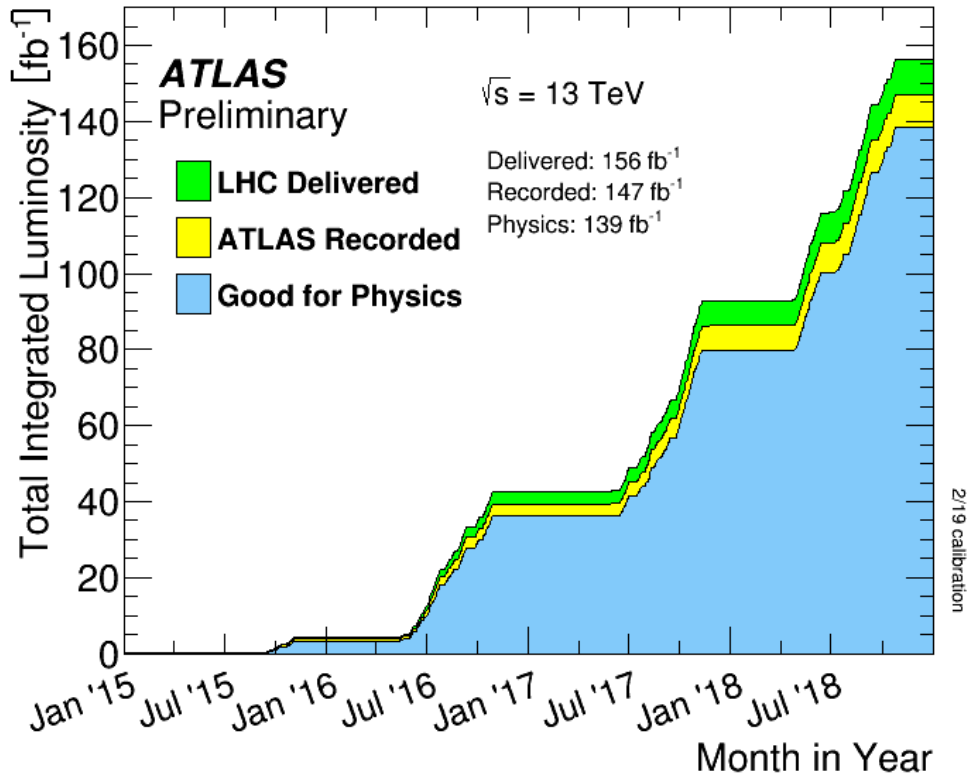


Figure 3.1: Cumulative luminosity versus time delivered to ATLAS (green), recorded by ATLAS (yellow), and certified to be good quality data (blue) during stable beams for pp collisions at 13 TeV centre-of-mass energy in 2015-2018[43].

$$\mu = \frac{\mathcal{L}_0 \sigma_{inelastic}}{n_b f_r} \quad (3.2)$$

with  $\mathcal{L}_0$  the instantaneous luminosity and  $\sigma_{inelastic}$  the pp inelastic cross-section. A more useful measure is often the average of  $\mu$  over a luminosity block,  $\langle \mu \rangle$ .

### 3.2 The ATLAS Detector

The ATLAS detector (A Toroidal LHC ApparatuS) is a general purpose particle detector located at one of the four beam crossing points of the LHC ring. Proton bunches collide in the centre of the detector, and collision products radiate from the interaction point (IP)

through the bulk of the detector. Various subsystems measure the energy and momenta of these products [44, 42]. A cutaway view of ATLAS is shown in figure 3.2.

### **Design Philosophy**

ATLAS is designed to be a general-purpose particle detector, and so must be able to detect, or at least infer, the presence of all known particles. To be sensitive to signatures of new physics, ATLAS must be able to measure the properties of as many collision products as possible, ideally letting none escape without detection. Neutrinos, despite being able to travel through kilometres of solid matter with only a small chance of interacting, can be detected indirectly as missing energy. ATLAS is thus designed to have as much detector mass close to the beam crossing point as possible, with the various detector subsystems arranged in concentric layers radiating outwards.

The different types of particle moving through the detector will interact differently, according to their properties. Charged particles such as electrons and protons will interact with the inner layers, depositing detectable charge in the silicon pixel and strip detectors. Photons will create showers in the electromagnetic calorimeter, whilst neutrons will only shower in the hadronic calorimeter. Muons travel most easily through the detector, and so the outer most component of ATLAS is the muon spectrometer. Conservation of momentum is an important consideration in a detector such as ATLAS, since neutrinos and signatures of new physics can be inferred as an imbalance of the total transverse energy deposited in a collision event.

### **Coordinate System**

The ATLAS detector, described in detail in Chapter 3, uses a right-handed coordinate system with the origin at the centre of the detector. The x-axis points towards the centre of the LHC ring, the y-axis points upwards. The z-axis points along the beam pipe, from point 1 to point 8 (towards Geneva).

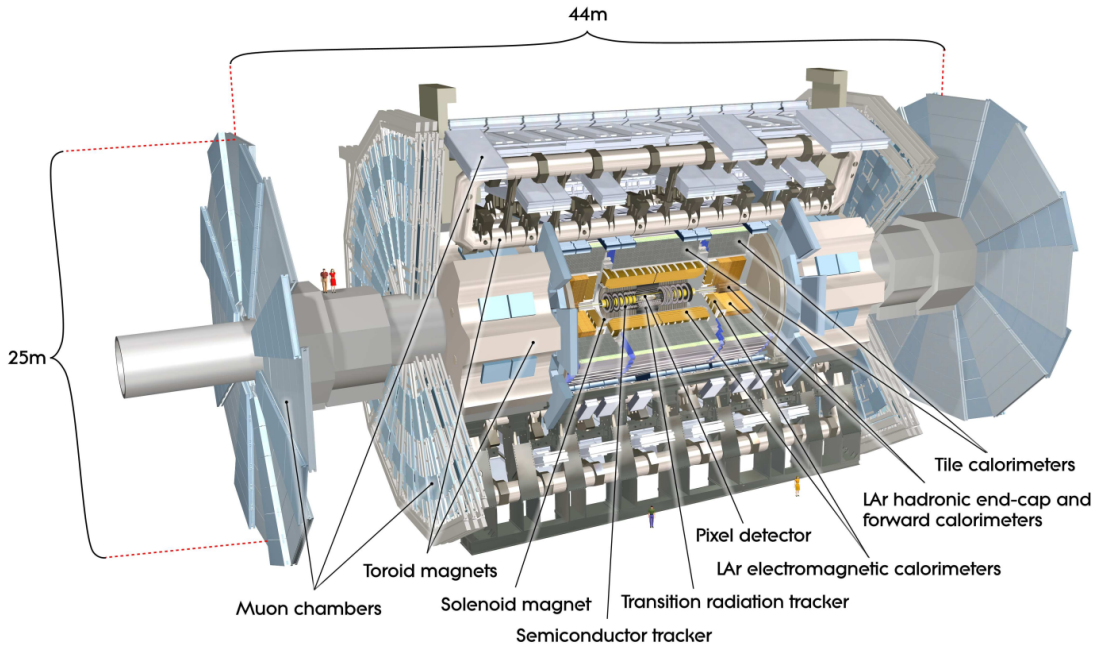


Figure 3.2: Cut-away view of the ATLAS detector, from [45]. The function and construction of each of the sub-detector systems is outlined below.

A cylindrical coordinate system is also commonly used, with  $r$ ,  $\phi$  and  $\eta$ .  $r$  is the radial axis ( $=\sqrt{x^2 + y^2}$ ) with  $\phi$  the azimuthal angle around the beampipe/ $z$ -axis.  $\eta$  is the pseudorapidity as defined in 2.18.

In jet analyses, a more commonly used variable is the rapidity,  $y$ , defined in Equation 3.3, since differences in rapidity are invariant under Lorentz boosts along the  $z$ -axis. This therefore provides a convenient way to measure how 'back-to-back' two jets are in their rest frame.

$$y = \frac{1}{2} \ln \left( \frac{E + p_z}{E - p_z} \right). \quad (3.3)$$

## Magnets

A magnetic field is necessary to measure the momenta of charged particles which have their paths diverted when moving through the field. The bending radius is inversely proportional to the particle's momentum - the greater the momentum, the less the track will curve in the detector. ATLAS is unusual amongst particle detectors for utilising two separate magnet systems, an inner 2 Tesla superconducting solenoid and three outer air-cooled toroid magnets - one barrel and two end-caps, which produce a toroidal magnetic field of approximately 0.5 T and 1 T respectively. CMS by comparison uses a single 4 Tesla superconducting solenoid. The benefit to ATLAS' hybrid magnet system comes mostly at high- $\eta$ . Since the solenoid magnetic field is aligned with the beam axis, only a small fraction of a high- $\eta$  particle's momentum is perpendicular to the field, limiting the resolution with which the momentum can be resolved. The toroidal magnets produce a magnetic field perpendicular to the beam-axis (and therefore perpendicular to high- $\eta$  particle tracks). The two magnet systems therefore complement each other and provide good momentum resolution throughout the detector.

## Inner Detector

### Inner Tracker

The central region of the detector, closest to the interaction point experiences the highest flux of particles. Accurate identification of particle momenta is important, to resolve individual particle tracks and vertices. Silicon semiconductor tracking detectors were chosen to provide highly accurate energy and spatial resolution. These come in the form of pixel detectors closest to the interaction point and micro-strip detectors further out. These silicon layers are arranged in a concentric cylindrical geometry in the barrel region, and as perpendicular disks in the end-cap, providing good  $\eta$  coverage up to  $|\eta| = 2.5$ . The insertable b-layer (IBL) was added closer to a new thinner beryllium beam pipe during the first long shutdown of atlas, in May 2014, providing an extra layer of silicon pixel detectors just 33 mm from the

beam pipe. All of these detectors are designed to cope with the most radiation intensive environment in ATLAS. The inner tracker provides an intrinsic accuracy in  $R - \phi$  of  $1 - \mu m$  in the pixels, and  $17 \mu m$  in the strips.

### Transition Radiation Tracker

The transition radiation tracker (TRT) is composed of “straw” drift chambers containing xenon, with carbon-dioxide added for avalanche quenching. The TRT is located around the inner tracker, with an inner radius of 560 mm and an outer radius of 1080 mm. Approximately 50,000 straws are aligned parallel to  $z$  in the 1140 mm long barrel region, and 122,000 are aligned perpendicular to  $z$  in the end-caps. The TRT provides continuous tracking, averaging 36 hits per track, improving pattern recognition and momentum resolution over  $\eta < 2.0$ .

Transition radiation comprises photons produced as relativistic particles move through a boundary between two materials of different permittivity. Each straw is a 4 mm diameter aluminium tube forming a cathode, with a central gold-plated tungsten wire forming the anode. The aluminium cathode is kept at 1520 V while the anode is grounded. A polypropylene film separates the straws, providing the permittivity difference necessary to produce transition radiation. Less massive particles produce transition energies at lower energies, allowing for instance electrons to be distinguished from pions.

### Calorimetry in ATLAS

The ATLAS calorimeters cover a range of  $\eta < 4.9$ , using different techniques suited to different requirements and radiation regimes. The EM calorimeter provides a fine granularity over an  $\eta$  range matched to the inner detector. The rest of the calorimeter system provides a coarser granularity sufficient for jet reconstruction and  $E_T^{miss}$  measurements.

For reliable measurement, the calorimeters are designed to provide good containment of electromagnetic and hadronic showers, and minimise punch-through to the muon detectors.

There are 9.7 interaction lengths in the barrel and 10 in the end-caps which ensures good resolution of high energy jets and  $E_T^{miss}$ .

The calorimeter systems closest to the beam-line are contained within three cryostats, one barrel, containing the electromagnetic barrel calorimeter, and two end-caps. These end-cap cryostats contain an electromagnetic end-cap calorimeter (EMEC), a hadronic end-cap calorimeter (HEC), and a forward calorimeter (FCal), see Figure 3.4. The cryostats are required since all of these calorimeters use liquid-argon (LAr), which has been chosen for its intrinsic linear behaviour, stability of response over time, and its intrinsic radiation-hardness.

### Electromagnetic Calorimeter

The electromagnetic calorimeter is constructed from lead absorbing plates alternating with liquid argon between electrodes at a high voltage difference. The lead absorber causes charged particles to shower as they pass through, the charged particles in these showers ionise the liquid argon and free electrons in proportion to their energy. The electrodes accelerate and collect the electrons, and transmit the resulting pulse to the readout electronics.

The electromagnetic calorimeter, in common with the inner detector, is divided into a barrel part ( $\eta < 1.475$ ) and two end-caps ( $1.375 < \eta < 3.2$ ). The central region is located just behind the central solenoid, and housed in the same vacuum vessel to eliminate two vacuum walls. The electromagnetic calorimeter is a lead-LAr construction, with kapton electrodes and lead absorber plates arranged in an accordion geometry, providing complete  $\phi$  symmetry without azimuthal cracks.

The barrel electromagnetic calorimeter 3.2 m long, with an inner and outer diameter of 2.8 m and 4 m respectively. This is complemented with a liquid-argon presampler detector in front of its inner surface over the full  $\eta$ -range, providing shower sampling inside the barrel cryostat and in front of the active electromagnetic calorimeter [46]. The barrel is constructed from 2048 absorbers interleaved with readout electrodes. These electrodes are placed in the middle of the gap by honeycomb spacers. On each side of the electrode, the drift gap is

2.1 mm wide, corresponding to a drift time of  $\sim 450$  ns at an operating voltage of 2000 V. The barrel electromagnetic calorimeter is constructed from 32 modules constructed as in Figure 3.3. Each module has three layers, and a total depth of at least 22 radiation lengths ( $X_0$ ), increasing to 33  $X_0$  at high  $|\eta|$ . There are 3424 readout cells per module, including those in the presampler.

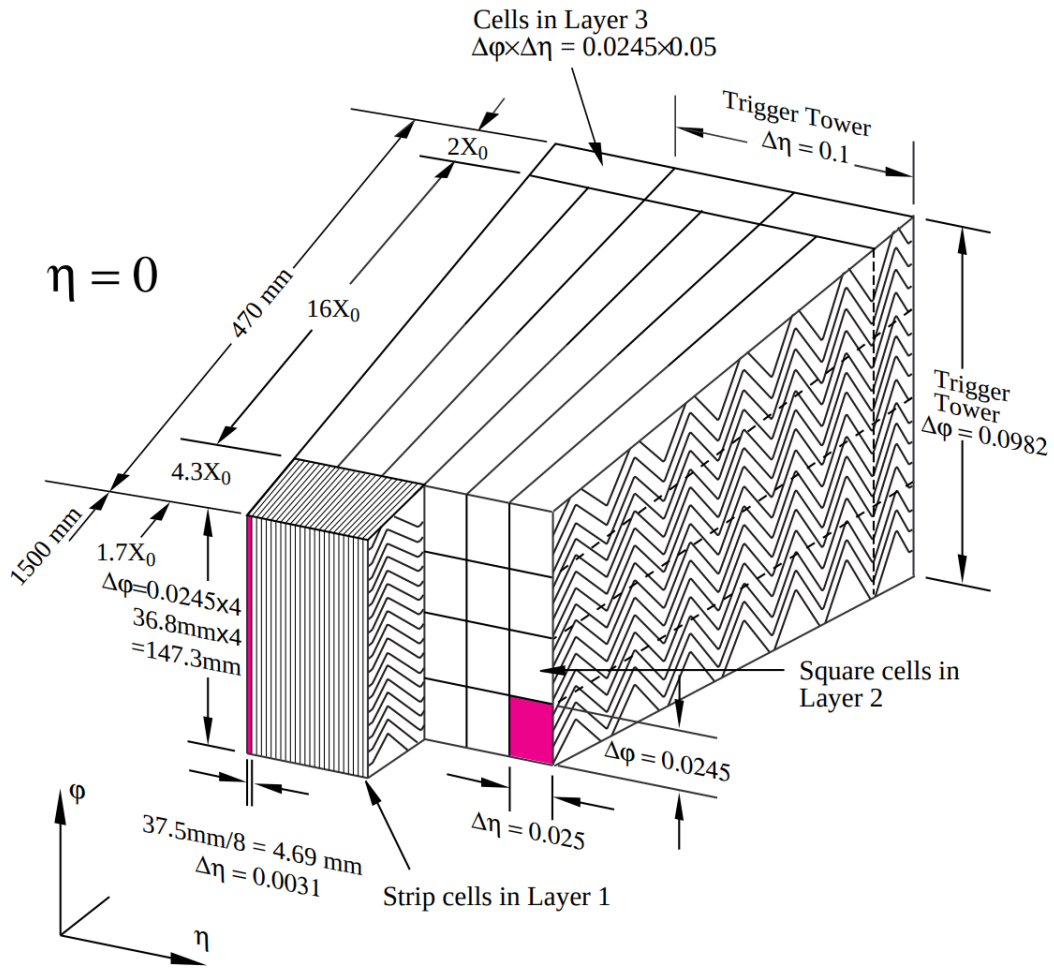


Figure 3.3: Electromagnetic Calorimeter barrel module showing the different layers and the granularity of the detector in  $\eta$  and  $\phi$ . 32 such modules make up the barrel EM calorimeter. From [42]

The EMEC calorimeters [47] consist of two wheels on either side of the barrel electromagnetic calorimeter, Figure 3.4. These each cover the region  $1.375 < |\eta| < 3.2$ . As with the barrel

calorimeter, the EMEC calorimeters have a LAr presampler calorimeter in front, these cover the range  $1.5 < |\eta| < 1.8$ .

Each end-cap consists of two co-axial wheels, an outer wheel containing 768 absorbers interleaved with readout electrodes, and an inner wheel of 256 absorbers. The electrodes are positioned in the middle of the gaps by honeycomb spacers. The total active thickness of an end-cap calorimeter is greater than  $24 X_0$  for  $|\eta| < 1.475$ .

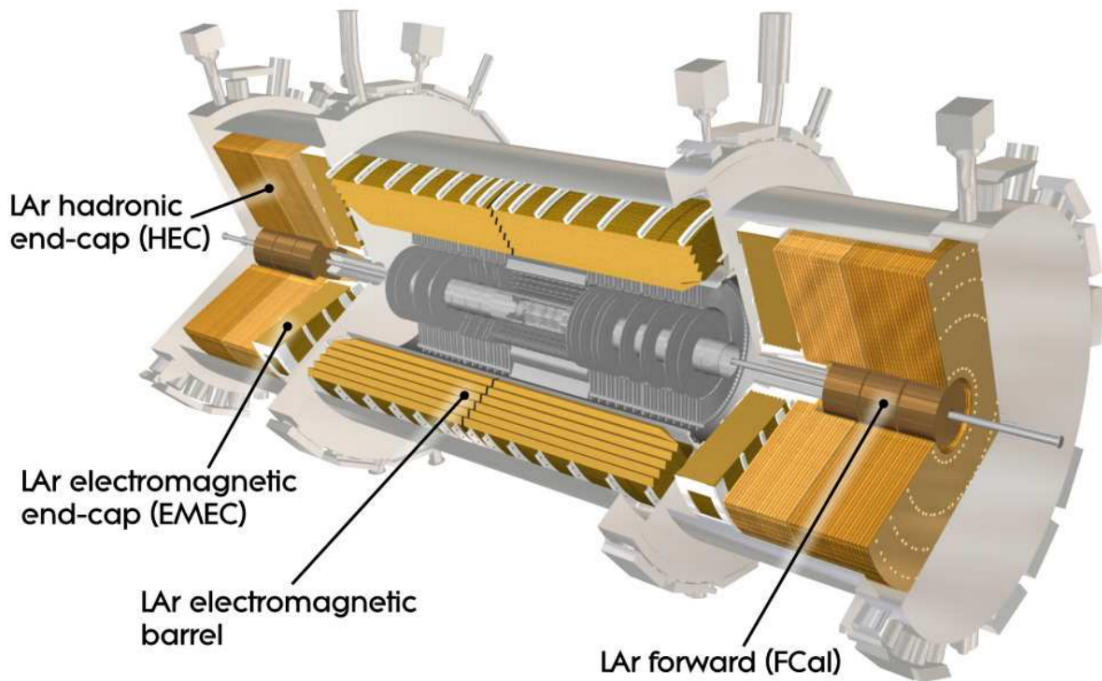


Figure 3.4: Cut-away view of the ATLAS liquid argon calorimeters [47]. The calorimeters are contained within three cryostats, one in the barrel, containing the electromagnetic barrel calorimeter, and two end-caps, each containing an electromagnetic end-cap calorimeter (EMEC), a hadronic end-cap calorimeter (HEC), and a forward calorimeter (FCal).

### Hadronic Calorimeter

Only  $\sim 2/3$  of the hadronic shower from strongly charged particles is contained within the electromagnetic calorimeter. Hadrons shower differently to electromagnetic particles due to additional strong force interactions. There is always some invisible energy which goes

towards contributing to nuclear breakup (30-45%) rather than collisions. Ionisation provides the greatest fraction of deposited energy (40-60%), while neutron generation (10-15%) and photon generation from fission ( $\sim 3\%$ ) account for the rest [48].

The design of hadronic calorimeters is slightly different to electromagnetic calorimeters, requiring significantly greater absorber thickness to fully contain a shower. This means sampling rather than homogeneous calorimeters tend to be used. In ATLAS, liquid argon and plastic scintillating tiles are used to measure the deposited energy. The liquid argon measures the electromagnetic shower and nuclear ionisation components, while invisible energy is accounted for through calibration. Plastic scintillators rely on incoming particles exciting molecules which then emit UV light on de-excitation.

The hadronic calorimeter (HCAL) is positioned outside of the electromagnetic calorimeter to contain the remaining radiation. There are three components to the hadronic calorimeter. The scintillator tile calorimeter is located in the barrel region, directly outside the EM calorimeter. In the same end-cap cryostats as the EMEC calorimeter are the LAr hadronic end-cap and LAr forward calorimeters.

The tile calorimeter (TileCal) is a sampling calorimeter using a steel absorber and scintillating tiles, Figure 3.5. There is a barrel region ( $\eta < 1.0$ ) and two extended barrels ( $0.8 < \eta < 1.7$ ), each divided azimuthally into 64 modules. The tile calorimeter extends radially between 2.28 and 4.25 m, and each section is segmented radially into three: the central region into layers 1.5, 4.1 and 1.8 interaction lengths thick; the extended barrels into layers 1.5, 2.6 and 3.3 interaction lengths thick. Two sides of the scintillating tiles are read out by wavelength shifting fibres into two separate photomultiplier tubes. The initial UV light from de-excitation must be absorbed and re-emitted in the wavelength shifting fibres so that it can propagate far enough to exit the tile.

The LAr Hadronic End-cap Calorimeter (HEC) is located directly behind the end-cap electromagnetic calorimeter extending out to  $1.5 < |\eta| < 3.2$ , overlapping with the forward and tile calorimeters. There are two independent wheels of 32 wedge shaped modules in

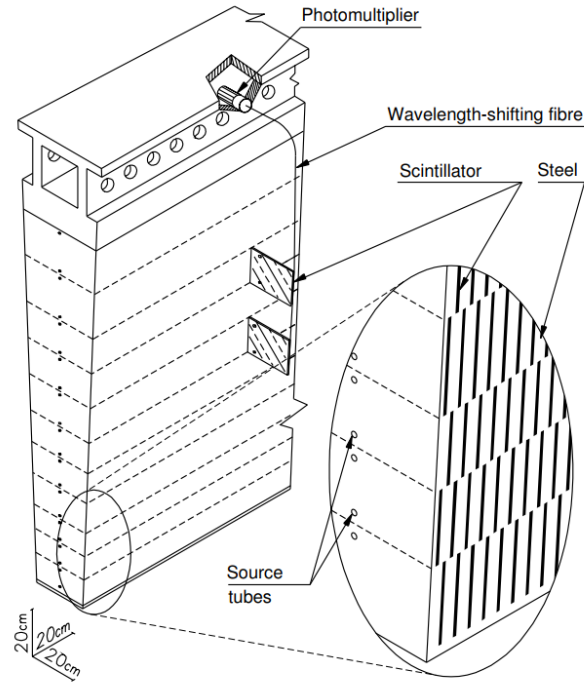


Figure 3.5: Schematic of an ATLAS tile calorimeter module. The arrangement of scintillating tiles and readout components is shown. The labelled source tubes are access channels allowing caesium calibration tests. From [42]

each end-cap. Copper plates are interleaved with 8.5 mm LAr layers, providing the active medium.

The LAr Forward Calorimeter (FCal) is integrated into the same end-cap cryostats as the HEC and EMEC. The FCal is  $\sim 10$  interaction lengths deep and consists of three modules. The first module is constructed from copper, and is optimised for electromagnetic measurements, while the second and third are made of tungsten and predominantly measure hadronic interactions. Again LAr is the active medium. The geometry of the ATLAS calorimeter systems is given in Table 3.2

	Barrel		End-cap	
<b>EM calorimeter</b>				
Number of layers and $ \eta $ coverage				
Presampler	1	$ \eta  < 1.520$	1	$1.5 <  \eta  < 1.8$
Calorimeter	3	$ \eta  < 1.350$	2	$1.375 <  \eta  < 1.5$
	2	$1.35 <  \eta  < 1.475$	3	$1.5 <  \eta  < 2.5$
			2	$2.5 <  \eta  < 3.2$
Granularity $\Delta\eta \times \Delta\phi$ versus $ \eta $				
Presampler	$0.025 \times 0.1$	$ \eta  < 1.52$	$0.025 \times 0.1$	$1.5 <  \eta  < 1.8$
Calorimeter 1st layer	$0.025/8 \times 0.1$	$ \eta  < 1.40$	$0.050 \times 0.1$	$1.375 <  \eta  < 1.425$
	$0.025 \times 0.025$	$1.40 <  \eta  < 1.475$	$0.025 \times 0.1$	$1.425 <  \eta  < 1.5$
			$0.025/8 \times 0.1$	$1.5 <  \eta  < 1.8$
			$0.025/6 \times 0.1$	$1.8 <  \eta  < 2.0$
			$0.025/4 \times 0.1$	$2.0 <  \eta  < 2.4$
			$0.025 \times 0.1$	$2.4 <  \eta  < 2.5$
		$0.1 \times 0.1$	$2.5 <  \eta  < 3.2$	
Calorimeter 2nd layer	$0.025 \times 0.025$	$ \eta  < 1.40$	$0.050 \times 0.025$	$1.375 <  \eta  < 1.425$
	$0.075 \times 0.025$	$1.40 <  \eta  < 1.475$	$0.025 \times 0.025$	$1.425 <  \eta  < 2.5$
			$0.1 \times 0.1$	$2.5 <  \eta  < 3.2$
Calorimeter 3rd layer	$0.05 \times 0.025$	$ \eta  < 1.35$	$0.050 \times 0.025$	$1.5 <  \eta  < 2.5$
Number of readout channels				
Presampler	7808		1536 (both sides)	
Calorimeter	101760		62208 (both sides)	
<b>LAr hadronic end-cap</b>				
$ \eta $ coverage			$1.5 <  \eta  < 3.2$	
Number of layers			4	
Granularity $\Delta x \times \Delta y$			$0.1 \times 0.1$	$1.5 <  \eta  < 2.5$
			$0.2 \times 0.2$	$2.5 <  \eta  < 3.2$
Readout channels			5632 (both sides)	
<b>LAr forward calorimeter</b>				
$ \eta $ coverage			$1.5 <  \eta  < 3.2$	
Number of layers			3	
Granularity $\Delta x \times \Delta y$			FCal1: $3.0 \times 2.6$	$3.15 <  \eta  < 4.30$
			FCal1:~ four times finer	$3.10 <  \eta  < 3.15,$ $4.3 <  \eta  < 4.83$
			FCal2: $3.3 \times 4.2$	$3.24 <  \eta  < 4.50$
			FCal2:~ four times finer	$3.20 <  \eta  < 3.24,$ $4.50 <  \eta  < 4.81$
			FCal3: $5.4 \times 4.7$	$3.32 <  \eta  < 4.60$
			FCal3:~ four times finer	$3.29 <  \eta  < 3.32,$ $4.60 <  \eta  < 4.75$
Readout channels			3524 (both sides)	
<b>Scintillator tile calorimeter</b>				
	Barrel		Extended Barrel	
$ \eta $ coverage	$ \eta  < 1.0$		$0.8 <  \eta  < 1.7$	
Number of layers	3		3	
Granularity $\Delta x \times \Delta y$	$0.1 \times 0.1$		$0.1 \times 0.1$	
	Last layer $0.2 \times 0.1$		$0.2 \times 0.1$	
Readout channels	5760		4092 (both sides)	

Table 3.2: Geometry of the ATLAS calorimeter system.

## Tile Calorimeter Calibration

The final cell energy in the tile calorimeter is calculated from several calibration constants derived from dedicated calibration systems which monitor the behaviour of the different detector components for each TileCal channel [49].

- Charge Injection System (CIS) [50]: Used to derive ADC<sup>1</sup> to pC conversion factors for the digital readout. Pulses are generated from discharge capacitors in the readout circuit and the electronic response measured in order to simulate physics signals in the calorimeter. This provides a quantitative relationship between analogue signals from the PMTs and the response in the TileCal readout channels. The calibration runs are conducted daily to weekly, so  $C_{ADC \rightarrow pC}$  conversion factors are regularly produced and can be applied to data.
- Caesium System [51]: A movable Caesium  $\gamma$ -source is used to calibrate the optical components and PMT gains. Calibration constants  $C_{caesium}$  come from the deviation of the measured Caesium signals from the expected values, interpreted as gain variations. Each scan takes about 8 hours, and is conducted every few months.
- Laser System [52]: The laser system monitors the response of the PMTs and electronic components by sending a controlled amount of light onto the photocathode of each PMT while no collisions are taking place. The calibration constants  $C_{laser}$  are derived from the deviations in the channel response with respect to its reference response. This calibration is usually conducted twice a week.
- Integrator System: The dominating processes in the LHC are soft parton interactions - Minimum Bias (MB) events. The integrator system of each PMT integrates the response over time and measures the average signal of the MB interactions during proton-proton collisions. The variation between minimum bias events, Caesium systems and

---

<sup>1</sup>analog-to-digital converter

the Laser measurements can be interpreted as a loss of efficiency of the scintillators by radiation damage. This allows a determination in the variation of LHC luminosity [53].

- Charge - Energy conversion factor: A factor,  $C_{ADC \rightarrow GeV}$  to convert charge to EM scale energy was determined from electron beam measurements in 2001-2003 [54].

The final reconstructed energy for each TileCal channel in GeV from the raw response,  $A(ADC)$  is then given by:

$$E[GeV] = A(ADC) \cdot C_{ADC \rightarrow pC} \cdot C_{Cs} \cdot C_{laser} \cdot C_{pC \rightarrow GeV} \quad (3.4)$$

Figure 3.6 shows the different calibrations applied, and the various signal paths in the TileCal depending on the signal source. The partially overlapping signal paths allows for cross checks of the calibration systems.

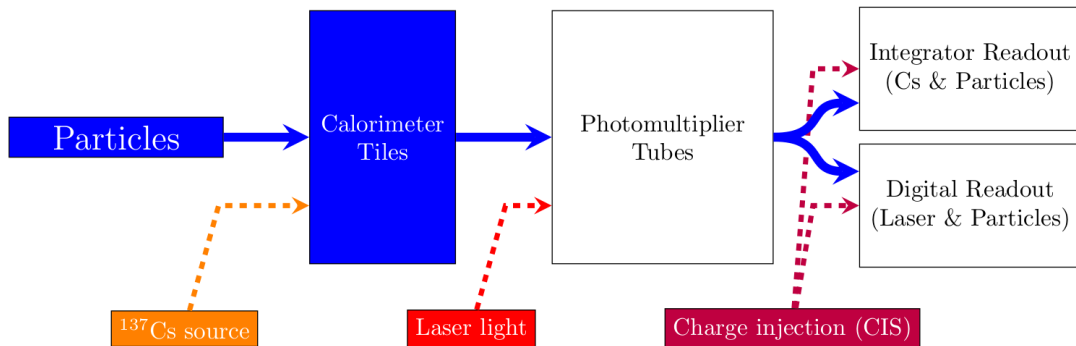


Figure 3.6: Flow diagram of the readout signal path of the different TileCal calibration systems [2].

## Muon System

The muon system detects muons, measuring their momenta based upon the deflection of tracks by the toroid magnets. It is composed of separate trigger and high-precision tracking

chambers. The chambers are arranged in three cylindrical layers around the beam axis in the barrel region, and in three planes perpendicular to the beam axis in each of the end-cap regions. Precise measurement of track coordinates is provided by Monitored Drift Tubes (MDTs) and, at large pseudorapidities, Cathode Strip Chambers (CSCs).

The MDTs consist of a pressurised drift tube ( $\sim 30$  mm diameter) containing an argon/carbon-dioxide gas mixture at 3 bar. Ionisation electrons are collected in a central wire. The MDT chambers are rectangular in the barrel and trapezoidal in the end-cap. Shapes and dimensions of the chambers were chosen to optimise solid angle coverage, while considering the dimensions of the magnet system, support structures and access ducts.

The MDTs are considered safe up to counting rates of about  $150 \text{ Hz/cm}^2$ , which is exceeded at high  $\eta$ . In these high flux regions, the MDTs are replaced with CSCs able to cope with counting rates up to  $\sim 1000 \text{ Hz/cm}^2$ . The CSC system consists of two disks with eight chambers each (eight small and eight large). Each chamber can produce four independent measurements in  $\eta$  and  $\phi$  along each track from four separate CSC planes.

The trigger system covers the pseudorapidity range  $|\eta| < 2.4$ . The trigger chambers are designed to provide fast information on muon tracks traversing the detector, so that the L1 trigger can quickly recognise their multiplicity and approximate energy range. It consists of Resistive Plate Chambers (RPCs) in the barrel, and Thin Gap Chambers (TGCs) in the end-caps. The RPCs are arranged in three concentric layers around the beam axis. They consist of two parallel resistive plates separated by 2 mm with an electric field between them. This allows avalanches to form along ionising tracks towards the anode, allowing a signal to be read out via capacitive coupling to metallic strips mounted on the outer faces of the plates. The TGCs provide both trigger capability, and also complement the MDTs in determining the azimuthal coordinate in the radial direction. TGCs are multi-wire proportional chambers containing a highly quenching gas mixture, designed to provide high granularity, good time resolution, and high rate capabilities.

### Trigger System

Data storage and processing remains a key challenge at ATLAS. The integrated luminosity is expected to total more than  $300 \text{ fb}^{-1}$  by the end of Run 3. This data set is intended to provide ATLAS physicists the ability to make precise measurements of Higgs production rates and properties and search a very large phase space for evidence of BSM physics, while also helping to improve the measurement of many SM physics processes. To satisfy these diverse demands, the Trigger and Data Acquisition system (TDAQ) provides comprehensive and efficient coverage of Higgs and SM physics, and serves the requirements of the various BSM physics searches while managing the limitations of data storage and processing at ATLAS.

A two level trigger system is employed, a hardware-based first level trigger (L1 trigger) and a software-based high level trigger (HLT). This system has been in place since the start of run 2, during the LHC run 1 (2009 - 2013) a three-stage system (with two-stage HLT) was used. The run 2 L1 trigger is capable of a data rate of 100 kHz, while the HLT is capable of a data rate of 1 kHz [55].

The rate of low- $p_T$  and multi-jet triggers is strongly affected by pile-up, which also degrades the jet resolution. For generic single- and multi-jet triggers, full calorimeter read-out allows more accurate determination of jet energies using the full offline jet calibration procedure. This includes both pile-up suppression and correction, allowing the HLT thresholds to be placed very close to the offline thresholds. The full read-out also allows iterative event-level jet-finding algorithms, such as the anti- $k_t$  algorithm, to be used.

## Chapter 4

# Data Quality

Data quality is maintained by the careful selection of triggers and data quality cuts, outlined below. These are intended to provide maximum statistics possible, whilst minimising background, and ensuring events pass certain quality cuts. The strategy employed in the quark-gluon tagged searches follows from the standard non-tagged dijet search [56]: event selection is identical, with additional cuts only where QQ, QG and GG enriched samples are created as outlined in Chapter 6.

### 4.1 Triggering

This analysis uses a single jet trigger, which selects events having at least one transverse energy deposit in the calorimeter with a magnitude above a particular threshold. Triggers with particularly low  $p_T$  thresholds have prescale factors ( $p_i$ ) applied: a random subsample of events passing the selection are recorded, with a rate of  $1/p_i$ . In order to maximise the statistics available for this analysis, the non-prescaled trigger with the lowest  $p_T$  threshold is used. This corresponds to a jet  $p_T$  greater than 420 GeV.

Single-jet triggers use a naming convention of ‘Jnnn’ for L1 triggers or ‘jnnn’ for the high level trigger (HLT) - ‘nnn’ is the nominal jet  $p_T$  threshold in GeV. The energy scale of the L1 triggers is the EM scale, while for HLT triggers, a calibration sequence very close to what

is applied to offline jets is applied, bringing their scale to the hadronic scale.

For the complete Run 2 dataset, two single-jet triggers are unrescaled for all data taking: HLT\_j420 and HLT\_j225\_gsc420\_boffperf\_split. Both of these are seeded from the L1\_J100 trigger. Both triggers search for jets with  $p_T > 420$  GeV, while the HLT\_j225\_gsc420\_boffperf\_split trigger additionally applies the normally-offline global sequential calibration (GSC) to improve the trigger turn-on.

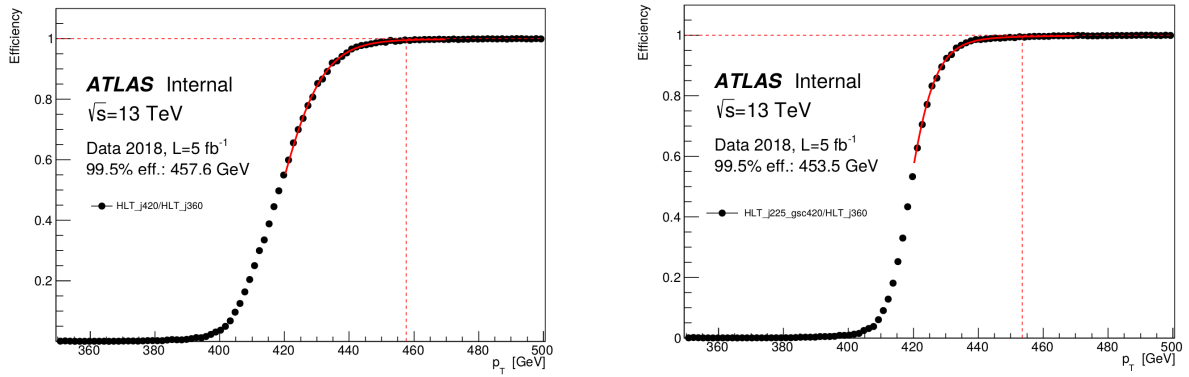
To measure the trigger efficiency in data, an unbiased sample was obtained using the HLT\_j360 trigger - assuming this one is fully-efficient at  $\sim 420$  GeV.  $5 \text{ fb}^{-1}$  of high- $\mu$  2018 pp data were used to measure the turn-ons for trigger and dijet invariant mass,  $m_{jj}$ . Figure 4.1 shows the efficiencies as a function of the jet  $p_T$  for HLT\_j420 and HLT\_j225\_gsc420\_boffperf\_split with a functional fit applied to determine the plateau, defined as the point at which the efficiency reaches above 99.5%. The HLT\_j420 trigger reaches this plateau at 457.6 GeV, HLT\_j225\_gsc420\_boffperf\_split reaches the plateau at 453.5 GeV

## 4.2 Event Selection

In order to maximise the significance of a possible signal, the dominant contribution from QCD processes must be reduced. This is done by applying a kinematic cut on the rapidity difference between the two leading jets, thus selecting central jets:

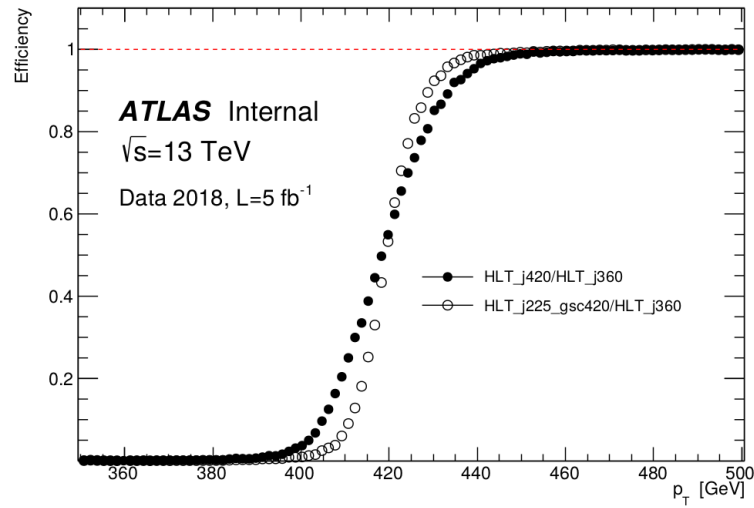
$$y^* = \frac{1}{2}|y_1 - y_2| < 0.6 \quad (4.1)$$

In QCD, gluon exchange diagrams have approximately the same angular dependence as Rutherford scattering, whereas resonant signals and contact interactions are more isotropic [57]. This distinct angular distribution motivates the selection of events with large polar angle (central jets).



(a) HLT\_j420

(b) HLT\_j225\_gsc420\_boffperf\_split



(c) Comparison

Figure 4.1: Trigger efficiencies and their corresponding fits for HLT\_j420 and HLT\_j225\_gsc420\_boffperf\_split triggers as a function of jet  $p_T$  for 2018 data. From Ref. [56].

The dijet invariant mass is fully efficient at 1.1 TeV, within the detector acceptance for which the trigger requirement is met. This corresponds to the lower bound of the  $m_{jj}$  range investigated. The upper bound is determined simply by the highest mass dijet event recorded and passing cuts, this is an event with  $m_{jj} = 8.02$  TeV collected in 2016.

### Good Run List

The standard method for ensuring an analysis uses good data quality is the use of a good run list (GRL). These lists are compiled by the ATLAS Data Quality (DQ) group based on the various data quality flags of the detector subsystems. The DQ flags label a particular luminosity block as either good, flawed or bad. Because the various analyses rely on different subsystems of the detector to be working correctly, the system of DQ flags can be used to assemble different collections of reliable data depending on the particular physics objects under investigation. Each GRL consists of a list of run numbers and luminosity blocks in a combination that satisfies the specification of the particular GRL. An event can be said to pass the GRL when it is included in one of the luminosity blocks in the GRL. The Data Monitoring Quality Framework (DMQF) determines the overall suitability of a run in data analysis and is described in [58].

## 4.3 JET Reconstruction and Calibration

A jet in ATLAS can be defined using a variety of objects, using the tracking information or at calorimeter level. Calibration studies often employ track jets - those reconstructed using the reconstructed tracks and momenta of the inner detector. Jets simulated in Monte Carlo can have known particle level constituents which can be used as input four-vectors to the same jet reconstruction algorithms used in analyses. These “Truth jets” provide a useful tool for calibration of jet reconstruction performance.

This study uses jets defined using topoclusters, a higher-level object compared to calorimeter level, topoclusters consist of a group of topologically connected calorimeter cells. The

Parameter	EM 633	Had 420
Calorimeters	EM only	All
Seed signal definition	E	$ E $
Cluster cut before splitting	$E_T > 5$ GeV	$ E_T  > 0$ GeV
$t_{\text{seed}}$	6	4
$t_{\text{neighbor}}$	3	2
$t_{\text{cell}}$	3	0

Table 4.1: Parameters used to build the two types of topological cluster available in the standard ATLAS reconstruction. From [60].

topological clustering algorithm [59, 60] reconstructs three-dimensional particle showers using the lateral and longitudinal segmentation of the calorimeters. Topoclusters are seeded from calorimeter cells with absolute energy measurements  $|E| > t_{\text{seed}}\sigma_{\text{noise}}$  with  $t_{\text{seed}}$  the chosen seed threshold, and  $\sigma_{\text{noise}}$  the deviation of the expected noise. This noise includes both electronic noise and the expected contribution from pile-up - thus depending on the run conditions. Adjacent cells with  $|E| > t_{\text{neighbor}}\sigma_{\text{noise}}$  are added iteratively to the topocluster, followed by adding all the cells neighbouring the previous set with  $|E| > t_{\text{cell}}\sigma_{\text{noise}}$ .  $t_{\text{cell}} = 0$  implies that all cells neighbouring a seed cell will be included. The set of neighbours can include not only the eight surrounding cells, but also cells overlapping partially in  $\eta$  and  $\phi$  in adjacent layers and/or adjacent calorimeter systems. In ATLAS, the number of neighbouring cells is often  $> 10$  as the granularity varies between different calorimeter layers and regions of the detector. The two types of topological cluster available in the standard ATLAS reconstruction are given in Table 4.1.

The granularity and noise thresholds vary across the different ATLAS calorimeters, but are initially calibrated to the electromagnetic scale (EM scale), which correctly measures the energy deposited in the calorimeter by particles produced in electromagnetic showers. Hadronic interactions produce responses that are lower than this EM scale, the amount depending on where the showers develop. This analysis makes use of jets calibrated to the EM scale, using the “420” set of parameters. The “420” is optimized to find efficiently low energy clusters without being overwhelmed by noise. The cut on absolute energy ensures

the noise contribution is symmetric.

Finally, a splitting step separates at most the two local energy maxima into separate topoclusters. This is important, as clusters can grow to cover large areas of the detector if sufficient energy is present between incident particles. Even in the case of overlapping showers, it may be possible to separate individual particles if the relevant energy maxima can be identified.

The final cluster obtained is kept if its total transverse energy is above some predefined cutoff. The use of topoclusters is intended to suppress noise and the impact of pileup by requiring a minimum energy to expand the clusters, while including soft radiation in the cluster perimeter.

The obtained EMTopo clusters are used as inputs to the anti- $k_t$  jet reconstruction algorithm, described in section 2.3, using a distance parameter ( $R$ ) of 0.4. This algorithm is implemented in the FastJet package [61]. The use of FastJet is motivated by the improvement of performance, due to a reduction in the scaling of the algorithmic complexity of the anti- $k_t$  algorithm from  $N^3$  to  $N \ln N$  for an ensemble of  $N$  particles [62].

### Jet Calibration

Jets reconstructed from calorimeter topoclusters directly do not necessarily possess the true energy of the original parton. Calorimeter cells and associated topoclusters may accurately measure energy deposits from electromagnetic showers, but only poorly measure those from hadronic showers. Other factors contributing to incorrect jet energy measurement include:

- Dead material: Some jet energy may be deposited in unresponsive areas of the detector.
- Leakage: Some energy may escape the calorimeters altogether - *punch through* occurs when showers penetrate the calorimeters and enter the muon system.
- Out of jet cone: Particles in the MC truth jet can end up outside of the reconstructed calorimeter jet, creating a source of energy loss.

- Reconstruction efficiency: The noise threshold requirements of topocluster formation will lead to some energy losses from low energy deposits in the calorimeter cells.

The ATLAS calibration scheme is intended to restore the jet energy scale to that of reconstructed truth jets. Each stage of the calibration (apart from the origin correction) corrects the full four-momentum of the jet, scaling the jet  $p_T$ , energy, and mass. The full procedure is outlined in [63], and shown schematically in Figure 4.2.

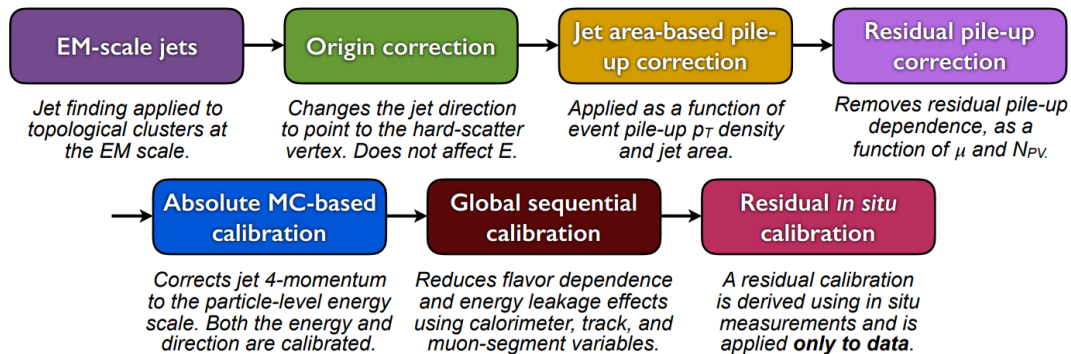


Figure 4.2: Calibration stages for EM-scale jets. From [63].

The directional component assigned to calorimeter cells and topoclusters - and hence to EM-scale jets - points to the geometrical centre of the ATLAS detector. The origin correction recalculates the four-momentum of the jet to point to the hard-scatter primary vertex, while keeping the energy constant. The  $\eta$ -resolution of the jets, measured as the difference between the reconstructed jets and truth jets in MC simulation is improved in this step. Improvements from roughly 0.06 to 0.045 at a jet  $p_T$  of 20 GeV and from 0.03 to below 0.006 for those above 200 GeV are achieved [63].

### Pile-up corrections

The pile-up correction removes excess energy contributions from both in-time and out-of-time pile-up. The pile-up correction methods for Run 2 were developed in 2012 [64]. There

are two components: a data driven area-based  $p_T$  density subtraction [65] and a residual correction derived from MC simulation.

First, the per-event pileup contribution to the  $p_T$  of each jet is subtracted according to its area, calculated from the median  $p_T$  density  $\rho$  of the jets in the  $\eta$ - $\phi$  plane. This uses only positive-energy topoclusters with a central  $|\eta| < 2$  selection clustered with the anti- $k_t$  algorithm. This algorithm is chosen based on its sensitivity to soft radiation, while the central  $|\eta|$  selection is due to the higher calorimeter occupancy in the forward regions.

After the area based subtraction is applied, a dependence of the jet  $p_T$  on pileup remains. An additional residual correction is therefore applied, as a function of the number of primary vertices,  $N_{PV}$ , and  $\langle \mu \rangle$  [66]. This enables both residual in-time and out-of-time effects to be captured. The corrected  $p_T$  of the jet following these pile up corrections is then given by:

$$p_T^{corr} = p_T^{EM} - \rho \times A - \alpha \times (N_{PV} - 1) - \beta \times \langle \mu \rangle \quad (4.2)$$

where  $\alpha$  and  $\beta$  are derived from the observed residual dependence.

### Jet energy scale and $\eta$ -calibration

Biases in the jet  $\eta$  reconstruction arise primarily from the transition between different calorimeter technologies and granularity. The JES calibration is derived from the correction of reconstructed jet energy to truth jet energy from a PYTHIA MC sample after origin and pileup corrections are applied [67].

The average energy response is taken as the mean of a Gaussian fit to the  $E^{\text{reco}}/E^{\text{truth}}$  distribution of the jets, binned in  $E^{\text{truth}}$  and  $\eta_{det}$  - the jet  $\eta$  pointing to the geometric centre of the detector. This produces a result most directly corresponding to the actual calorimeter geometry. A lower energy response due to absorbed and undetected particles can be caused

by gaps and transitions between calorimeter elements. The response in the full ATLAS simulation is shown in Figure 4.3a.

The fitting function for the calibration is defined as [68]

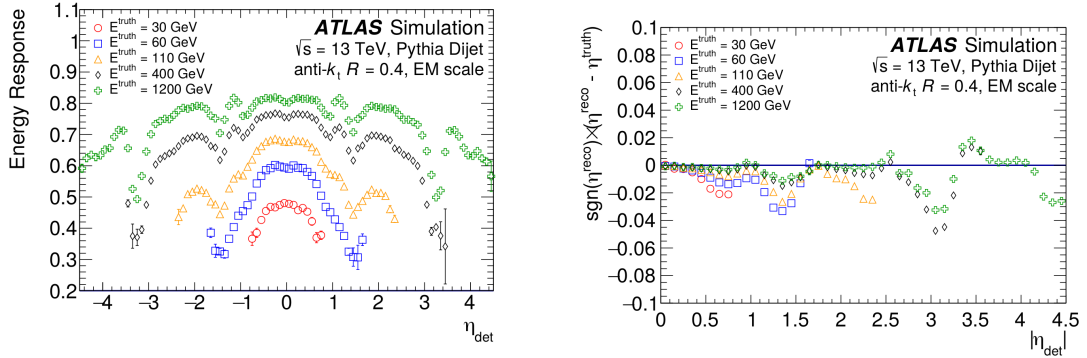
$$\mathcal{F}_{calib,k}(E_{EM}^{jet}) = \sum_{i=0}^{N_{max}} a_{i,k} (\ln E_{EM}^{jet})_k^i \quad (4.3)$$

with the  $a_i$  free fit parameters, and  $N_{max}$  between 1 and 6 depending on the goodness of fit obtained.  $k$  is the specific  $\eta_{det}$  bin.

The corrected jet energy is obtained by scaling the measured jet energy by the value of  $\mathcal{F}_{calib,k}(E_{EM}^{jet})$  in the relevant  $\eta_{det}$  bin,  $k$ :

$$E_{EM+JES}^{jet} = \frac{E_{EM}^{jet}}{\mathcal{F}_{calib,\eta_{det}}(E_{EM}^{jet})} \quad (4.4)$$

Differences are seen between the calculated pseudorapidity of the reconstructed jet  $\eta^{reco}$  and the truth jet pseudorapidity  $\eta^{truth}$ , shown in 4.3b. The bias is largest in jets encompassing different calorimeter regions corresponding to changes in geometry or technology. The impact of such changes is to alter the energy response of one side of the jet compared to the other, thus altering the reconstructed four-momentum. Changes in calorimeter geometry can be clearly identified in Figure 4.3b, for instance the barrel-endcap ( $|\eta_{det}| \sim 1.4$ ) and endcap-forward ( $|\eta_{det}| \sim 3.1$ ) transition regions. A second correction on top of that applied to the jet energy is therefore applied to the jet pseudorapidity, derived as the difference between  $\eta^{reco}$  and  $\eta^{truth}$ , parametrised as a function of  $E^{truth}$  and  $\eta_{det}$ . This step only corrects the jet  $p_T$  and  $\eta$ , not the full four-momentum.



(a) Average energy response at the electromagnetic scale in bins of EM+JES calibrated jet energy as a function of the detector pseudorapidity, after origin and pile-up corrections are applied. (b) The difference between the truth jet  $\eta^{truth}$  and the reconstructed jet  $\eta^{reco}$  due to biases in the jet reconstruction, as a function of the detector pseudorapidity  $|\eta_{det}|$ .

Figure 4.3: Average energy response and  $\eta$  difference between truth and reconstructed jets shown for truth energy of 30, 60, 110, 400, and 1200 GeV [67].

### Global sequential calibration

The calorimeter response and jet reconstruction are sensitive to fluctuations in the jet particle composition and energy distribution. Particle composition and shower shape vary depending on the initiating particles of the jet - notably between quark- and gluon-initiated jets. Quark-initiated jets often include higher  $p_T$  hadrons which penetrate further into the calorimeter, Gluon-initiated jets are expected to contain softer radiation with a wider transverse profile in the calorimeter.

The global sequential calibration (GSC) extends the EM+JES calibration with a multivariate technique. Any variable correlated with the detector response to the jet can be used. The correction to the jet energy measurement comes from inverting the calibrated jet response  $\mathcal{R}$  as a function of this variable

$$C(x) = \frac{\mathcal{R}^{-1}(x)}{\langle \mathcal{R}^{-1}(x) \rangle} \quad (4.5)$$

Parameter	Description	$ \eta_{det} $
$f_{Tile0}$	Fraction of jet energy measured in the first layer of the hadronic Tile calorimeter	$< 1.7$
$f_{LAr3}$	Fraction of jet energy measured in the third layer of the electromagnetic LAr calorimeter	$< 3.5$
$n_{trk}$	Number of tracks with $p_T > 1$ GeV ghost-associated with the jet	$< 2.5$
$\mathcal{W}_{trk}$	Average $p_T$ -weighted transverse distance in the $\eta - \phi$ plane between the jet axis and all tracks of $p_T > 1$ GeV ghost-associated to the jet	$< 2.5$
$n_{segments}$	Number of muon track segments ghost-associated with the jet	$< 2.7$

Table 4.2: The five observables used to improve the resolution of the JES.

where  $x$  is the correlated variable, and  $\langle \mathcal{R}^{-1}(x) \rangle$  is the average inverse jet response [68]. After this stage, the remaining dependence of the response on the variable  $x$  is removed without changing the average energy, by multiplying the numerical inversion with a constant. This improves the resolution through a reduction in the spread of the reconstructed jet energy.

Applying these corrections sequentially for several observables achieves the optimal resolution. This simply requires the correction for a variable  $x_i$  ( $C^i$ ) be applied to jets already corrected with the previous variable  $x_{i-1}$  ( $C^{i-1}$ ). It then follows that the jet transverse momentum after such corrections is given by:

$$p_T^i = C^i(x_i) \times p_T^{i-1} = C^i(x_i) \times C^{i-1}(x_{i-1}) \times p_T^{i-2} = \dots \quad (4.6)$$

Five observables have been identified which improve the resolution of the JES [67], detailed in Table 4.2. No improvements were found by including correlations of the observables or by altering their sequence.

The  $n_{segments}$  correction is motivated by high- $p_T$  jets not being fully contained within the calorimeter. These punch-through jets in the  $p_T$ -weighted track width increase the tails of the response distribution. It is more correlated with the energy escaping the calorimeters,

and so is derived as a function of energy. The other four parameters are derived as a function of  $p_T$ .

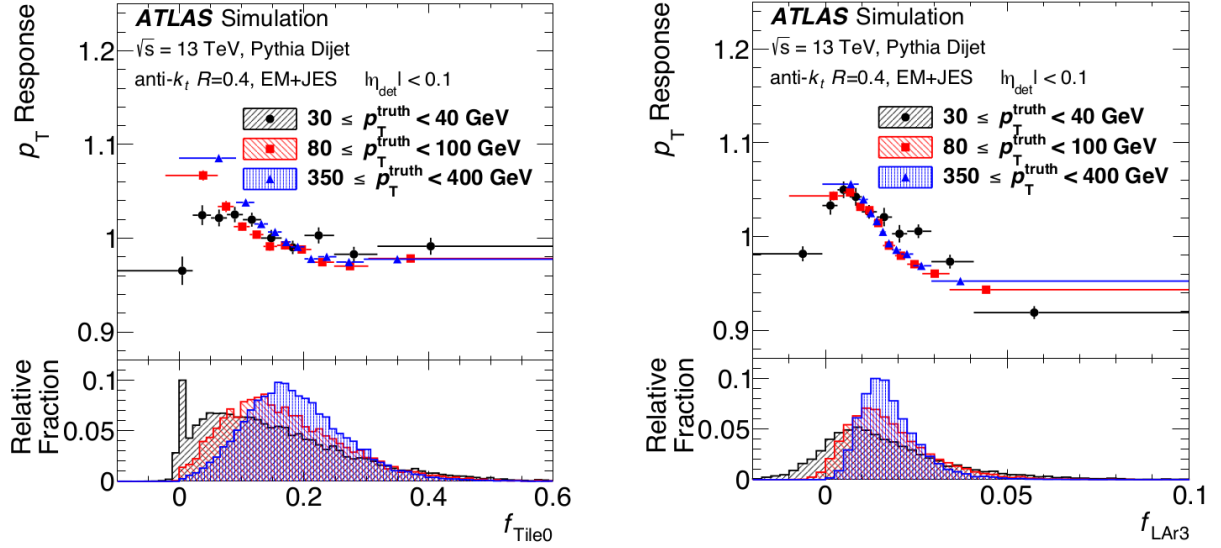
MC simulation has been able to model the underlying distributions of these variables well [67]. The dependence of the average jet response on the observables was tested using the dijet tag-and-probe method detailed in Ref. [68], Section 12.1. The average  $p_T$  asymmetry between back-to-back jets was measured with 2015 data as a function of each observable, with data and MC found to be in agreement, with differences small compared to the sizes of the proposed corrections.

After applying the full GSC, jet response dependence on each observable is reduced to less than 2%. Small deviations from unity reflect correlations between observables unaccounted for in these corrections [67].

### **In situ calibration**

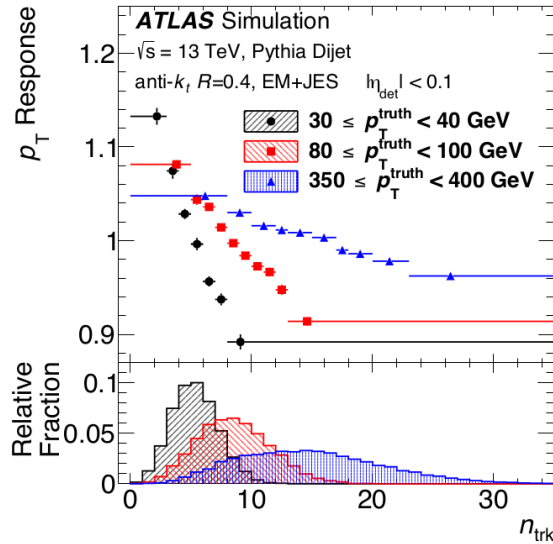
The final stage of calibration is intended to account for the differences between data and MC simulation using a well measured set of reference objects. Differences can arise from the imperfect description of the detector material and response in MC, as well as imperfect simulation of the hard scatter, underlying event, pileup, hadronisation and the EM and hadronic interactions within the detector. The correct jet energy is derived from conservation of transverse momentum.

Three separate *in situ* calibrations correct the differences in response of central jets ( $|\eta| < 1.2$ ) for different  $p_T$  regimes, using a different reference object. The direct  $p_T$  balance between a jet and the decay products of a Z boson through the decay channels of  $Z \rightarrow e^+e^-$  and  $Z \rightarrow \mu^+\mu^-$  is used for a transverse momentum of  $20 < p_T < 500$  GeV, where Z boson production is statistically significant. The  $\gamma$ +jet calibration is limited by the relatively small number of events at high  $p_T$ , as well as contamination through the dijet channel and an artificial reduction of the number of events coming from the prescaled triggers used at low  $p_T$ . The  $\gamma$ +jet calibration is therefore used between  $36 < p_T < 950$  GeV, with the multijet



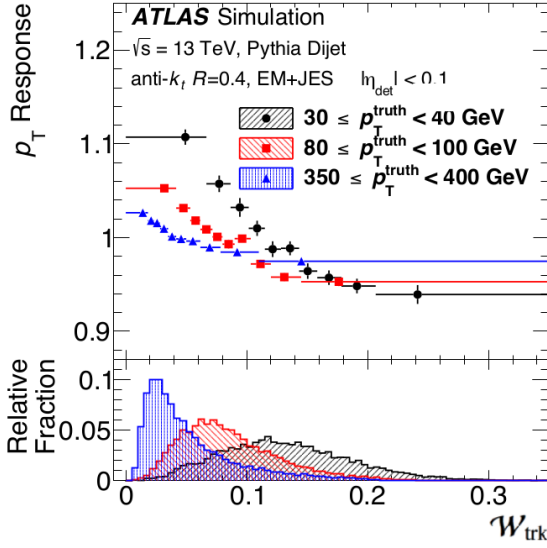
(a) Average jet response in MC simulation as a function of fractional energy in the first Tile calorimeter layer.

(b) Average jet response in MC simulation as a function of fractional energy in the third LAr calorimeter layer.

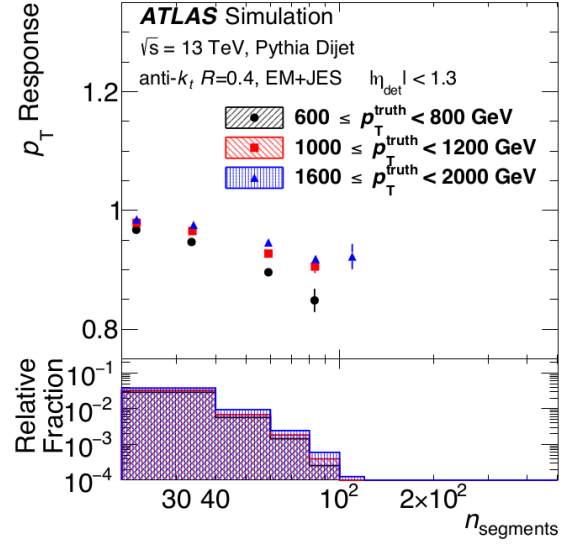


(c) Average jet response in MC simulation as a function of the number of tracks with  $p_T > 1$  GeV ghost-associated with the jet.

Figure 4.4: The average jet response in MC simulation as a function of the GSC variables for three ranges of truth jet  $p_T$ . Jets are constrained to  $|\eta| < 0.1$  for the distributions of calorimeter and track-based observables and  $|\eta| < 1.3$  for the muon  $n_{segments}$  distribution. The distributions of the underlying observables in MC simulation are shown in the lower panels for each truth jet  $p_T$  region, normalized to unity. The spike at zero in the  $f_{Tile0}$  distribution of Figure 4.4a at low  $p_T^{truth}$  reflects jets that are fully contained in the electromagnetic calorimeter and do not deposit energy in the Tile calorimeter. The negative tail in the  $f_{LAr3}$  distribution of Figure 4.4b and in the  $f_{Tile0}$  distribution of Figure 4.4a at low  $p_T^{truth}$  reflects calorimeter noise fluctuations. Figures from [67].



(a) Average jet response in MC simulation as a function of the  $p_T$ -weighted track width.



(b) Average jet response in MC simulation as a function of the number of muon track segments per jet.

Figure 4.5: The average jet response in MC simulation as a function of the GSC variables for three ranges of truth jet  $p_T$ . Jets are constrained to  $|\eta| < 0.1$  for the distributions of calorimeter and track-based observables and  $|\eta| < 1.3$  for the muon  $n_{\text{segments}}$  distribution. The distributions of the underlying observables in MC simulation are shown in the lower panels for each truth jet  $p_T$  region, normalized to unity. Figures from [67].

balance used up to a  $p_T$  of 2 TeV. In this multijet analysis, topologies with three or more jets are selected, which balance a single high- $p_T$  jet against a recoiling set of several lower- $p_T$  jets. In this selection, the recoil jets are of sufficiently low  $p_T$  to be able to be calibrated by the  $z/\gamma$ +jet calibrations.

An  $\eta$ -intercalibration uses dijet events to correct the average response of forward jets ( $0.8 < |\eta_{det}| < 4.5$ ) to that of better measured central jets ( $|\eta_{det}| < 0.8$ ).

For each *in situ* calibration, a response  $\mathcal{R}_{\text{in situ}}$  is defined as the average ratio of jet  $p_T$  to the reference object  $p_T$ , binned in regions of the reference object  $p_T$ , for both data and MC. The calorimeter response to EM+JES jets, gluon radiation, and energy loss outside of the jet cone will affect  $\mathcal{R}_{\text{in situ}}$ , such impacts are mitigated by the event selections. Assuming such effects are well modelled in MC, the ratio  $c$  is used as an estimate of the ratio of the

JES in data and MC, where

$$c = \frac{\mathcal{R}_{insitu}^{data}}{\mathcal{R}_{insitu}^{MC}} \quad (4.7)$$

The calibration constants derived in each of the analyses (Z+jet,  $\gamma$ +jet, multijet, and  $\eta$ -intercalibration) from Equation 4.7 are combined to produce the final *in situ* calibration, taken as the numerical inversion of this combination, as a function of jet  $p_T$  and jet  $\eta$ . These are shown in Figures 4.4 and 4.5.

The data-to-MC ratio (and associated systematic uncertainties) from the Z+jet,  $\gamma$ +jet, and multijet calibrations are combined in overlapping regions of  $p_T$  [67]. The result is a common data-to-MC ratio finely binned in  $p_T$ , through interpolation with second-order polynomial splines, shown in Figure 4.6. A  $p_T$ -dependent weight is ascribed to each *in situ* method, according to a  $\chi^2$  minimisation with the response ratios and uncertainties in each  $p_T$  bin as input. Weights are correspondingly higher in  $p_T$  regions of smaller bin size and relative uncertainty. Statistical fluctuations are minimised by smoothing with a sliding Gaussian kernel.

The combined *in situ* correction (taken as the inverse of the combined data-to-MC correction) is 4 % at low  $p_T$ , decreasing to 2 % at 2 TeV. Individual *in situ* corrections show good agreement with each other in areas of overlapping  $p_T$ , when quantified,  $\sqrt{\chi^2/N_{dof}}$  is generally below 1 [63].

### Jet energy scale uncertainties

The Jet Energy Scale contributes the largest individual uncertainty for most jet analyses. The final calibration includes 80 JES systematic uncertainty terms propagated through the individual calibrations and studies. The majority of these (67) come from the Z+jet,  $\gamma$ +jet, and multijet *in situ* calibrations, accounting for the assumptions made in the event topology, MC simulation, sample statistics, and electron, muon, and photon energy scales [63, 70, 71].

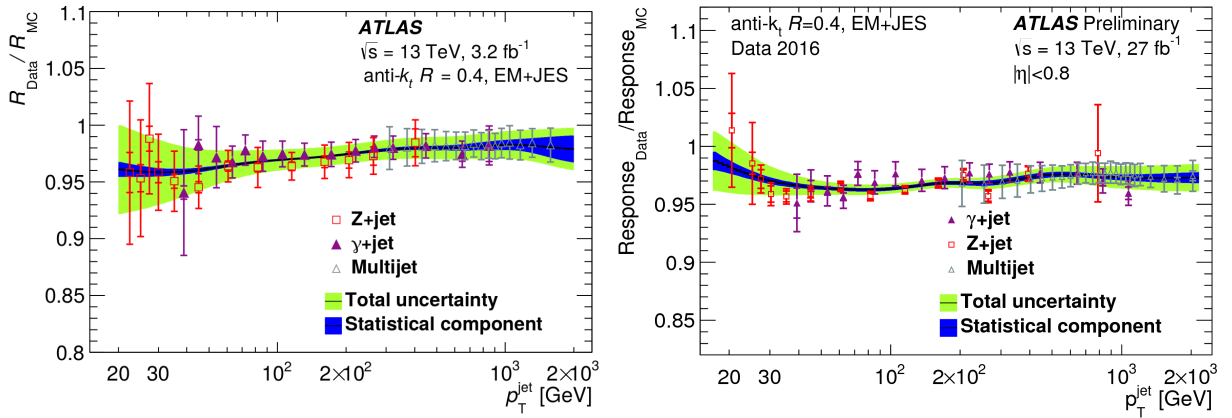


Figure 4.6: Combined data-to-MC EM+JES jet response ratio for Z+jet,  $\gamma$ +jet, and multijet channels. The final derived correction is shown as the black line. Statistical (dark blue band) and total (light green band) uncertainties are also shown. The original ratios are shown with their original binning. From [63, 69].

The systematic uncertainties in the *in situ* calibrations are averaged and smoothed in the same combination procedure as the calibration, achieved through an interpolation [67, 68]. A summary of the systematic uncertainties in the JES from the *in situ* calibration is provided in Table 4.3.

Due to the smooth variations between the results of the *in situ* methods, a linear interpolation is sufficient. Each source of uncertainty is coherently shifted by  $1\sigma$ , with the method's original binning, before the binning interpolation and combination are repeated. The systematic uncertainties are treated as independent and fully correlated across  $p_T$ . The difference in treating the correlations before and after the combination was found to be negligible [63], while treating the systematic uncertainties as independent allows for the flexibility of alternative correlation assumptions at a later stage. Each component of the *in situ* calibration systematic uncertainties is smoothed with a sliding Gaussian kernel.

Sometimes, within a  $p_T$  bin, the different nominal corrections will disagree, defined as those bins with a tension factor  $\sqrt{\chi^2/N_{dof}} > 1$ . In this case, the uncertainty from each source is scaled by this tension factor.

Name	Description
<b>Z + jet</b>	
Electron Scale	Uncertainty in the electron energy scale
Electron resolution	Uncertainty in the electron energy resolution
Muon scale	Uncertainty in the muon momentum scale
Muon resolution (ID)	Uncertainty in muon momentum resolution in the ID
Muon resolution (MS)	Uncertainty in muon momentum resolution in the MS
MC generator	Difference between MC event generators
JVT	Jet vertex tagger uncertainty
$\Delta\phi$	Variation of $\Delta\phi$ between the jet and Z boson
2nd jet veto	Radiation suppression through second-jet veto
Out-of-cone	Contribution of particles outside the jet cone
Statistical	Statistical uncertainty over 13 regions of jet $p_T$
<b><math>\gamma</math>+jet</b>	
Photon scale	Uncertainty in the photon energy scale
Photon resolution	Uncertainty in the photon energy resolution
MC generator	Difference between MC event generators
JVT	Jet vertex tagger uncertainty
$\Delta\phi$	Variation of $\Delta\phi$ between the jet and photon
2nd jet veto	Radiation suppression through second-jet veto
Out-of-cone	Contribution of particles outside the jet cone
Photon purity	Purity of sample in $\gamma$ +jet balance
Statistical	Statistical uncertainty over 15 regions of jet $p_T$
<b>Multijetbalance</b>	
$\alpha^{MJB}$ selection	Angle between leading jet and recoil system
$\beta^{MJB}$ selection	Angle between leading jet and closest subleading jet
MC generator	Difference between MC event generators
$p_T^{asymmetry}$ selection	Second jet's $p_T$ contribution to the recoil system
Jet $p_T$ threshold	Jet $p_T$ threshold
Statistical components	Statistical uncertainty over 16 regions of $p_T^{leading}$
<b><math>\eta</math>-intercalibration</b>	
Physics mismodelling	Envelope of the MC, pile-up, and event topology variations
Non-closure	Non-closure of the method in the $2.0 <  \eta_{det}  < 2.6$ region
Statistical component	Statistical uncertainty

Table 4.3: Summary of the systematic uncertainties in the JES [63] from in situ calibration.

The remaining 13 uncertainties come from sources other than the three *in situ* methods outlined above.

The  $\eta$ -intercalibration method introduces three uncertainties, the effect of potential mis-modeling of the physics, the non-closure of the method between  $2.0 < |\eta_{det}| < 2.6$ , and a statistical component.

Additional sources of systematic uncertainties are shown in Table 4.4. Four systematic uncertainties,  $N_{PV}$ ,  $\mu$ ,  $\rho$ , and the residual  $p_T$  dependence come from correcting MC simulations for pileup.

Three uncertainties come from the differences in the jet response and simulated composition of jets initiated from light-quarks, b-quarks, and gluons. The flavour response uncertainty is derived by comparison of the average jet response for each jet flavour for different MC generators, PYTHIA and Herwig++. The flavour composition uncertainty is analysis dependent.

The GSC punch-through correction uncertainty is taken as the maximum difference in the jet responses between data and MC as a function of muon segments.

The non-closure in absolute JES calibration of fast-simulation jets (those produced using FastCaloSim/AFII [72] MC samples). The MC samples used in this analysis use FastCaloSim only for the signal samples, the background samples use the full GEANT4 [73] ATLAS detector simulation.

The most relevant systematic uncertainty for very high  $p_T$  jets in the dijet resonance search comes from calibrating the calorimeter response in this  $p_T$  regime. Jets with  $p_T > 2$  TeV are beyond the scope of the *in situ* methods, as there are too few jets in the data for these techniques. Instead, a single hadron response calibration needs to be used. Minimum bias data samples are used to provide examples of the jet energy scale per single isolated hadron. The type of particle corresponding to each energy deposit in a jet is then identified, and the energy calibrated from the single particle responses. This uncertainty was found to be 2–5% for jets with transverse momenta above 2 TeV [74].

Name	Description
<b>Pile – up</b>	
$\mu$ offset	Uncertainty of the $\mu$ modelling in MC simulation
$N_{PV}$ offset	Uncertainty of the $N_{PV}$ modelling in MC simulation
$\rho$ topology	Uncertainty of the per-event $p_T$ density modelling in MC simulation
$p_T$ dependence	Uncertainty in the residual $p_T$ dependence
<b>Jetflavor</b>	
Flavour composition	Uncertainty in the jet composition between quarks and gluons
Flavour response	Uncertainty in the jet response of gluon-initiated jets
b-jet	Uncertainty in the jet response of b-quark-initiated jets
Punch-through	Uncertainty in GSC punch-through correction
AFII non-closure	Difference in the absolute JES calibration using AFII
Single-particle response	High- $p_T$ jet uncertainty from single-particle and test-beam measurements

Table 4.4: Additional systematic uncertainties in the JES [63]. Uncertainties from electron, photon and muon energy scales from [70, 71]

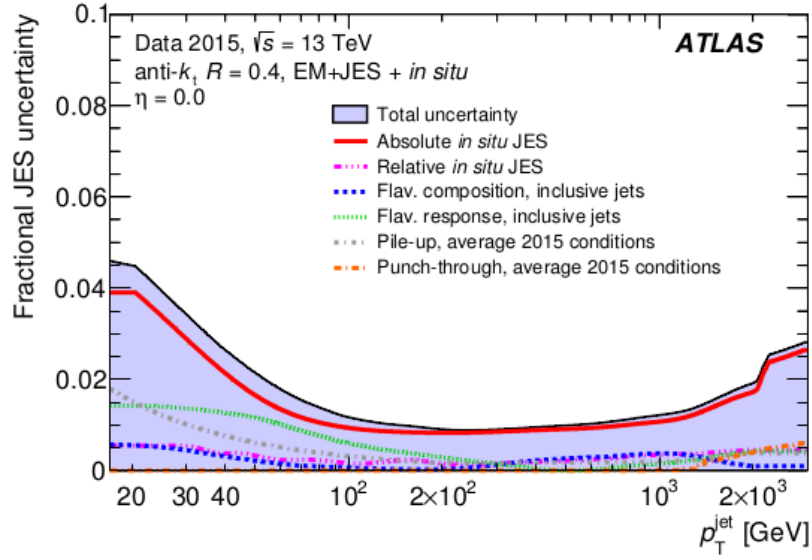
The full combined uncertainty in the JES is shown in Figure 4.7. The uncertainty is largest at low  $p_T$ , decreasing to  $\sim 1\%$  at 200 GeV, before rising at high  $p_T$  due to the end of the multijet balance measurements and the single particle response contributing larger uncertainties.

#### 4.4 Jet energy resolution uncertainties

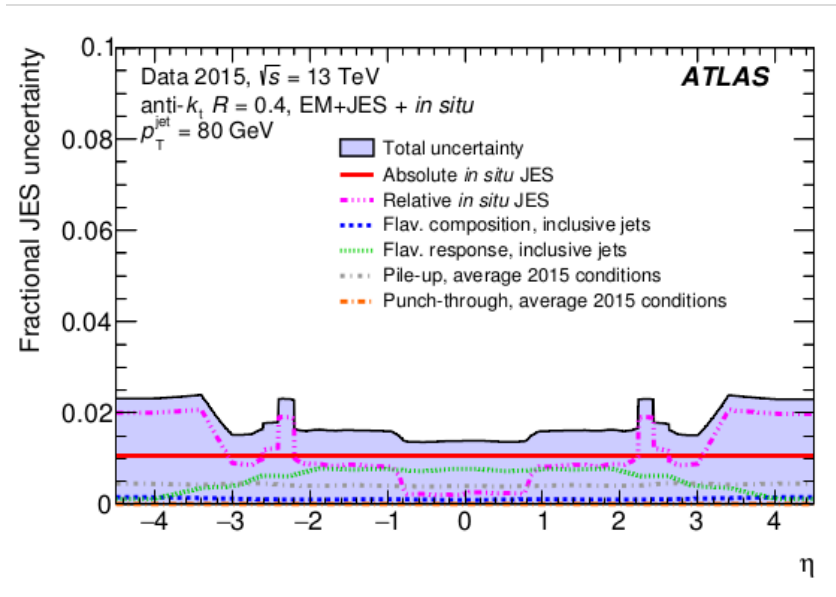
Inaccuracies in the simulation of the detector resolution gives rise to uncertainties in the jet energy resolution ( $\sigma(E)/E$ ). The jet energy resolution is measured *in situ* with two different techniques, the dijet balance method and the bisector method [75]. These methods exploit the fact that at fixed rapidity, the fractional jet energy resolution is equivalent to the fractional jet  $p_T$  resolution ( $\sigma(p_T)/p_T$ ).

The dijet balance method relies on momentum conservation in the transverse plane, with the asymmetry between the transverse momenta of the leading two jets defined by

$$A(p_{T,1}, p_{T,2}) \equiv \frac{p_{T,1} - p_{T,2}}{p_{T,1} + p_{T,2}} \quad (4.8)$$



(a)



(b)

Figure 4.7: Combined uncertainty of fully calibrated jets in the JES as a function of (a) jet  $p_T$  at  $\eta = 0$ , and (b) jet  $\eta$  at  $p_T = 80$  GeV [63].

where  $p_{T,1}$  and  $p_{T,2}$  are the transverse momenta of the two leading jets. A Gaussian fit to  $A(p_{T,1}, p_{T,2})$  characterises the asymmetry distribution and thus  $p_T$  resolution through its width,  $\sigma(A)$ . The relationship between  $\sigma(A)$  and the fractional jet resolution is given by

$$\sigma(A) = \frac{\sqrt{\sigma^2(p_{T,1}) + \sigma^2(p_{T,2})}}{\langle p_{T,1} + p_{T,2} \rangle} \simeq \frac{1}{\sqrt{2}} \frac{\sigma(p_T)}{p_T}. \quad (4.9)$$

An azimuthal cut between the leading jets helps ensure only back-to-back event topologies are included ( $\Delta\phi(j_1, j_2) \geq 2.8$ ), in addition to a veto on the third jet momentum ( $p_{T,3}^{EM} < 10\text{GeV}$ ). Further to these cuts, a soft radiation correction is applied, to account for the presence of soft particle jets not detected in the calorimeter. This correction varies from  $\sim 25\%$  at events with  $\bar{p}_T = 50\text{ GeV}$ , to  $\sim 5\%$  for  $\bar{p}_T = 400\text{ GeV}$ <sup>1</sup> [76].

The bisector method uses the projection of the vector sum of the transverse momenta of the leading jets on to the coordinate system bisector of the azimuthal angle between the individual transverse momentum vectors of the two jets. This is illustrated in Figure 4.8.

In a perfectly balanced dijet system,  $\vec{p}_T = 0$ . A number of effects can cause variations in this value however, for instance initial state radiation causing isotropic fluctuations in the  $\eta$ - $\phi$  plane.

## 4.5 Jet Cleaning

Reconstructed jets can originate either from the hard-scatter proton-proton collisions which are of interest for this analysis, or can come from unwanted non-collision background processes. It is therefore important to distinguish between these types of object. In ATLAS, this is achieved by the implementation of selection criteria referred to as jet cleaning [3, 78].

Jet cleaning is specifically targeted at three types of background:

---

<sup>1</sup> $\bar{p}_T$  is the average  $p_T$  of the leading two jets, ( $\bar{p}_T \equiv p_{T,1} + p_{T,2} / 2$ )

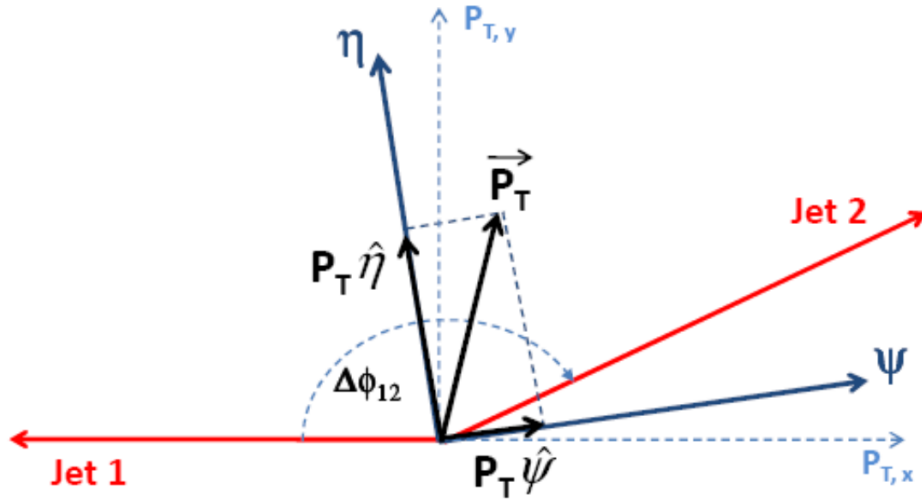


Figure 4.8: Variables used in the bisector method: The  $\eta$ -axis corresponds to the azimuthal angular bisector of the dijet system, while the  $\Psi$ -axis is orthogonal to the  $\eta$ -axis. Both these axes are transverse to the beam axis. Figure from [77].

- Beam induced background (BIB) [79]: The LHC beam pipe is not a perfect vacuum<sup>2</sup>, some scattering will take place between protons and gas particles, which can lead to a background in the detector. The proton halo can also contribute, since some fraction of the halo will interact with collimators in the vicinity of ATLAS and produce showers which can interact with the calorimeters.
- Cosmic ray showers: Atmospheric interactions with cosmic rays produce showers. Although the ATLAS detector is 100 m below ground, some high energy muons produced in these showers can penetrate far enough to reach the detector.
- Calorimeter noise: Isolated pathological calorimeter cells and even large scale coherent noise can be produced by the calorimeter. Cells which produce such noise are masked, either permanently, or on an event-by-event basis for cells which are only sporadically

<sup>2</sup>In the presence of a nominal beam, the cold regions of the beam pipe are of order  $10^{-9}$  mbar  $N_2$ -equivalent, where the equivalence of the most abundant gases ( $H_2$ ,  $CO$ ,  $CO_2$  and  $CH_4$ ) to molecular nitrogen is used for simplicity, based on the equivalence calculated based on the inelastic cross section at beam energy [79].

noisy<sup>3</sup>. A small fraction of this calorimeter noise remains undetected after the data quality inspection, and this needs to be removed by additional criteria.

Several jet quality variables are defined to discriminate between the fake and good jets, based on the calorimeter signal pulse shape, energy ratio and track-based variables [68, 79].

### Calorimeter noise variables

The characteristic ionisation signal shape in the liquid argon (LAr) calorimeters is used to discriminate between real and fake energy deposits. These are the electromagnetic calorimeter, the hadronic end-cap calorimeter and the forward calorimeter. Simulation of the electronics response is used to generate the expected pulse shape, which can then be compared to the actual pulse shape. The discrimination is based on the quadratic difference between the pulse shapes:

$$Q_{cell}^{LAr} = \sum_{j=1}^4 (s_j - A \cdot (g_j - \tau g'_j))^2 \quad (4.10)$$

where  $A$  is the measured amplitude of the signal, defined in Section 3.1.2 of [80],  $\tau$  is the measured time of the signal,  $s_j$  is the amplitude of each of four samples,  $j$ , in ADC counts,  $g_j$  is the normalised predicted ionisation shape and  $g'_j$  its derivative. Several jet-level quantities are defined from  $Q_{cell}^{LAr}$ :

- $\langle Q \rangle$ , the normalised average jet quality: The energy-squared weighted average of the pulse quality of the calorimeter cells in the jet.
- $f_Q^{LAr}$ : The fraction of the energy deposited in the LAr calorimeter cells for which a poor signal shape quality was obtained (defined as  $Q_{cell}^{LAr} > 4000$ )

---

<sup>3</sup>The fractions of cells permanently or conditionally masked are each smaller than one part in a thousand.

- $f_Q^{HEC}$ : The fraction of energy deposited in the hadronic calorimeter cells for which a poor signal shape quality was obtained (defined as  $Q_{cell}^{LAr} > 4000$ )

Large fake energy and negative energy deposits can be generated by sporadically noisy calorimeter cells. Summing the energy of all the cells with negative energy provides another variable,  $E_{neg}$ , which has a different distribution for good<sup>4</sup> and fake jets.

The distributions of all of these variables is shown in Figure 4.9, showing clear differences between good and bad jets.

### Energy ratio variables

Beam induced background and calorimeter noise tend to produce jets which are more localised longitudinally in the calorimeters compared to jets from proton-proton collisions. Several variables are defined to take advantage of these differences:

- $f_{EM}$ : The electromagnetic fraction is the ratio of the jet energy deposited in the EM calorimeter to the total energy of the jet.
- $f_{HEC}$ : The electromagnetic fraction is the ratio of the jet energy deposited in the hadronic calorimeter to the total energy of the jet.
- $f_{max}$ : The maximum energy fraction in a single calorimeter layer.

All of these variables produce a predictable smooth distribution with good jets, Figure 4.10. The fake jets show very high or low values for both  $f_{EM}$  and  $f_{HEC}$ , and are distributed mostly at very high values of  $f_{max}$  compared to the good jets.

### Track based variables

Most real jets contain charged hadrons which are reconstructed in the inner tracker and TRT. Several parameters defined in terms of track variables in the ID tracking system have

---

<sup>4</sup>Negative energy may be present in good jets due to electronic and pile-up noise.

been found to discriminate between good and fake jets. The ratio between the jet charged particle fraction ( $f_{ch}$ ) and the jet energy fraction ( $f_{max}$ ) in the layer with maximum energy deposited is such an example. The jet charged particle fraction is defined as the ratio of the scalar sum of the  $p_T$  of the tracks coming from the primary vertex which are associated with the jet, divided by the jet  $p_T$ , and is used as a discriminating variable also.

The distributions of these variables in data and MC are shown in Figure 4.11. Good agreement is observed between data and MC. Figure 4.12 shows the jet charged fraction ( $f_{ch}$ ) as a function of the jet electromagnetic fraction ( $f_{EM}$ ) for samples enriched with good and fake jets. The  $f_{ch} / f_{max}$  is very efficient at discriminating fake jets, which generally have an  $f_{ch}$  close to 0 and  $f_{max}$  close to 1, and jets originating from hard-scatter events, which have preferentially  $f_{ch} > 0$  and  $f_{max} < 1$ .

## 4.6 Quality Cuts

Two main types of selection are used in ATLAS to discriminate the fake jets, the LooseBad and TightBad, based upon the jet variables defined above.

The LooseBad selection was introduced in References [79, 68]<sup>5</sup>, and is designed to provide high good jet efficiency, while maintaining a high level of fake jet rejection. A jet is identified as LooseBad (and hence excluded) if it satisfies any of the following criteria:

- $f_{HEC} > 0.5$  and  $|f_Q^{HEC}| > 0.5$  and  $\langle Q \rangle > 0.8$
- $E_{neg} > 60$  GeV
- $f_{EM} > 0.95$  and  $f_Q^{LAr} > 0.8$  and  $\langle Q \rangle > 0.8$  and  $|\eta| < 2.8$
- $f_{max} > 0.99$  and  $|\eta| < 2$
- $f_{EM} < 0.05$  and  $f_{ch} < 0.05$  and  $|\eta| < 2$

---

<sup>5</sup>LooseBad was called Looser in these references.

- $f_{EM} < 0.05$  and  $|\eta| \geq 2$

The first two criteria are intended to identify fake jets arising from sporadic noise bursts in the HEC. The third selection criteria are intended to filter out coherent noise and isolated pathological cells in the EM Calorimeter. The final selections identify more general sources of noise such as beam-induced background, cosmic ray showers and miscellaneous hardware issues.

The BadTight selection is intended to provide a much higher rejection of fake jets with an inefficiency for selecting good jets of up to a few percent [3]. The TightBad selection extends the LooseBad selections with a single criterion based upon  $f_{ch} / f_{max}$ . A jet is defined as TightBad (i.e. excluded) if it satisfies any of the LooseBad criteria, or if it satisfies:

- $f_{ch} / f_{max} < 0.1$  for  $|\eta| < 2.4$

The jet criteria used in this analysis is summarised in Table 4.5.

## 4.7 Monte Carlo Samples

Searches for new phenomena in ATLAS involve a comparison to a prediction based upon the Standard Model. The event generators used to obtain such predictions use parton shower, hadronisation, and multiple interaction models to enhance fixed-order partonic matrix element events. In doing so, simulated events are as similar as possible to actual collider data. The models themselves are typically either approximations to high-multiplicity perturbative QCD calculations, or utilise a phenomenological approach in the non-perturbative regime, where the physics is not understood from first principles.

The models contain several free parameters which, in order to produce a good description of measured observables, must be optimised. The process of optimisation is referred to as tuning, and several sets of such tunes exist with a focus on specific event topologies and observables.

Jet reconstruction parameters	
Parameter	Value
Algorithm	anti- $k_t$
R-parameter	0.4
Input Constituent	EMTopo
Analysis Release Number	21.2.65
CalibArea tag	00-04-82
Calibration configuration	JES_data2017_2016_2015_Consolidated_EMTopo_2018_rel21.config
Calibration sequence (Data)	JetArea_Residual_EtaJES_GSC_Insitu
Calibration sequence (MC)	JetArea_Residual_EtaJES_GSC_Smear
Calibration configuration (AFII)	JES_MC16Recommendation_AFII_EMTopo_April2018_rel21.config
Calibration sequence (AFII)	JetArea_Residual_EtaJES_GSC
Selection requirements	
Observable	Requirement
Jet cleaning	LooseBad
Batman cleaning	No
$p_T$	>150 GeV
$ \eta $	<5.0

Table 4.5: Jet selection criteria used in this analysis

The ‘‘A14’’ (ATLAS 2014) tune series [81] consists of a set of four tunes performed on four leading-order(LO) parton density functions – CTEQ6L1 [82], MSTW2008LO [83], NNPDF23LO [84], and HERAPDF15LO [85].

The NNPDF23LO PDF set is used in this analysis. Systematic variations on this tune variant have been made using the ‘‘eigentunes’’ method [86], to provide estimates of the systematic uncertainties in the MC modelling<sup>6</sup>.

The data used to generate this tuning includes several ATLAS observables sensitive to the underlying event, jet track properties [87], and other substructure variables [88].

The full simulation must also consider the interactions of the final-state hadrons and the ATLAS detector. The MC events generated with PYTHIA are therefore passed to the GEANT4 software toolkit [73] which simulates these interactions, taking into account the

<sup>6</sup>The eigentunes construction is based on measuring deviations from the central tune along orthogonal directions in the parameter space aligned with the principal axes of the  $\chi^2$  covariance matrix at the central tune point, so that the same increase in  $\chi^2$  is obtained for each deviation

scattering of the various particles in different detector materials, whilst probabilistically determining decay paths based on lifetimes and branching ratios. GEANT4 even simulates the particle interactions with readout electronics and provides a set of digitised signals from each of the simulated detector components. These signals are then processed using the same reconstruction software used for real data.

## 4.8 Data MC comparisons

The processed MC simulation is compared to data for various observables in Figures 4.13-4.16. Good agreement is seen for all observables except for the number of primary vertices, Figure 4.15b corresponding to pileup conditions in the detector. A slight difference is seen, the result of the MC simulation not representing the full run conditions of the data. Current efforts into using the quark-gluon tagging with the full range of run conditions in the MC samples are ongoing.

Figure 4.13 shows the comparisons between data and MC for the difference in jet angle ( $\Delta\phi$ ), the scalar sum of jet momentum (HT), the jet energy (E), and jet angle in the  $\eta$  and  $\phi$  planes. Several kinematic variables are introduced.  $y^*$  measures the angular separation of two jets (in this case, the leading and subleading jets). It is defined in terms of the rapidities,  $y_1$  and  $y_2$  of the two jets,

$$y^* = \frac{y_1 - y_2}{2} \quad (4.11)$$

Due to the different momenta of the interacting particles in a collision, there is often an imbalance in the longitudinal momenta of the jets. This results in a longitudinal boost with respect to the lab frame. The boost,  $y_B$  is defined as

$$\begin{aligned}
y_B &= \frac{y_1 + y_2}{2} \\
&= \frac{1}{2} \ln \left( \frac{x_1}{x_2} \right)
\end{aligned}
\tag{4.12}$$

where  $x_1$  and  $x_2$  are the longitudinal momentum fractions of the incoming partons.

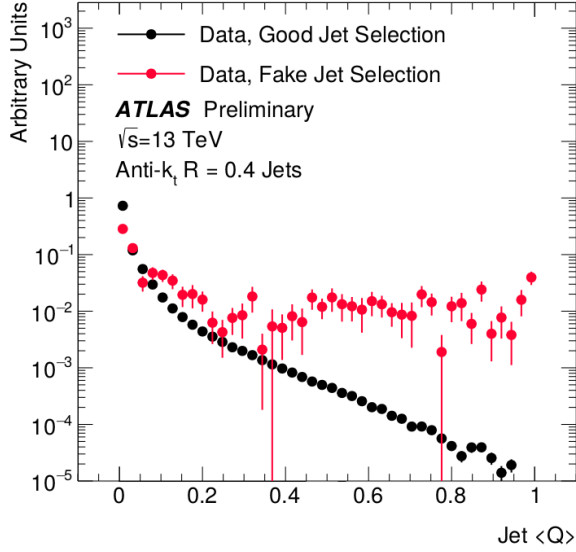
The most important quantity in this analysis is the dijet invariant mass,  $m_{jj}$ , defined as the square root of the sum of the four-vectors of the two jets,

$$m_{jj} = \sqrt{(E_1 + E_2)^2 - |\vec{p}_1 + \vec{p}_2|^2} \tag{4.13}$$

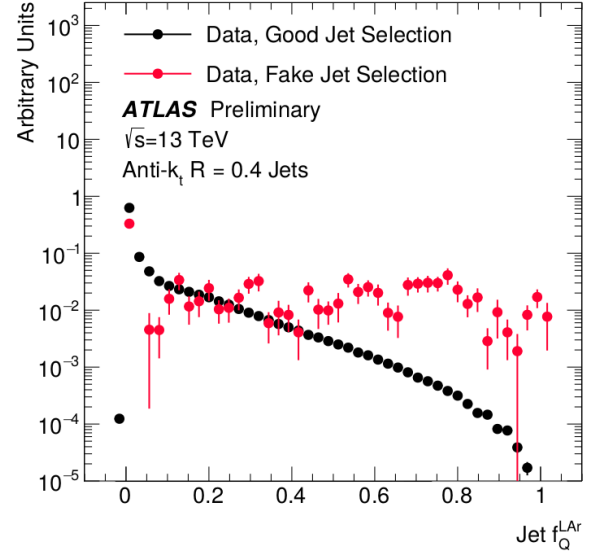
where  $E_1, \vec{p}_1$  and  $E_2, \vec{p}_2$  are the energy and momentum of the leading and subleading jets. It is a Lorentz-invariant quantity which can also be expressed

$$m_{jj} = \sqrt{\hat{s}} = 2p_T \cosh y^* \tag{4.14}$$

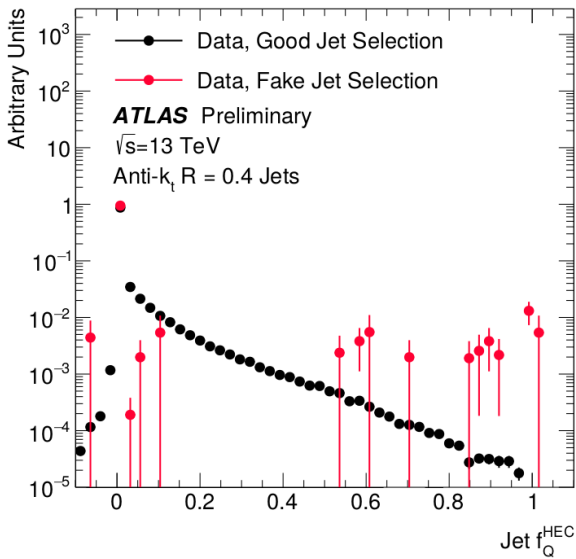
where  $\hat{s} = (p_1 + p_2)^2$  is one of the Mandelstam variables.



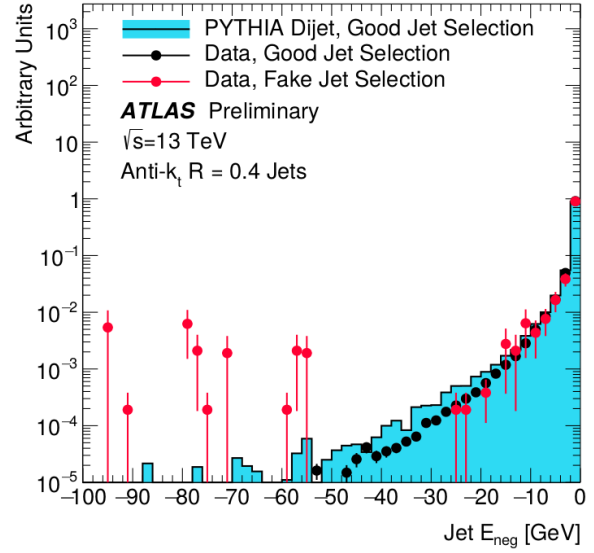
(a)



(b)



(c)



(d)

Figure 4.9: Distributions of (a)  $\langle Q \rangle$ , (b)  $f_Q^{LAr}$ , (c)  $f_Q^{HEC}$  and (d)  $E_{neg}$  for good jets in 2015 data (black points), simulation (blue histogram) and a fake jet enriched sample from 2015 data (red points) [3].

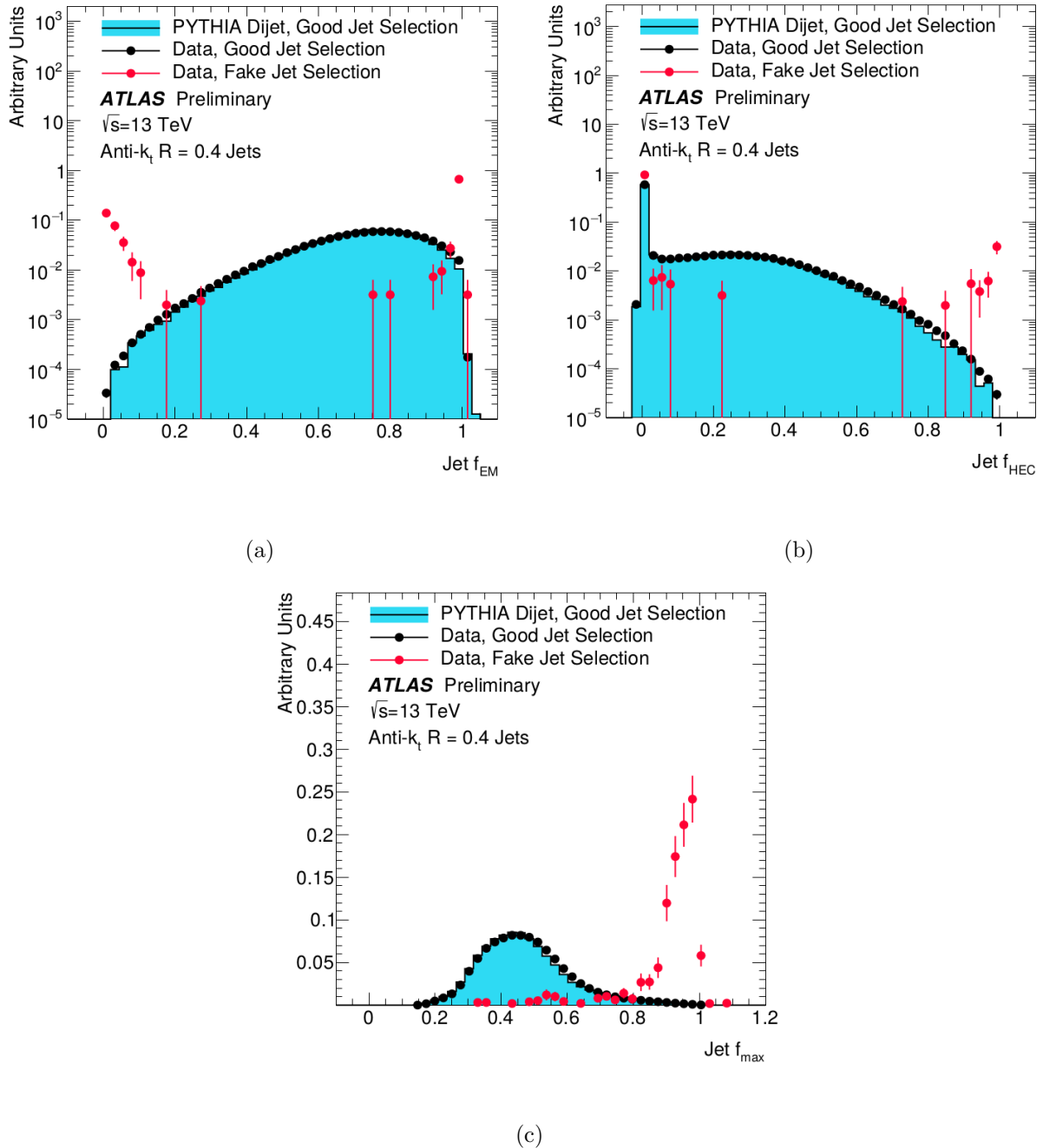


Figure 4.10: Distributions of (a)  $f_{EM}$ , (b)  $f_{HEC}$ , and (c)  $f_{max}$  for good jets in 2015 data (black points), simulation (blue histograms) and a fake jet enriched sample from 2015 data (red points) [3].

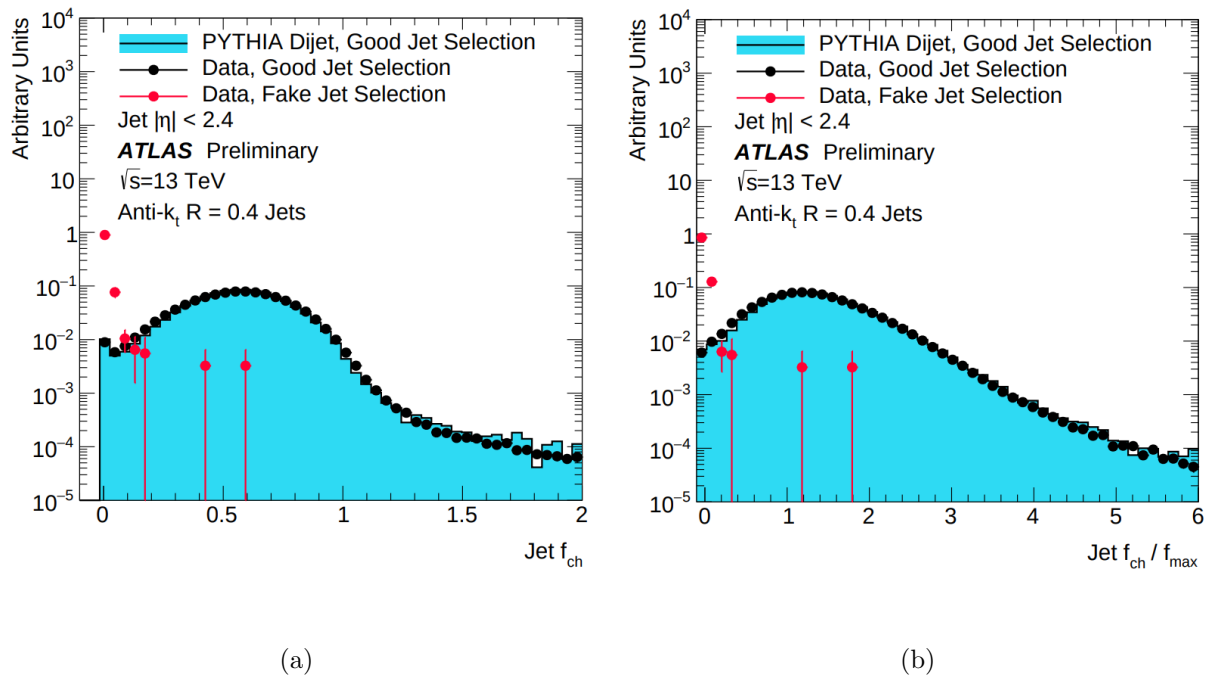


Figure 4.11: Distributions of (a)  $f_{ch}$  and (b)  $f_{ch} / f_{max}$  is very efficient for  $|\eta| < 2.4$  in the good jets enriched sample for both data (black points) and simulation (blue histograms). Distributions from the fake jet enriched samples are also superimposed (red points). From Ref [3].

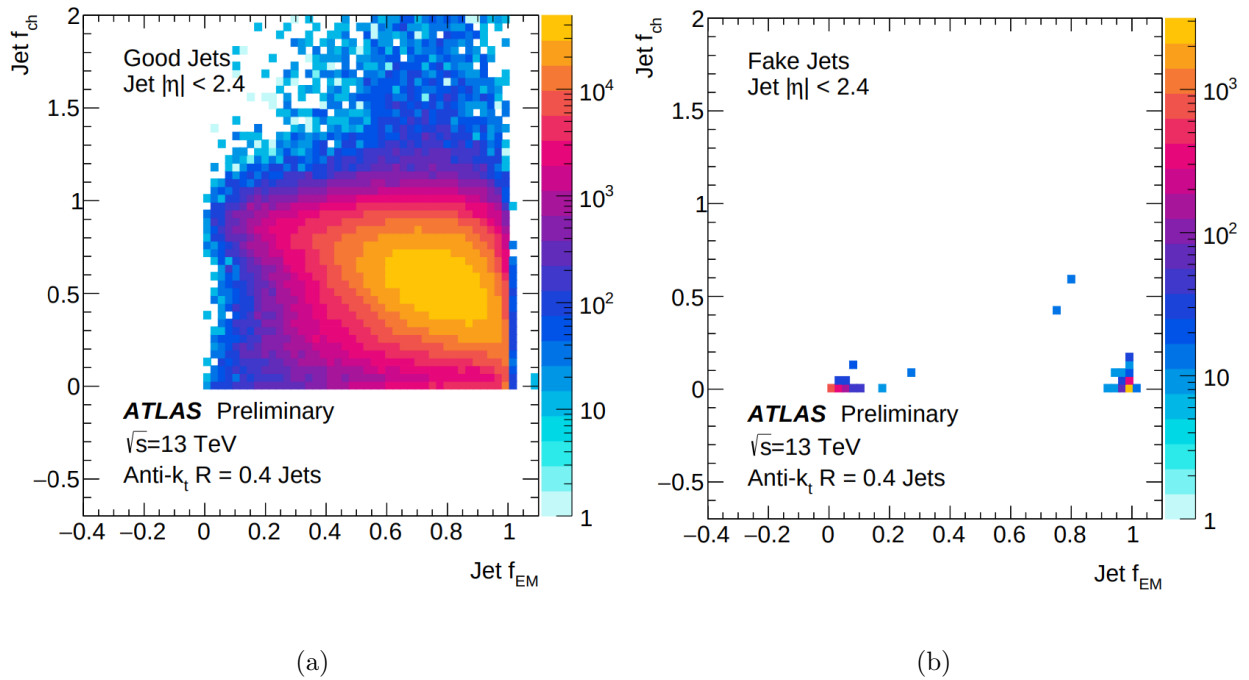
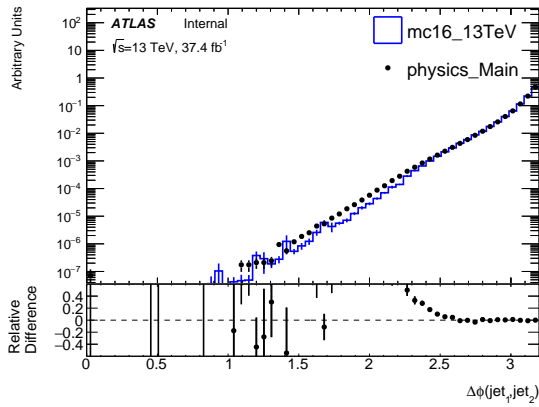
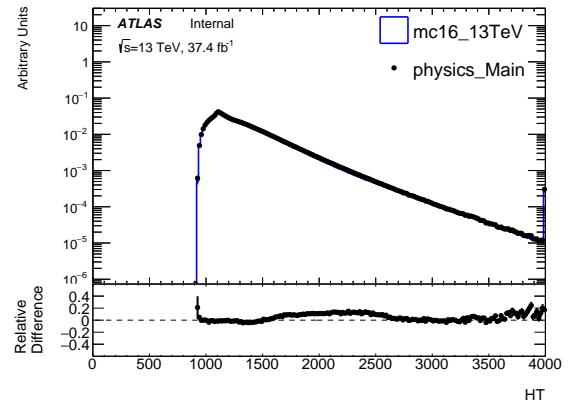


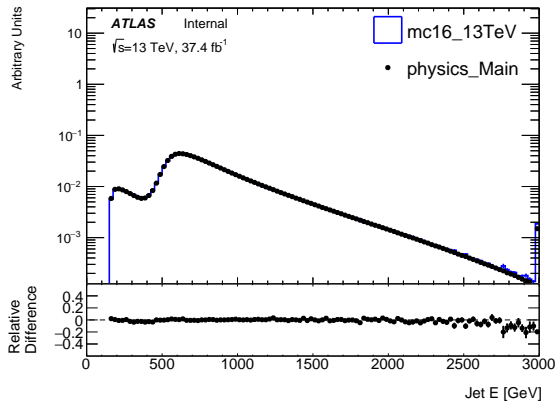
Figure 4.12: Distribution of  $f_{ch}$  as a function of the electromagnetic fraction ( $f_{EM}$ ) for (a) good jets and (b) fake jet enriched samples in data. From Ref [3].



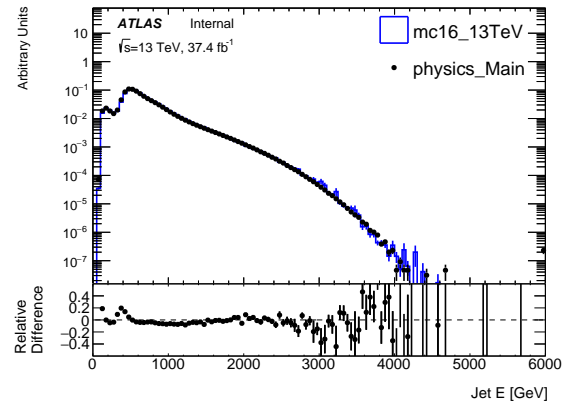
(a)



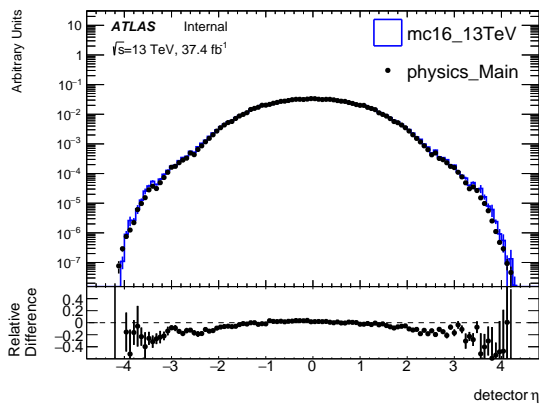
(b)



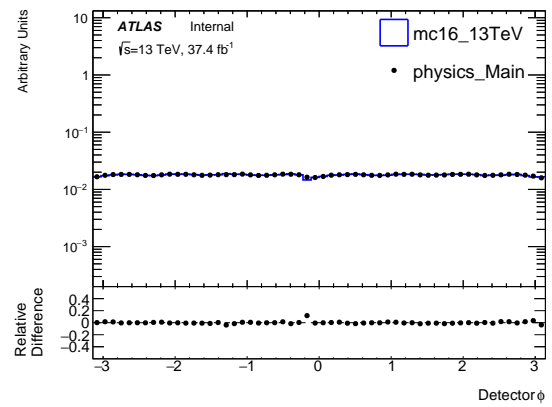
(c)



(d)

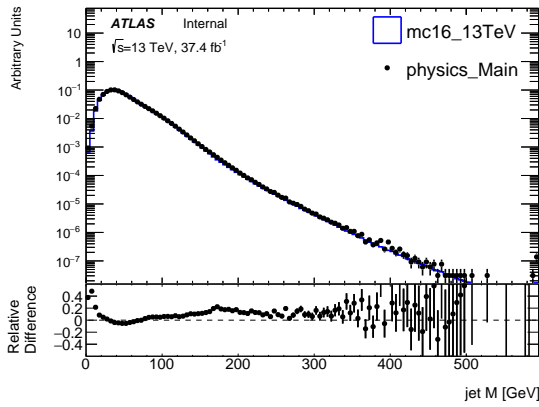


(e)

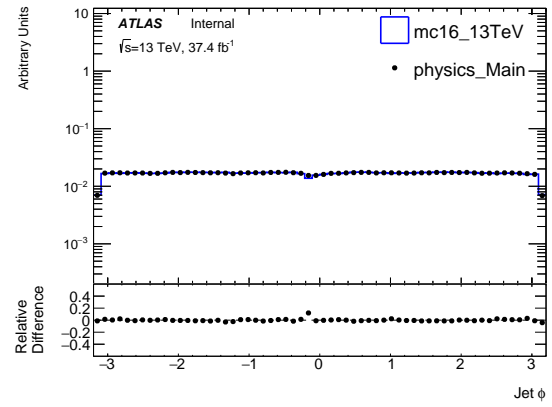


(f)

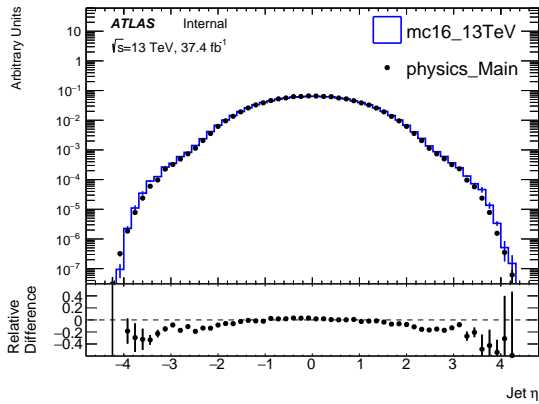
Figure 4.13: Data/MC comparisons for several jet variables: (a) the jet angle ( $\Delta\phi$ ), (b) the scalar sum of jet momentum (HT), (c) the jet energy (E), (d) jet energy at the EM scale, (e,f) jet angle  $\eta$  and jet angle  $\phi$  in the detector.



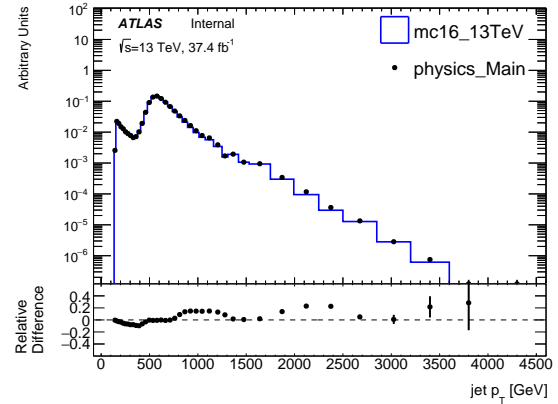
(a)



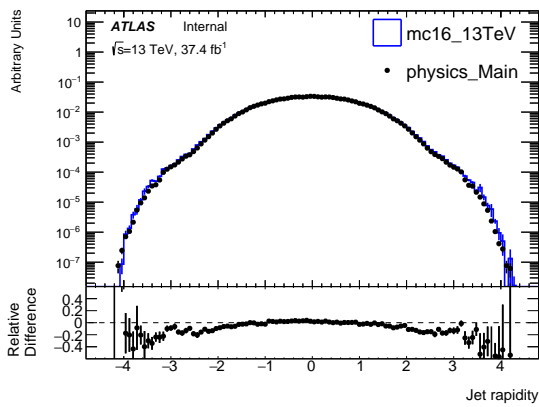
(b)



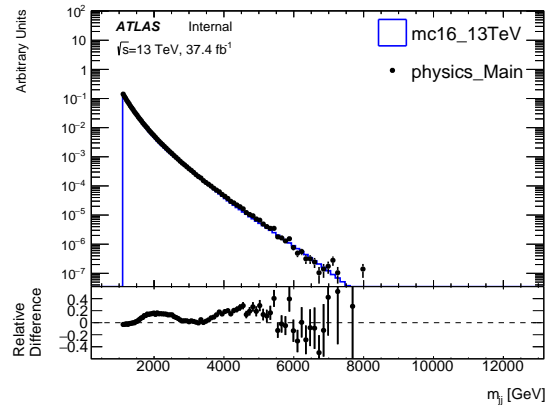
(c)



(d)

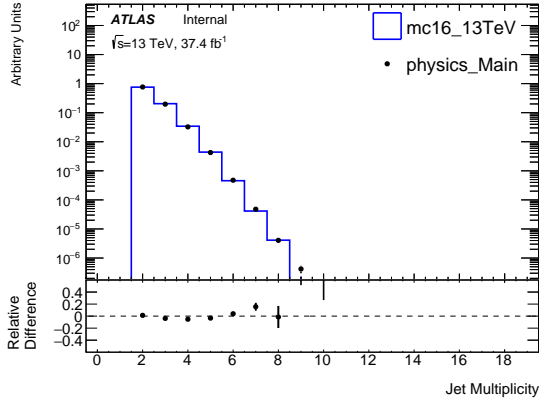


(e)

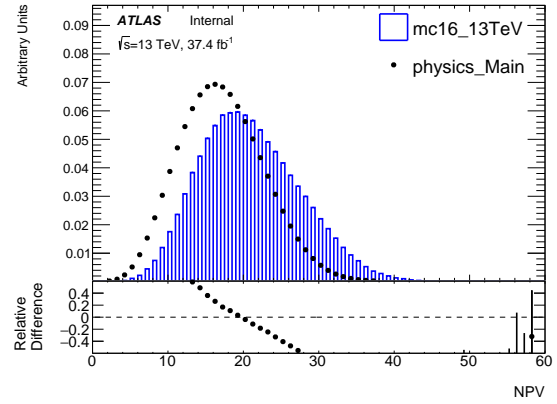


(f)

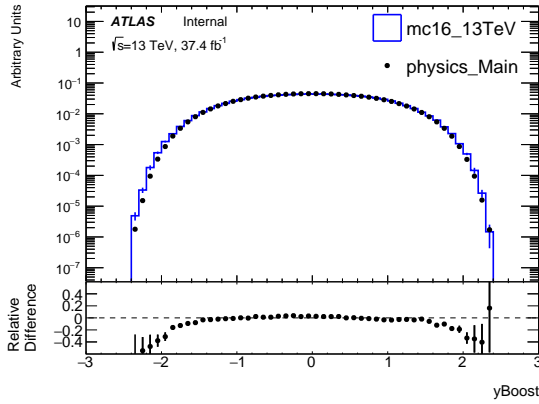
Figure 4.14: Data/MC comparisons for several jet variables: (a) the jet multiplicity ( $M$ ) (b) reconstructed jet angle  $\phi$ , (c) reconstructed jet angle  $\eta$ , (d) jet  $p_T$ , (e) jet rapidity, and (f) the invariant dijet mass spectrum,  $m_{jj}$ .



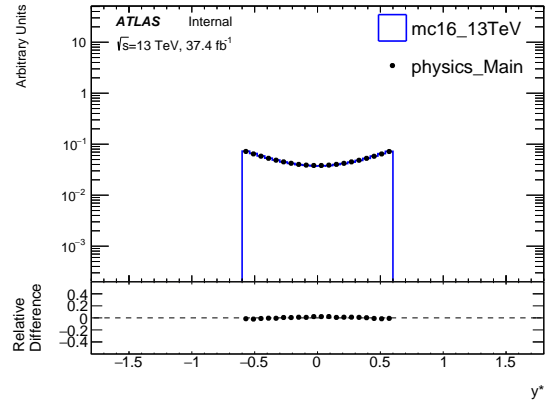
(a)



(b)

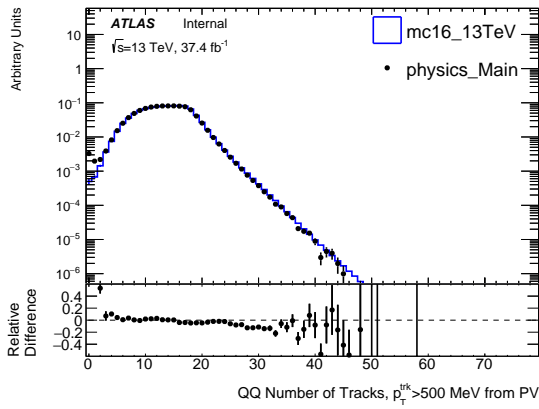


(c)

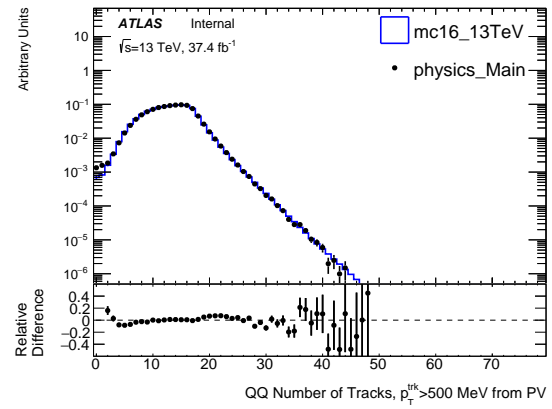


(d)

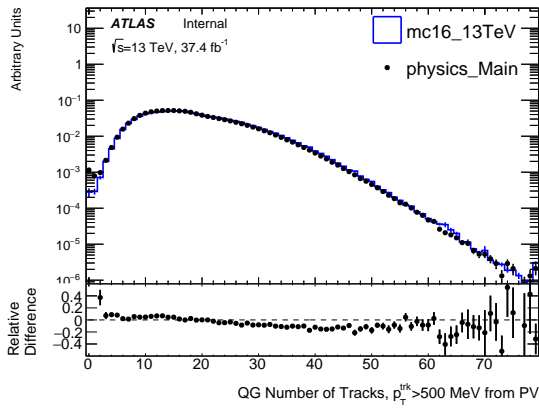
Figure 4.15: Data/MC comparisons for several event variables: (a) number of jets, (b) number of primary vertices, (c) rapidity boost, and (d) the angular separation of the two jets,  $y^*$ .



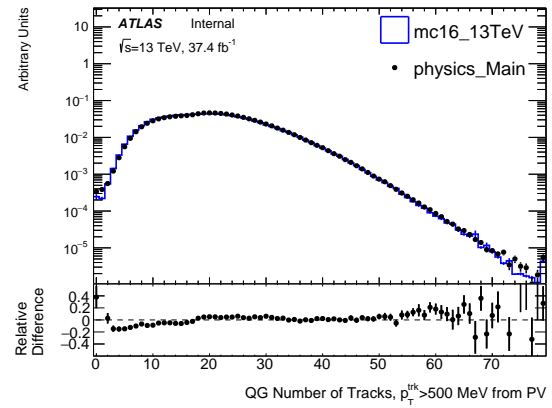
(a)



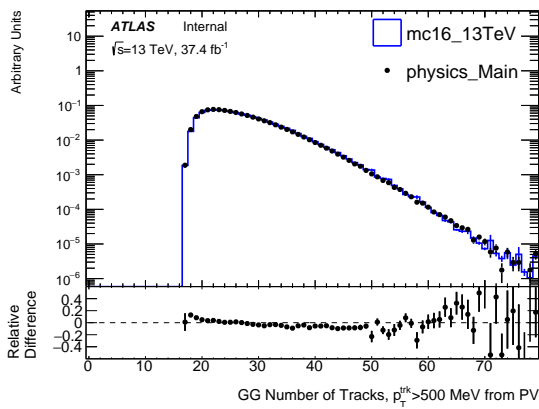
(b)



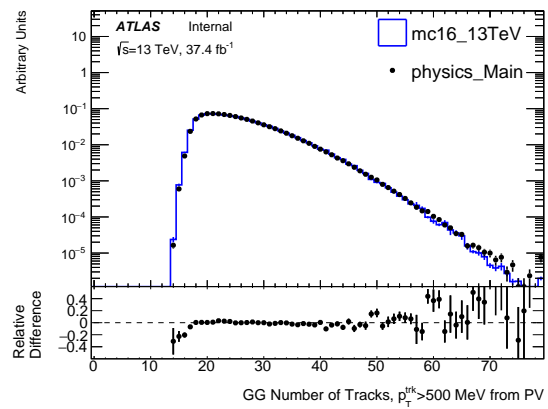
(c)



(d)



(e)



(f)

Figure 4.16: Data/MC comparisons of charged track multiplicity for (a) & (b) QQ, (c) & (d) GG and (e) & (f) GG tagged events, both leading and sub-leading jets.

## Chapter 5

# SWiFt: Fitting the Background

### 5.1 Pseudo Data

The PYTHIA generated MC is smoothed using an algorithm based on 353QH smoothing implemented in ROOT. This process reduces the statistical fluctuations in the generated MC before creating a datalike distribution for sensitivity studies. The 353QH algorithm is described by J. Friedman from the Proceedings of the 1974 CERN School of Computing [89].

In implementing smoothing, one assumes that the true background  $m_{jj}$  spectrum is continuous and does not change dramatically for small changes in  $x$  - assumptions which are also implicit in the use of the background fit functions described in Section 5.2. Any rapid changes in dijet production in MC are therefore attributed to statistical fluctuations in the simulated dataset.

An overlapping average of successive estimates dampens these fluctuations, whilst preserving the underlying shape of the  $m_{jj}$  spectrum. The specific implementation used here uses a series of running medians and means followed by quadratic interpolation.

First, running medians of three are used, yielding no change to monotonic sequences, but moving inward any points which are larger or smaller than both of their neighbours. Taking a sequence of observed values  $\{y_i\}_{i=1}^n$ , we wish to produce a sequence of smoothed values

$\{z_i\}_{i=1}^n$ , where

$$z_i = \text{median}(y_{i-1}, y, y_{i+1}). \quad (5.1)$$

In this first step, the end points are given special treatment, taking

$$z_1 = \text{median}(3z_2 - 2z_3, y_1, z_2) \quad (5.2)$$

$$z_n = \text{median}(z_{n-1}, y_n, 3z_{n-1} - 2z_{n-2}). \quad (5.3)$$

Next, running medians of five are applied, with the exception of the end points, and next-to-end points. The end-points are simply copied, whilst the next-to-endpoints are treated as medians of three. Following this, running medians of three are again applied, again copying the end points. This ‘353’ procedure of running medians performs much of the smoothing of the MC. There are limitations to using this approach alone however, such as monotonically rising and falling sequences being unchanged, and peaks being unnaturally flattened.

The challenge of monotonic sections is dealt with using running means:

$$z_i = \frac{1}{4}z_{i-1} + \frac{1}{2}z_i + \frac{1}{4}z_{i+1} \quad (5.4)$$

while keeping the end points unchanged.

The flattening is remedied by using quadratic interpolation - a quadratic fit is applied through the two points adjacent to the flat, and the point in the flat next to the adjacent point with the largest difference to the value of the flat. The two remaining points are given values corresponding to the quadratic fit.

Although perhaps more robust than necessary for the dijet spectrum, this algorithm also implements ‘twicing’, for smoothing regions with large second derivatives. Twicing consists of smoothing the calculated difference between the original data and the smoothed data produced with the algorithm up to this point, and adding this result to the original smoothing:

$$z = \text{smooth}(y) + \text{smooth}[y - \text{smooth}(y)] \quad (5.5)$$

where  $y$  is the original distribution.

This smoothing procedure is referred to as 353QH, twice.

## 5.2 SWiFt

Resonance searches in the dijet channel have traditionally been conducted by searching for localised excesses of events above a smoothly falling background, see for example Refs [90, 91, 92, 93, 94, 95, 96]. The smooth background has previously been obtained by fitting the dijet mass spectrum with an ad-hoc function, motivated in form by the LO matrix element ( $x^p$ ) and the parton distribution functions ( $(1-x)^p$ ):

$$f(x) = p_0(1-x)^{p_1}x^{p_2+p_3\ln(x)+p_4(\ln(x))^2} \quad (5.6)$$

where the  $p_i$  are the fit parameters and  $x = m_{jj}/\sqrt{s}$ . More than 5 parameters can be added to Equation 5.6 by adding higher order log terms.

This family of functions have been highly successful, however with the increasing luminosity available at the LHC, a global ad-hoc fit to the data becomes increasingly challenging. Figure 5.1 illustrates the problem using data from the low mass dijet spectrum from the Trigger

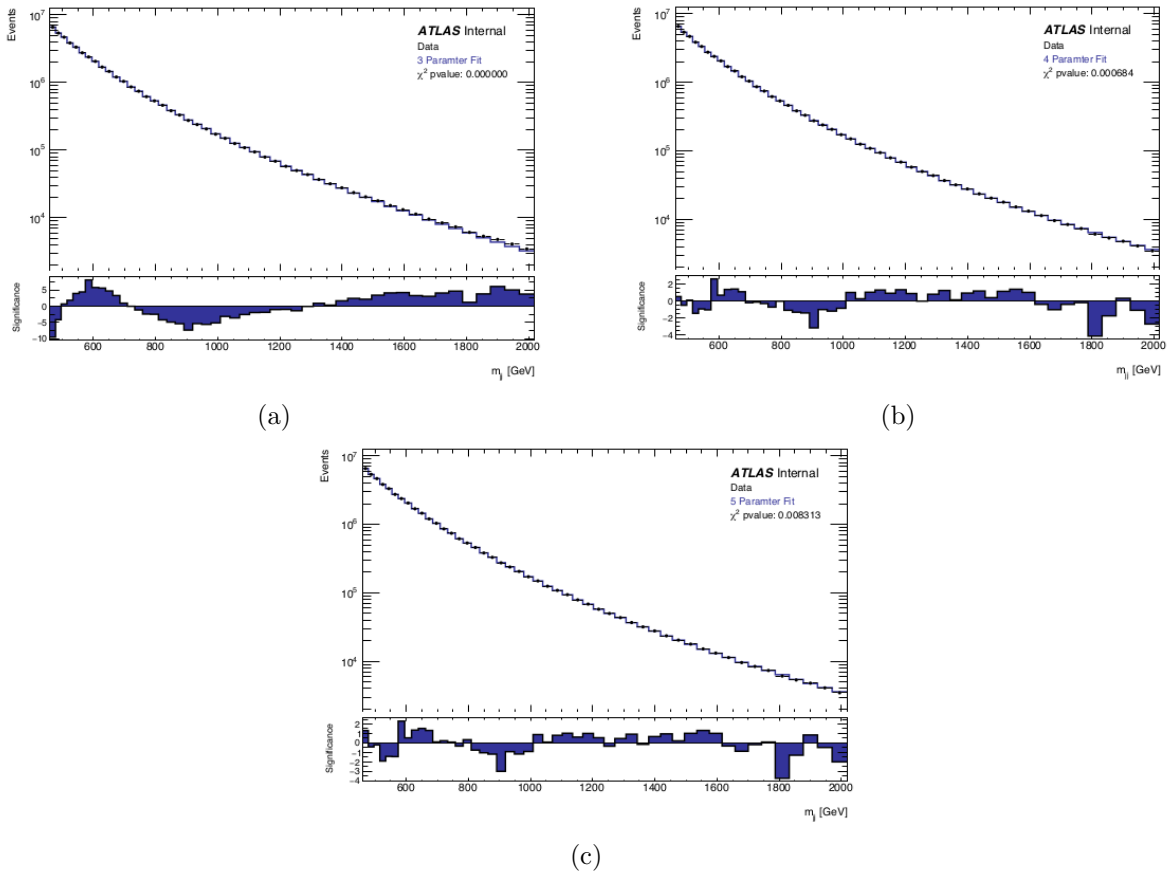


Figure 5.1: Global fits to the  $3.4 \text{ fb}^{-1}$  TLA dijet data are shown here. The functions used are (a) the 3-parameter, (b) the 4-parameter and (c) the 5-parameter dijet functions defined in equation 5.6. The lower panel of the plots shows the statistical significance obtained in  $\sigma$  - the significant swings seen in (a) shows the inability of the 3-parameter function to model the data. The higher order functions (b) and (c) improve the fit to the data, however swings can still be observed in the statistical significance, and none is able to model the region beyond 1 TeV well. From Ref. [98]

Level Analysis (TLA) [97]<sup>1</sup>. Approximately 50 million events are fitted between 450 - 2000 GeV, with fits using the 3, 4 and 5-parameter global fits shown. Improvement is seen using 4 and 5 parameters, however neither manages to adequately model the data beyond 1 TeV, where significances approaching  $4\sigma$  can be seen.

Several solutions for coping with large statistics exist. One could for instance add more

<sup>1</sup>Different cuts and selections are applied in the TLA analysis compared to the high-mass dijet search (see [97]), however the problems encountered when fitting recur in both, and the plots shown here are illustrative of all analyses attempting to fit a large number of events using Equation 5.6

parameters to the function described above, or investigate new functions. An alternative approach is to reduce the fit range. Since the resonances searched for are highly localised, one need not be concerned about fitting the entire data distribution with a single fit. SWIFT is a fitting technique based around the idea of using smaller window sizes over the whole of the distribution, and is now used in the high mass dijet search.

### The SWiFt Background

The SWIFT background is constructed from the data bin-by-bin. In each window, the fit is evaluated at the window centre, providing the background estimate for the central bin. This study uses the same fixed 24 bin window width as the untagged dijet search. This width was found to provide good sensitivity while avoiding over-fitting during signal injection studies. As the window slides across the background distribution bin-by-bin, the complete SWIFT background is extracted by stitching together the evaluations at each window centre. An exception to this procedure is in the first and last windows, in which the SWIFT background for bins below (for the first window) and above (for the final window) are evaluated in addition to the centre bin. This provides the background estimation at the edges of the  $m_{jj}$  distribution.

Some steps from this procedure are shown in Figure 5.2. The red dots are bins which are evaluated as the bin centres of different windows, while the black dots at the edges of the hypothetical distribution are evaluated from the same background fit in the first and last windows (a) and (d) respectively. Figure 5.2 (b) and (c) show intermediate windows in which the SWIFT background is obtained for the central bin only.

### Likelihood Fits

SWIFT determines the parameters in the fit function by minimizing the negative log likelihood (LLH) in each window. The probability of the model given the data is quantified using a Poisson likelihood (LH):

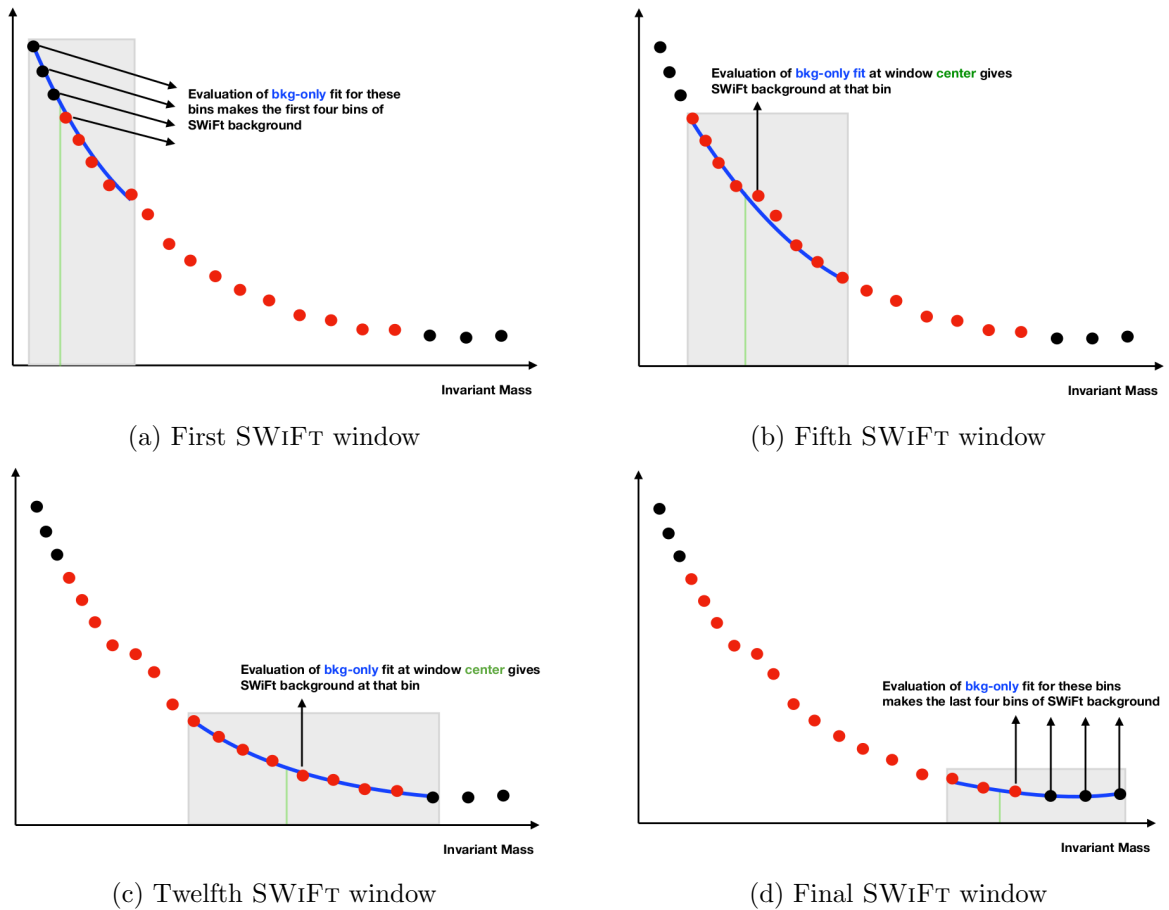


Figure 5.2: Bin-by-bin construction of the SWiFT background for a hypothetical data distribution. Vertical green lines are the window centres which match the bin edges, while the grey boxes represent the window size. Bin edges around the red dots show all the possible window centres, while the black dots are those bins close to the edges. (a) and (d) show the first and last window, where the background fit is evaluated at the window centre and the three edge bins. (b) and (c) show intermediate windows where the background fit is evaluated at the window centres only. From Ref. [99]

$$LH(\vec{p}|x) = \prod_{i=1}^N e^{-\lambda_i(\vec{p})} \frac{(\lambda_i(\vec{p}))^{x_i}}{x_i!} \quad (5.7)$$

where  $\vec{p}$  is the collection of parameters describing the model,  $N$  is the total number of bins, and  $x_i$  and  $\lambda_i$  are the events in the data and histogram respectively in the  $i$ 'th bin.

The negative LLH is used to more easily manage the maximisation of the LH by simplifying the computation, since the negative logarithm reaches its minimum at the same parameter values as the LH function reaches its maximum. The negative LLH is described by a summation over all of the bins:

$$-LLH(\vec{p}|x) = \sum_{i=1}^N [\lambda_i(\vec{p}) - x_i \ln(\lambda_i(\vec{p})) + \ln(x_i!)] \quad (5.8)$$

Minimisation of the LLH can be performed analytically in only the simplest cases. Instead, numerical methods are implemented using a combination of the SIMPLEX and MIGRAD [100] minimisation algorithms. SIMPLEX utilises the Nelder-Mead method [101] to obtain a fit to the background. The parameters found by SIMPLEX are then used as a starting point for the MIGRAD fit, using a variable-metric [102] method. The initial use of SIMPLEX reduces the risk of the MIGRAD fit failing to converge. The uncertainties on the fit parameters are improved using HESSE, which calculates the full second-derivative matrix of the function using a finite difference method.

## Chapter 6

# Signal Selection: Quark-Gluon Tagging

### 6.1 Tagging

The purpose of applying Quark-Gluon tagging to dijet events is to maximise the search potential by maximising the signal/background ratio. An optimal cut on the chosen jet parameter (in this case `nTrack`) must be found by comparing cross section limits obtained for different signal models with a variety of cuts.

Samples with enhanced fractions of quark or gluon initiated jets can be created by using selection criteria based on the charged track multiplicity as shown in Fig. 6.1. The `PYTHIA8` generator using the A14 tune is found to be in a good agreement with the distributions found in data [4].

Previous studies [4] involving quark-gluon tagging have chosen a selection criterion such that each  $p_T$  bin has 60% quark-initiated jet purity. Applying such a selection to the high mass dijet sample would result in discontinuities in the mass spectrum that would present challenges to a resonance search. Several different selection criteria have therefore been investigated, avoiding the presence of such discontinuities.

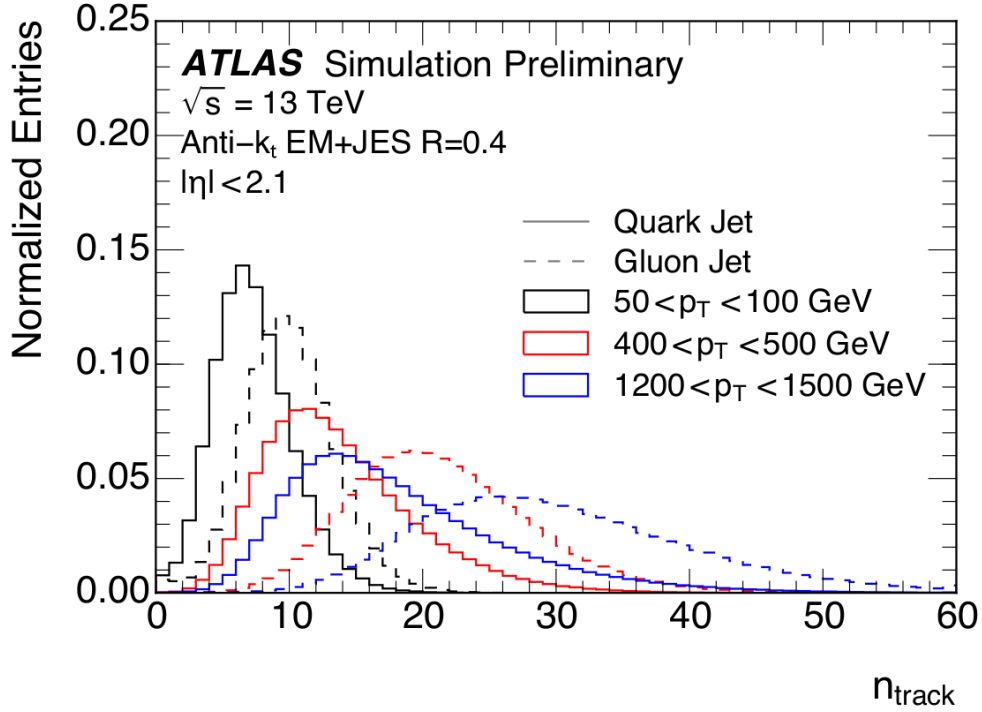


Figure 6.1: Distribution of the jet reconstructed track multiplicity ( $n_{\text{track}}$ ) in different  $p_T$  ranges with the PYTHIA8 generator using the A14 tune [81], the NNPDF2.3 PDF set [84], and processes with a full simulation of the ATLAS detector. Jets must be fully within the tracking acceptance ( $|\eta| < 2.1$ ) and tracks are required to have  $p_T > 500$  MeV and pass quality criteria described in [4]. Figure from [4].

A jet is classified as a quark or gluon jet depending on some threshold of  $n_{\text{track}}$ ,  $n_{qg}$ :

$$\begin{aligned}
 n_{\text{track}} < n_q &: \text{quark-initiated jet} \\
 n_q \geq n_{\text{track}} < n_g &: \text{undefined jet} \\
 n_{\text{track}} \geq n_g &: \text{gluon-initiated jet}
 \end{aligned} \tag{6.1}$$

The implementation of the selection used in Ref. [4] sets  $n_{qg}$  to

$$n_{qg} = \text{int} \left[ \frac{65}{1 + e^{[-0.003(p_T - 1500)]}} + 7 \right] \tag{6.2}$$

where  $p_T$  is measured in GeV, and the function in Eq. 6.2 is truncated so that it is evaluated as an integer. Alternative selection criteria investigated use a linear or log function of the  $p_T$  of the individual jet or the  $m_{jj}$  of the event:

$$n_{qg} = \text{int}[k \times p_T + c] \quad (6.3)$$

$$n_{qg} = \text{int}[k \times m_{jj} + c] \quad (6.4)$$

$$n_{qg} = \text{int}[k \times \ln(p_T) + c] \quad (6.5)$$

where  $k$  and  $c$  are constants chosen to provide suitable sub-samples.

It is possible to use different selection criteria for the quark-initiated and gluon-initiated jets (corresponding to different values of  $m$  and  $c$  in equations 6.3-6.5). This allows for a tighter cut and naturally leads to a third category of jet (undefined), consisting of those jets with track multiplicity between  $n_q$  and  $n_g$ .

These selection criteria are applied to the two leading jets in each dijet event to create three sub-samples, labelled QQ, GG and QG, where both jets are more likely to be quark-initiated, gluon-initiated, or when we are likely to have one of each type respectively. If a selection includes undefined jets, these may be included for a loose selection:

$$\begin{aligned} QQ_{\text{tight}} &= Q + Q \\ QG_{\text{tight}} &= Q + G \\ GG_{\text{tight}} &= G + G \\ QQ_{\text{loose}} &= Q + Q, Q + U \\ QG_{\text{loose}} &= Q + G, Q + U, G + U, U + U \\ GG_{\text{loose}} &= G + G, G + U \end{aligned} \quad (6.6)$$

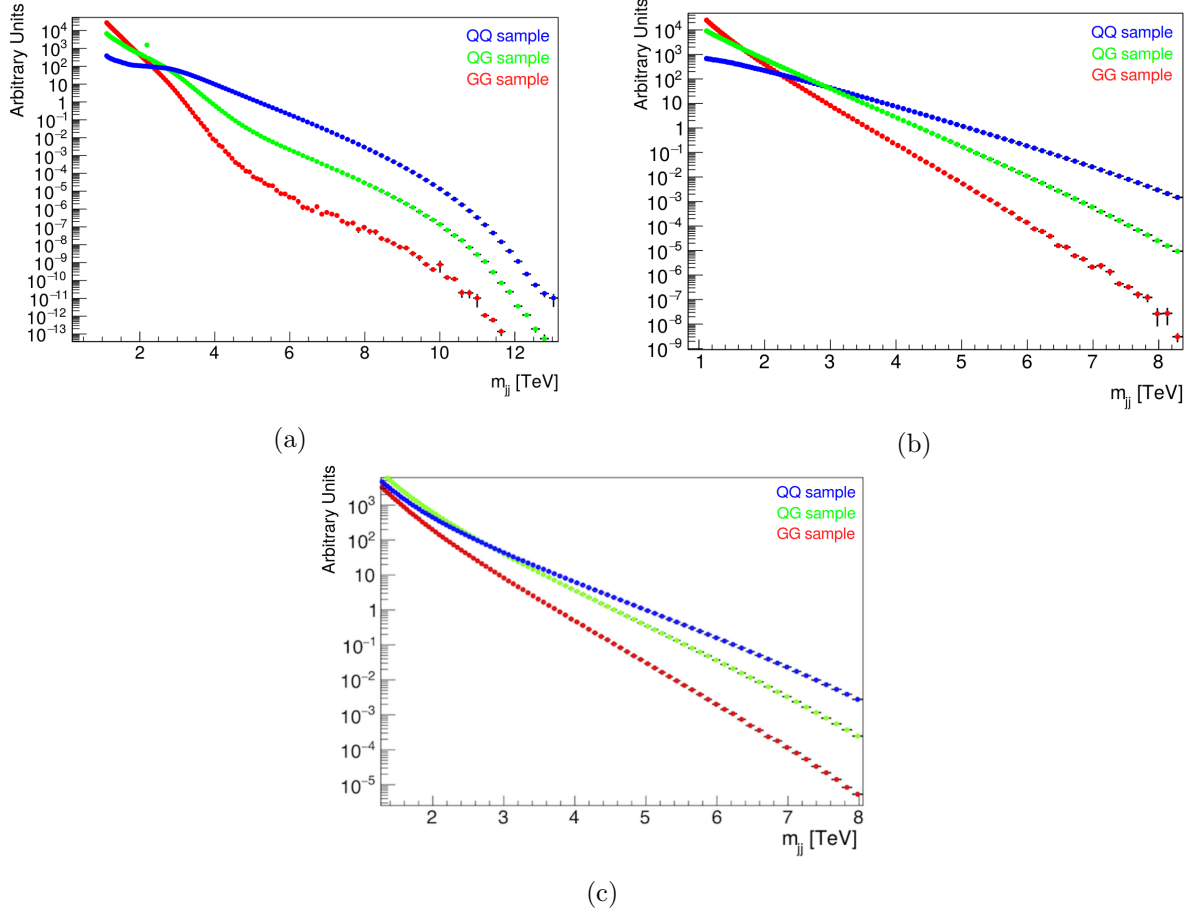


Figure 6.2: Simulated dijet samples produced using the Pythia 8 generator [20] using the A14 tune, the NNPDF2.3 PDF set, and processes with a full simulation of the ATLAS detector. The simulated events are separated into QQ (blue), QG (green) and GG (red) samples based on (a) Eq. 6.2, (b) Eq. 6.3 with  $k = 0.02$ ,  $c = 1$  and (c) Eq. 6.3 with  $k = 0.01$ ,  $c = 15$

Simulated background events are separated into subsamples using the selection criteria given in Eqs. 6.2-6.5. Fig. 6.2 shows the subsamples obtained with example values of  $k$  and  $c$ , with  $n_q = n_g$ . It is clear that the selection using Eq. 6.2 produces a more complex background shape than those using the simpler linear cut. This presents challenges when fitting the background, and is likely to introduce larger systematic uncertainties.

The tagging of the Excited Quark sample used in this analysis uses a tight and a loose selection, both based on Equation 6.3 with  $k = 0.07$ ,  $c = 10.165$  for the  $n_q$  cut, and  $k = 0.0063$ ,  $c = 15.156$  for the  $n_g$  cut. These will be referred to as  $Sel_{\text{Tight}}^{QG}$  and  $Sel_{\text{Loose}}^{QG}$ .

Figure 6.3 shows the loose selection applied to the mass distribution of a 4.5 TeV Excited Quark. The QG sample is increased relative to the QQ and GG samples. The QQ sample is especially suppressed with this selection. The shapes of the QG and GG samples are similar, with the QG sample being more peaked.

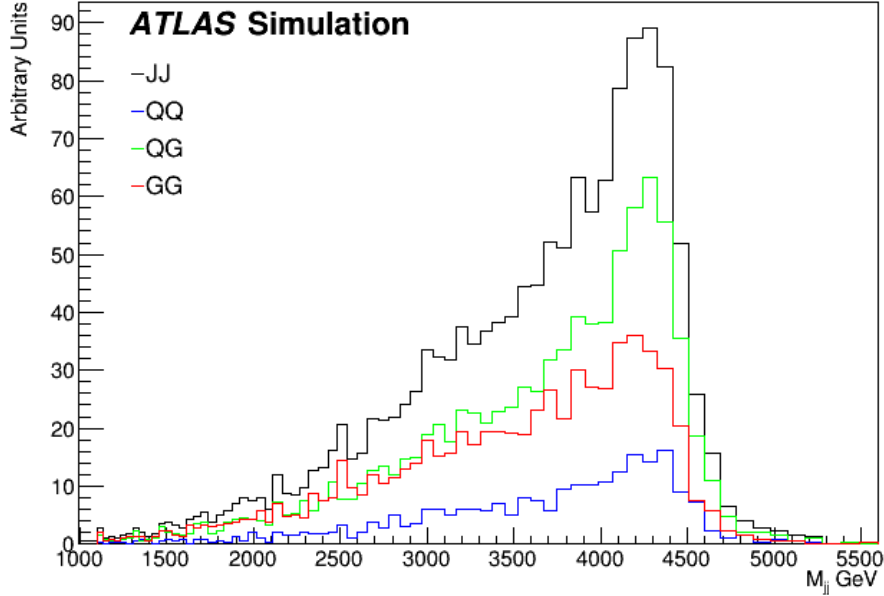


Figure 6.3: Simulated 4.5 TeV Excited Quark sample separated into untagged Jet-Jet (black), QQ (blue), QG (green) and GG (red) sub-samples,  $Sel_{\text{Loose}}^{QG}$  selection. Note that due to the loose selection including some events in multiple selections (see Eq. 6.6), the untagged sample is not equivalent to the sum of the sub-samples.

The ability of a tagger to discriminate between signal and background QCD events is driven by the differences in the track multiplicity distributions of both quark- and gluon-initiated jets. Figures 6.4, 6.5 and 6.6 show these distributions for background QCD events generated with PYTHIA in various  $p_T$  ranges. Figures 6.7 and 6.8 show the same distributions for an excited quark signal using the same event generator. Both sets of plots show the same trend illustrated in Figure 6.1, with the separation between mean track multiplicity for quark- and gluon-initiated jets increasing at higher  $p_T$ . What is also evident, is the decline in the proportion of gluon-initiated jets at high  $p_T$  in the QCD sample. This is not observed in the

excited quark sample, due to the decay process leading to the same quark-gluon final state at every simulated mass. At high  $p_T$ , one therefore observes a higher proportion of gluon jets in the signal than in the background, suggesting the power of quark-gluon tagging especially for gluon-initiated jet heavy final state processes at high mass.

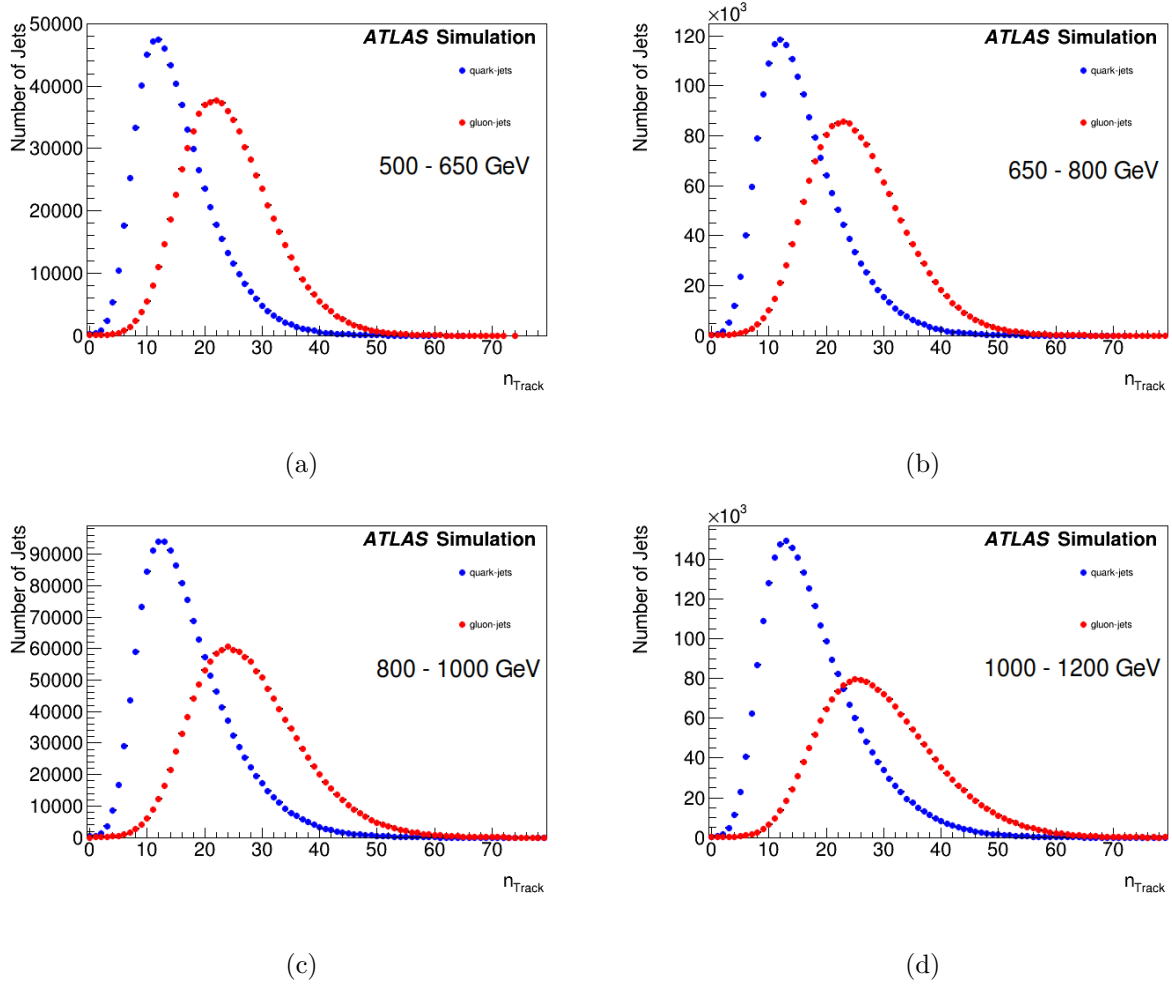
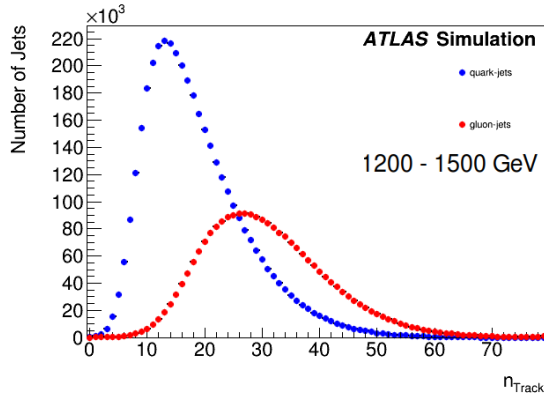
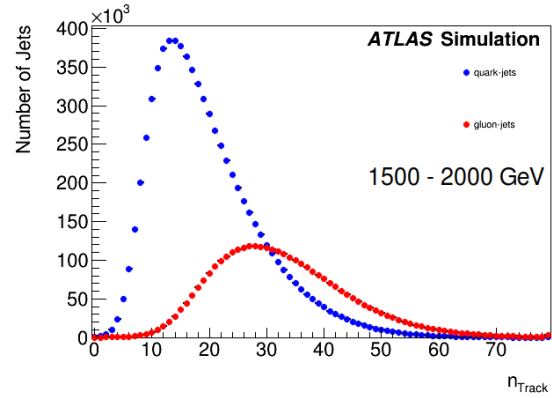


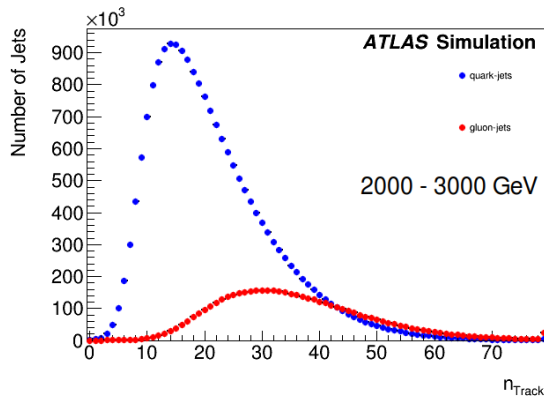
Figure 6.4: Truth  $n_{\text{Track}}$  distributions from the QCD PYTHIA8 MC samples used in this analysis between 500 and 1200 GeV. Quark jets (blue) have fewer tracks than gluon jets (red). The separation increases at higher  $p_T$ . Quark jets dominate at high  $p_T$ .



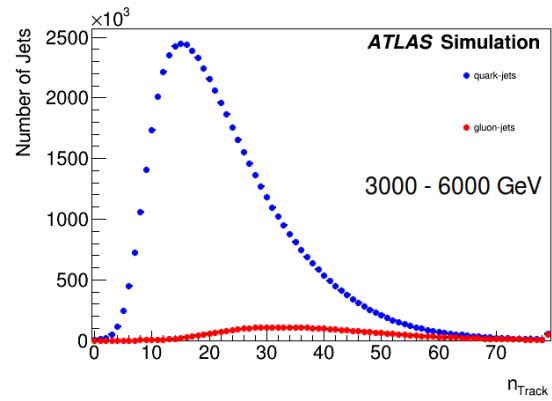
(a)



(b)



(c)



(d)

Figure 6.5: Truth  $n_{\text{Track}}$  distributions from the QCD PYTHIA8 MC samples used in this analysis between 1200 and 6000 GeV. Quark jets (blue) have fewer tracks than gluon jets (red). The separation increases at higher  $p_T$ . Quark jets dominate at high  $p_T$ .

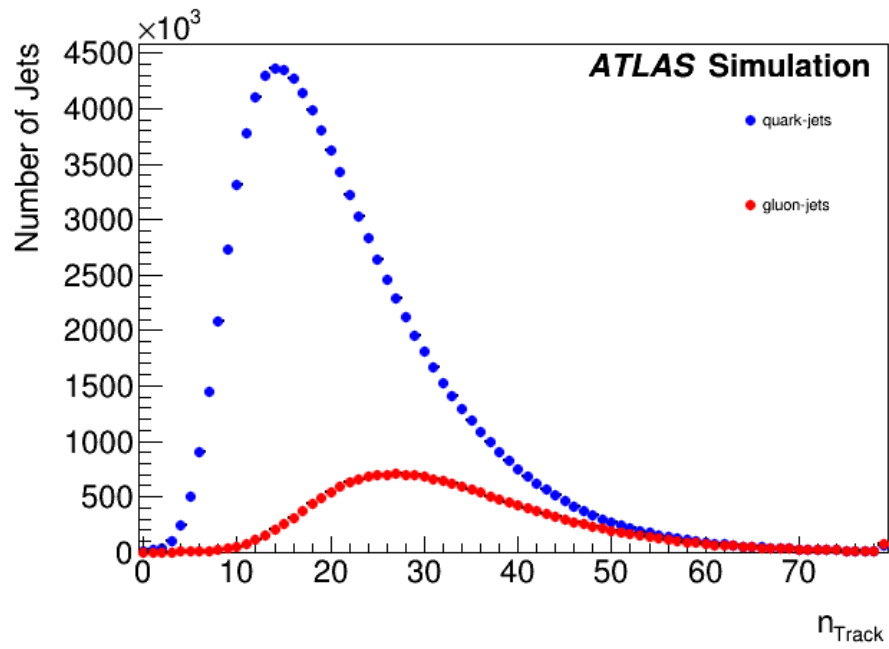


Figure 6.6: Truth  $n_{\text{Track}}$  distributions from the QCD PYTHIA8 MC samples used in this analysis over all  $p_T$  bins

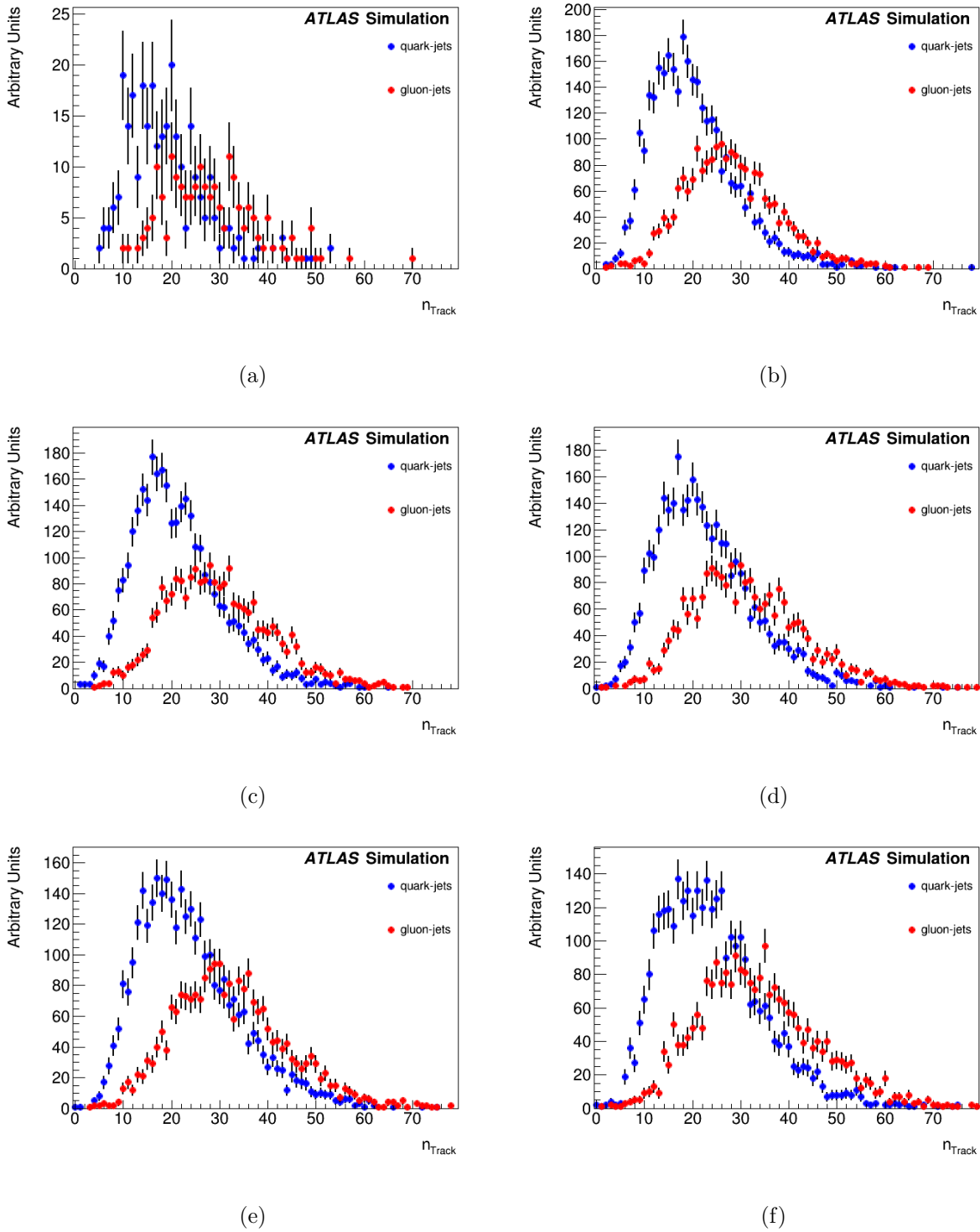
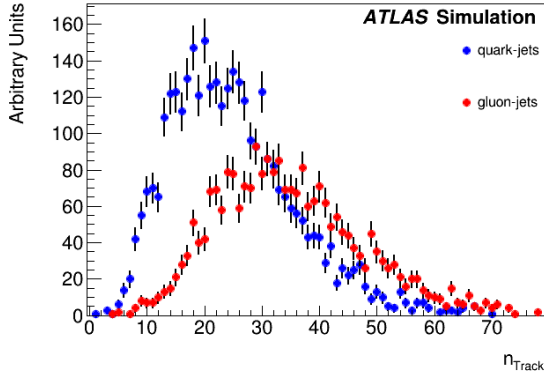
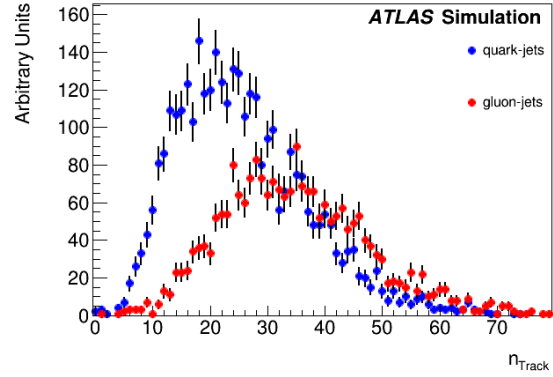


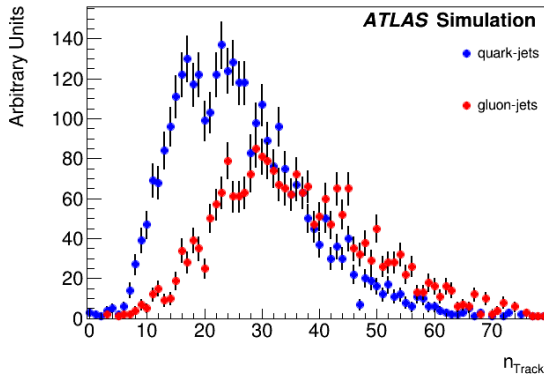
Figure 6.7: Truth  $n_{\text{Track}}$  distributions from the excited quark PYTHIA8 MC samples used in this analysis, 1000-4000 GeV. Unlike the QCD samples, at high  $p_T$  there is an equal number of quark and gluon jets.



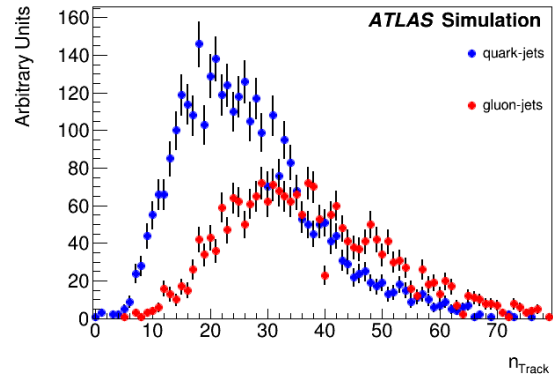
(a)



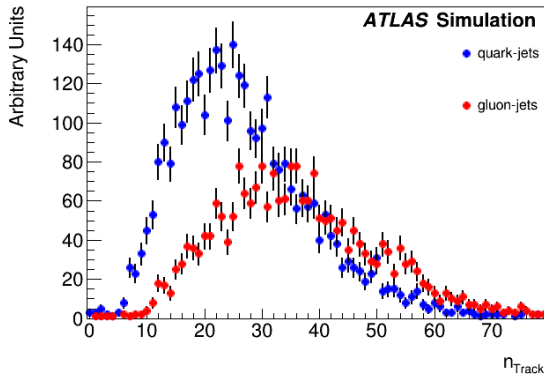
(b)



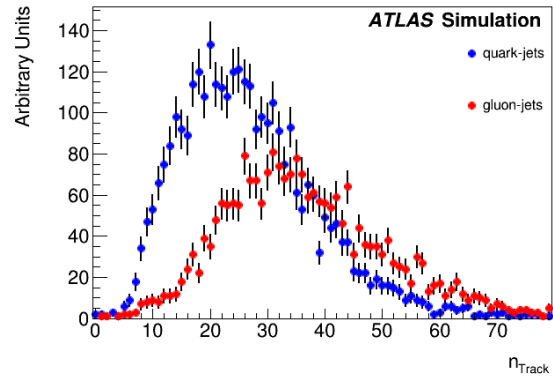
(c)



(d)



(e)



(f)

Figure 6.8: Truth  $n_{\text{Track}}$  distributions from the excited quark PYTHIA8 MC samples used in this analysis, 4500-7000 GeV. Unlike the QCD samples, at high  $p_T$  there is an equal number of quark and gluon jets.

### Optimising the Q-G sample selection

To optimise the quark-gluon sample selection for the resonance search it is helpful to determine the expected significance for the different resonant models. The significance is based on the composition of the  $q^*$  and  $H'$  signal models, and the background MC samples, and the expected selection efficiencies.

Consider first the simpler case of a gg final state, produced in the  $H'$  model. The inputs for the significance calculation are the efficiency of the truth quark and gluon jets being selected by the QG tagging,  $\epsilon_{q\mathbf{Q}}, \epsilon_{g\mathbf{Q}}$  ( $\epsilon_{q\mathbf{G}}, \epsilon_{g\mathbf{G}}$ ).

For example, for a given  $\mathbf{Q}$ -selection that results in a constant efficiency of  $\epsilon_{q\mathbf{Q}} = 0.8$  for truth quark jets, the corresponding efficiency for truth gluon jets to pass the selection is  $\epsilon_{g\mathbf{Q}} = 0.37$ . Further selections are given in Table 6.1.

Table 6.1: The efficiency for truth quark or gluon jets being selected by the  $\mathbf{Q}$  ( $\mathbf{G}$ ) selection  $\epsilon_{q\mathbf{Q}}, \epsilon_{g\mathbf{Q}}$  ( $\epsilon_{q\mathbf{G}}, \epsilon_{g\mathbf{G}}$ ).

$\epsilon_{q\mathbf{Q}}$	$\epsilon_{g\mathbf{Q}}$	$\epsilon_{q\mathbf{G}}$	$\epsilon_{g\mathbf{G}}$
0.9	0.6	0.9	0.47
0.8	0.37	0.8	0.34
0.7	0.24	0.7	0.25
0.6	0.15	0.6	0.19
0.5	0.09	0.5	0.13
0.4	0.05	0.4	0.09
0.3	0.03	0.3	0.06

The expected significance for a GG signal selection for the  $H'$  model and the QCD background is given by

$$S_{H'} = N_S \sum_i \frac{f_{qq_i} \epsilon_{q\mathbf{G}}^2 + f_{qg_i} \epsilon_{q\mathbf{G}} \epsilon_{g\mathbf{G}} + f_{gg_i} \epsilon_{g\mathbf{G}}^2}{\sqrt{B_{qq_i} \epsilon_{q\mathbf{G}}^2 + B_{qg_i} \epsilon_{q\mathbf{G}} \epsilon_{g\mathbf{G}} + B_{gg_i} \epsilon_{g\mathbf{G}}^2}} \quad (6.7)$$

where  $N_S$  is the expected number of signal events,  $f_{xx_i}$  is the fraction of signal events which produce  $qq$ ,  $qg$  and  $gg$  jet events in mass bin  $i$  (for an  $H'$  signal this is mostly  $gg$  events), and  $B_{xx_i}$  is the number of background events which produce  $qq$ ,  $qg$  and  $gg$  jet events in mass bin  $i$  where the total number of events is normalised to the size of the data set collected

in the 2015 and 2016 data taking periods. The resulting significance is compared to the expected significance of applying no gluon selection to the data for  $H'$  masses of 2.0 to 7.0 TeV in 0.5 TeV steps. The results of the calculation are shown in Fig. 6.9 and show that an improvement in the significance of up to 40% is possible at high masses for selection efficiencies of  $\epsilon_{g\mathbf{G}}$  of 0.9 and 0.8 (i.e. a minimal selection criteria).

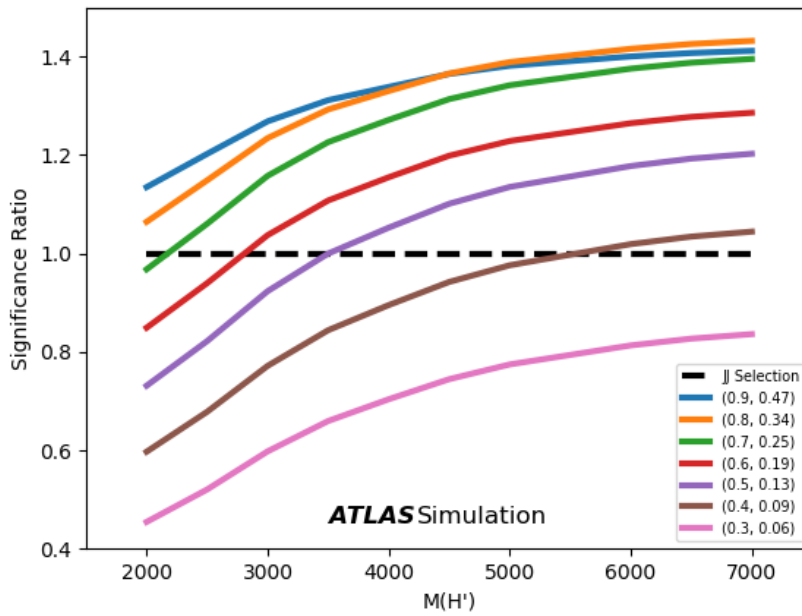


Figure 6.9: The expected significance for a  $H'$  for values of  $\epsilon_{g\mathbf{G}}$  from 0.9 to 0.3 compared to the significance with no selection applied.

Calculating the significance for QG signal selection is more complicated as the upper threshold on selection of a quark-jet is greater than the lower threshold of the selection of a gluon-jet. This means it is possible to tag a jet as both a quark- and a gluon-jet simultaneously. This complicates the calculation of the significance by introducing an additional category of jets. For this type of signal, the samples will be categorised as **Qonly**, **Q&G**, and **Gonly** with corresponding efficiencies of  $\epsilon_{q\mathbf{Qonly}}$ ,  $\epsilon_{q\mathbf{Q\&G}}$ , and  $\epsilon_{q\mathbf{Gonly}}$  with a similar notation for truth gluon-jets. We can then calculate the fraction of the  $qq$ ,  $qg$ , and  $gg$  truth samples that pass the selection as

$$\begin{aligned}\epsilon_{qq} &= 2\epsilon_{q\mathbf{Qonly}}\epsilon_{q\mathbf{Gonly}} + \epsilon_{q\mathbf{Q\&G}} (\epsilon_{q\mathbf{Qonly}} + \epsilon_{q\mathbf{Gonly}}) + \epsilon_{q\mathbf{Q\&G}}^2 \\ \epsilon_{qg} &= \epsilon_{q\mathbf{Qonly}} (\epsilon_{g\mathbf{Q\&G}} + \epsilon_{g\mathbf{Gonly}}) + \epsilon_{q\mathbf{Q\&G}} (\epsilon_{g\mathbf{Qonly}} + \epsilon_{g\mathbf{Q\&G}} + \epsilon_{g\mathbf{Gonly}}) \\ &\quad + \epsilon_{g\mathbf{Gonly}} (\epsilon_{q\mathbf{Q\&G}} + \epsilon_{q\mathbf{Qonly}}) \\ \epsilon_{gg} &= 2\epsilon_{g\mathbf{Qonly}}\epsilon_{g\mathbf{Gonly}} + \epsilon_{g\mathbf{Q\&G}} (\epsilon_{g\mathbf{Qonly}} + \epsilon_{g\mathbf{Gonly}}) + \epsilon_{g\mathbf{Q\&G}}^2\end{aligned}$$

which gives an overall significance of

$$S_{q^*} = N_S \sum_i \frac{f_{qq_i}\epsilon_{qq} + f_{qg_i}\epsilon_{qg} + f_{gg_i}\epsilon_{gg}}{\sqrt{B_{qq_i}\epsilon_{qq} + B_{qg_i}\epsilon_{qg} + B_{gg_i}\epsilon_{gg}}}. \quad (6.8)$$

Table 6.2: The efficiency for truth quark or gluon jets being selected by the **Q** (**G**) selection  $\epsilon_{q\mathbf{Q}}$ ,  $\epsilon_{g\mathbf{Q}}$  ( $\epsilon_{q\mathbf{G}}$ ,  $\epsilon_{g\mathbf{G}}$ ).

$\epsilon_{q\mathbf{Qonly}}$	$\epsilon_{q\mathbf{Q\&G}}$	$\epsilon_{q\mathbf{Gonly}}$	$\epsilon_{g\mathbf{Qonly}}$	$\epsilon_{g\mathbf{Q\&G}}$	$\epsilon_{g\mathbf{Gonly}}$
0.52	0.39	0.1	0.1	0.51	0.39
0.66	0.14	0.2	0.2	0.19	0.61
0.7	0.0	0.26	0.24	0.0	0.7
0.6	0.0	0.19	0.15	0.0	0.6
0.5	0.0	0.14	0.09	0.0	0.5
0.4	0.0	0.1	0.05	0.0	0.4
0.29	0.0	0.07	0.02	0.0	0.3

The expected significance for a QG signal selection for the  $q^*$  model and the QCD background is determined using the same method for  $q^*$  masses of 2.0 to 7.0 TeV in 0.5 TeV steps. The results of the calculation are shown in Fig. 6.10 and show no improvement in the significance if the efficiency of quark and gluon selection is equal ( $\epsilon_{q\mathbf{Q}} = \epsilon_{q\mathbf{Q}\text{only}} + \epsilon_{q\mathbf{Q}\&\mathbf{G}} = \epsilon_{g\mathbf{G}} = \epsilon_{g\mathbf{G}\text{only}} + \epsilon_{g\mathbf{Q}\&\mathbf{G}}$ ).

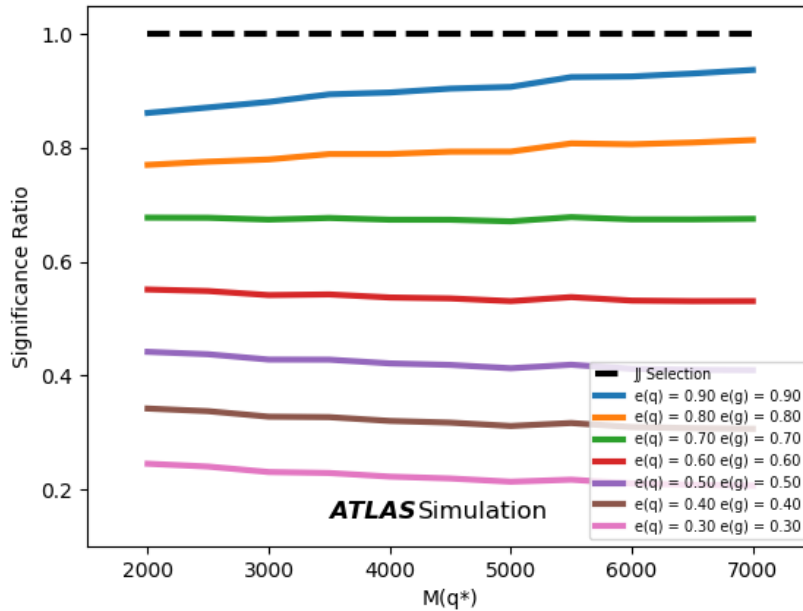


Figure 6.10: The expected significance for a  $q^*$  compared to the significance with no selection applied.

We can also choose different efficiencies for quark and gluon selection for the QG selection. If we do this we find the best improvement in significance if we apply no selection criteria on the gluon jet and tight selection on the quark jet (i.e. we require one jet to pass the quark selection criteria), as seen in Figure 6.11. Here we see improvements of up to 15% in significance for high mass  $q^*$  samples.

An assumption underlying the above significance calculations should be noted, namely that the efficiency of selecting the quark- and gluon-jets is the same in both the signal sample and QCD sample. This depends on the signal model under investigation having the same

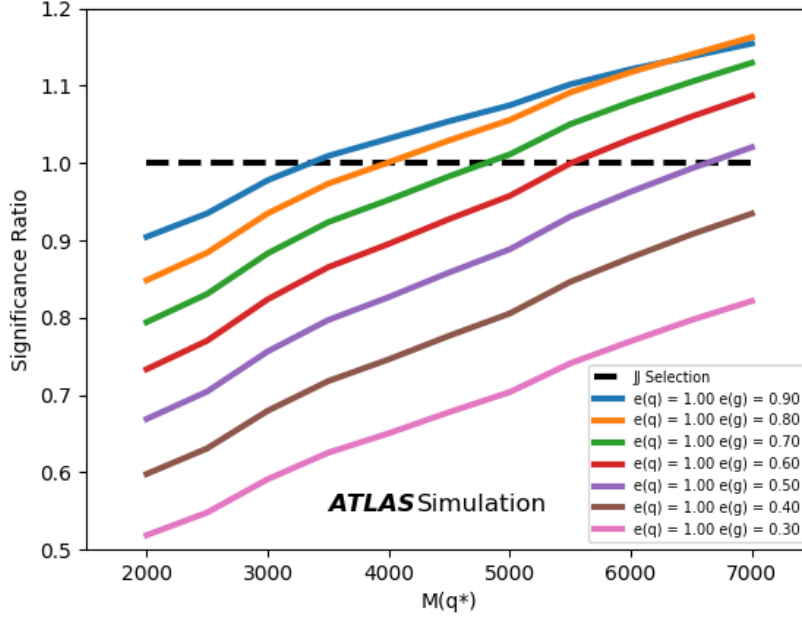


Figure 6.11: The expected significance for a  $q^*$  compared to the significance with no selection applied where no selection is required on the gluon jet.

$n_{\text{track}}$  distribution for both the quark- and gluon-jets. Normalised distributions of the  $n_{\text{track}}$  distributions of the truth jets in the QCD and signal samples are shown in figs. 6.12 to 6.14. The gluon-jets appear to be well matched between the signal samples and QCD, while the quark-jets appear to have higher track multiplicity in the  $q^*$  sample. The reason for this is not clear, however may be due to differences in the colour flow between QCD hard scatter events and events with an intermediate excited quark.

The effect of this apparent mismodelling is to reduce the efficiency of the quark-jet selection of the signal sample compared to QCD, thus the above assumptions regarding the obtained signal significance do not hold.

The reason for this mismodelling was traced to the treatment of colour dipoles arising in the  $q^* \rightarrow qg$  decay. A more thorough treatment of such dipoles is included in PYTHIA since version 8.301, which incorporates a new coherent Vincia RF shower model [103], which was

not available in time for this analysis.

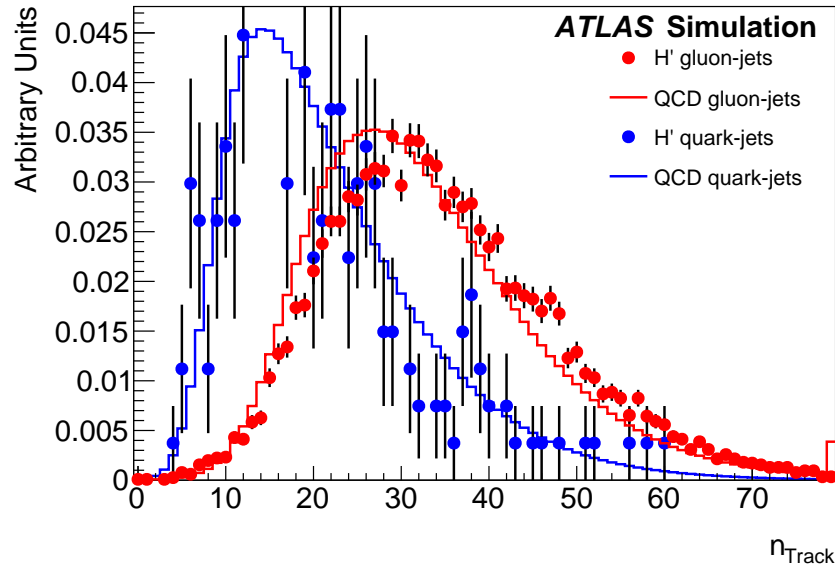


Figure 6.12: The  $n_{\text{track}}$  distribution of truth Quark jets (blue) and truth Gluon jets (red) for QCD (solid line) compared to a 5 TeV  $H'$  signal (solid markers).

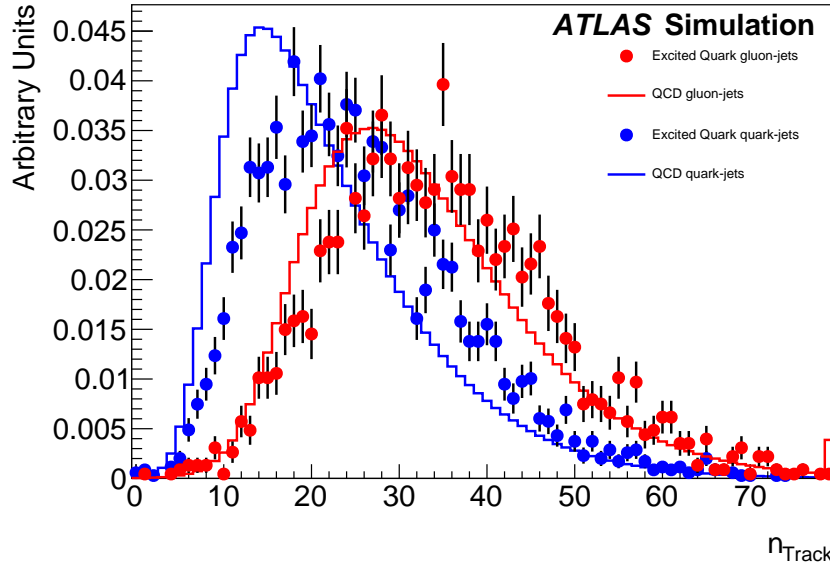


Figure 6.13: The  $n_{\text{track}}$  distribution of truth Quark jets (blue) and truth Gluon jets (red) for QCD (solid line) compared to a 5 TeV  $q^*$  signal (solid markers).

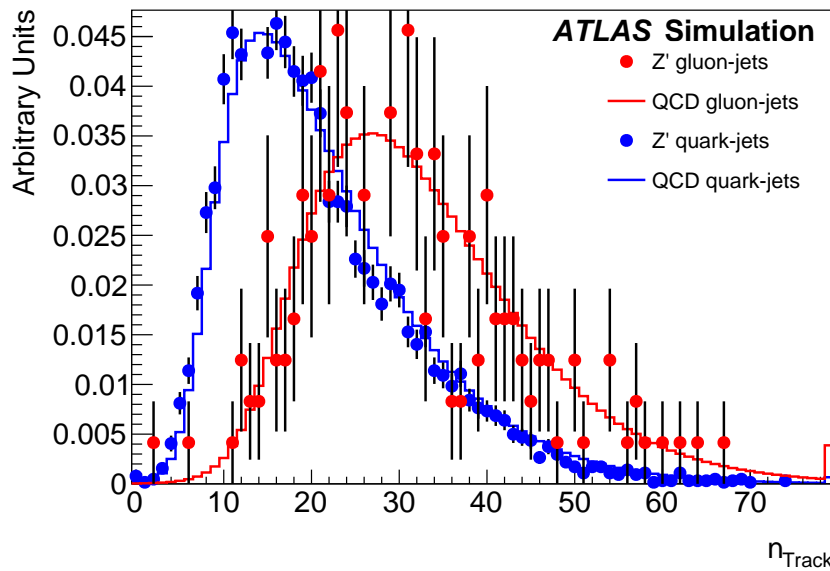


Figure 6.14: The  $n_{\text{track}}$  distribution of truth Quark jets (blue) and truth Gluon jets (red) for QCD (solid line) compared to a 5 TeV  $Z'$  signal (solid markers).

## 6.2 Systematic Uncertainties

Systematic uncertainties relating specifically to the identification of quark- and gluon-initiated jets come from both modelling uncertainties, and from detector-level track reconstruction uncertainties. These have both been studied at low  $p_T$  ( $< \sim 1200$  GeV) [4], whilst studies are currently ongoing to extend this derivation into the high- $p_T$  regime.

### Modelling Uncertainties

Considering only the two highest  $p_T$  jets in a MC simulated dijet event, one can define the fraction labelled as a quark or gluon jet by  $f_{q,g}^{f,c}$ , where  $f(c)$  denotes the more forward (central) jet of the two. The fractions  $f_{q,g}^{f,c}$  depend on parton distribution functions (PDFs) convolved with matrix element calculations. The differences in the fractions of forward and central gluon jets approaches zero at high and low  $p_T$ , and reaches a peak at  $p_T \sim 400$  GeV (see Figure 6.15 (a)). The difference in average charged particle multiplicity,  $\langle n_{charged} \rangle$  can be described separately for quarks and gluons in each  $p_T$  bin:

$$\begin{aligned}\langle n_{charged}^f \rangle &= f_q^f \langle n_{charged}^q \rangle + f_g^f \langle n_{charged}^g \rangle \\ \langle n_{charged}^c \rangle &= f_q^c \langle n_{charged}^q \rangle + f_g^c \langle n_{charged}^g \rangle\end{aligned}\tag{6.9}$$

If the  $\langle n_{charged} \rangle$  distribution in jets is independent of  $\eta$ , then equation 6.9 can be used to extract the average number of charged particles in quark- and gluon-initiated jets. The validity of this assumption is demonstrated in Figure 6.16 for PYTHIA MC simulation, similar closure is observed in HERWIG++ [4]. Figure 6.16 compares the values of  $\langle n_{charged} \rangle$  obtained from Eq. 6.9 and directly from MC Truth, finding agreement better than 1% across nearly the entire  $p_T$  range. The distributions of forward and central jets are coincident for both quark- and gluon-initiated jets, and also agree with the predictions extracted from Eq. 6.9. Figure 6.16 thus demonstrates the charged particle multiplicity of jets depends to good approximation only on the  $p_T$  and type (quark or gluon) of the initiating parton.

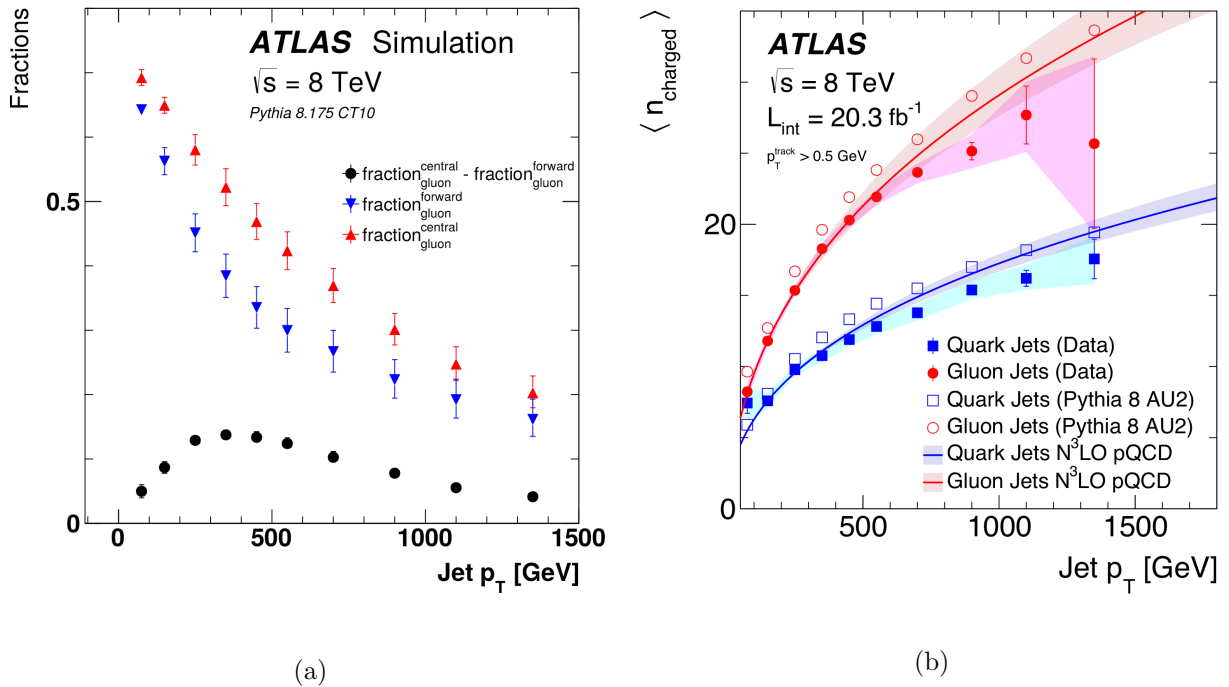


Figure 6.15: (a) The simulated fraction of jets originating from gluons as a function of jet  $p_T$  for the more forward jet (down triangle), the more central jet (up triangle), and the difference between these two fractions (circle). The error bars represent PDF and ME uncertainties. (b) The jet  $p_T$  dependence of the average charged-particle multiplicity of quark- and gluon-initiated jets. The error bands include the experimental uncertainties, as well as PDF and ME uncertainties. The MC statistical uncertainties are smaller than the markers. The uncertainty band for the N<sup>3</sup>LO pQCD prediction is determined by varying the scale  $\mu$  by a factor of two up and down. Both (a) and (b) use PYTHIA with the CT10 PDF. From Ref [5]

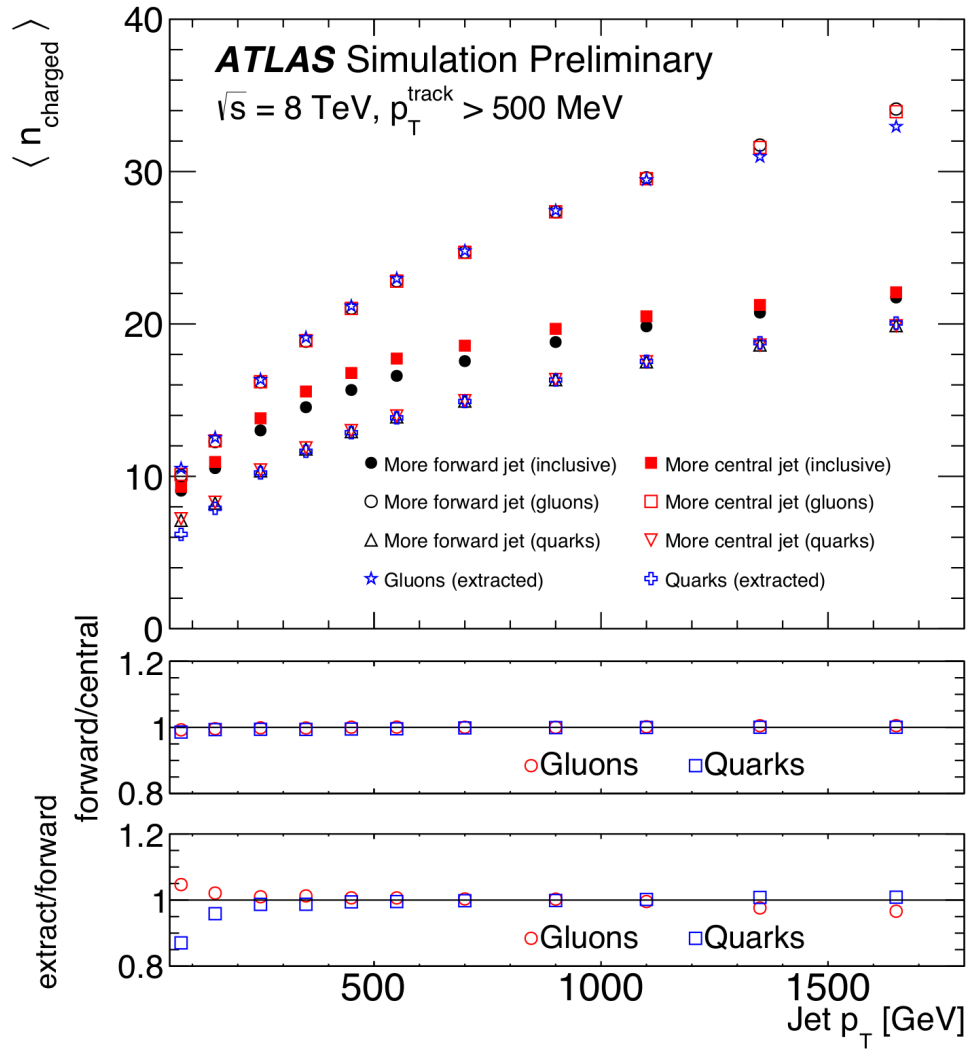


Figure 6.16: An illustration of the closure test from the central-forward method for jets with  $p_T > 50$  GeV. The upper panel shows the values of  $\langle n_{charged}^f \rangle$  and  $\langle n_{charged}^c \rangle$  as the filled black circles and red squares respectively. The open blue points show the values of  $\langle n_{charged}^{q,g} \rangle$  extracted from Eq. 6.9 while the open red and black points show  $\langle n_{charged}^{q,g} \rangle$  for the more forward and more central jets extracted from labels directly in simulation. The middle panel shows the ratio of  $\langle n_{charged}^{q,g} \rangle$  for the forward versus central jets and the lower panel shows the ratio for the values extracted from Eq. 6.9 and the ones taken directly from simulation for the more forward jets. From Ref. [4].

Tagging uncertainties may be calibrated using the approach of Ref. [5] to provide a measure of  $\langle n_{charged} \rangle$  as a function of  $p_T$ , and extracting  $\langle n_{charged}^{q,g} \rangle$  by exploiting the rapidity dependence of the quark-gluon jet fraction. When applied to the unfolded data, this procedure results

in the distribution shown in Figure 6.15 (b). In this particular study, the nominal  $f_{q,g}^{f,c}$  fractions are calculated from PYTHIA 8 [104] using the CT10 [105] PDF set. Two sources of uncertainty in addition to experimental and statistical are included in Figure 6.15 (b). Eigenvector variations in the CT10 PDF set are used to estimate the PDF uncertainty, while the uncertainty in the quark-gluon fraction due to the matrix element calculation is taken as the variation between PYTHIA and HERWIG++ [106]. The PYTHIA 8 results are reweighted to the PDF set in HERWIG++, CTEQ6L1 [107], using the LHAPDF [108] library. Uncertainty bands are formed by the summation in quadrature of all of these uncertainties. The impact of these uncertainties is shown in Figure 6.17 for a working point of 60% quark jet efficiency (in each  $p_T$  bin, the  $n_{\text{track}}$  cut is defined by requiring the efficiency closest to 60%).

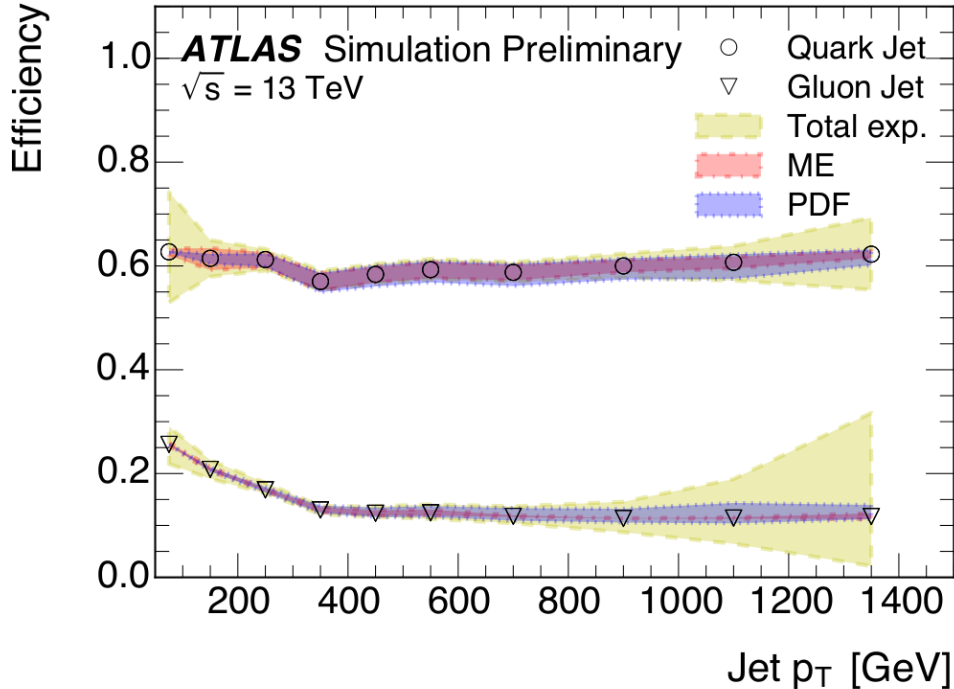


Figure 6.17: The systematic uncertainties on the particle-level charged particle distribution for a 60% quark jet efficiency working point. From Ref [4].

Additional variations were studied [4] to ensure the calculated uncertainties are reasonable.

The PYTHIA 8 sample was re-weighted to the central NNPDF 2.3 set to check if these two unrelated PDF sets produce a similar uncertainty to the CT10 variations. The uncertainties ranged between  $\sim 0.1$  to 1 charged particles at low and high  $p_T$  in both cases, showing good agreement. Additional negligible uncertainties are discussed in Ref. [4].

This analysis uses the A14 tune, which is found to be in good agreement with data for the charged track multiplicity found inside of jets up to  $p_T \sim 1600$  GeV. Figure 6.18 shows a comparison between data, the A14 tune and another popular tune used in Higgs analyses, the AZNLO tune [109], which overestimates the multiplicity. The factorised approach presented in Ref. [4] allows the same procedure to be used for any tune.

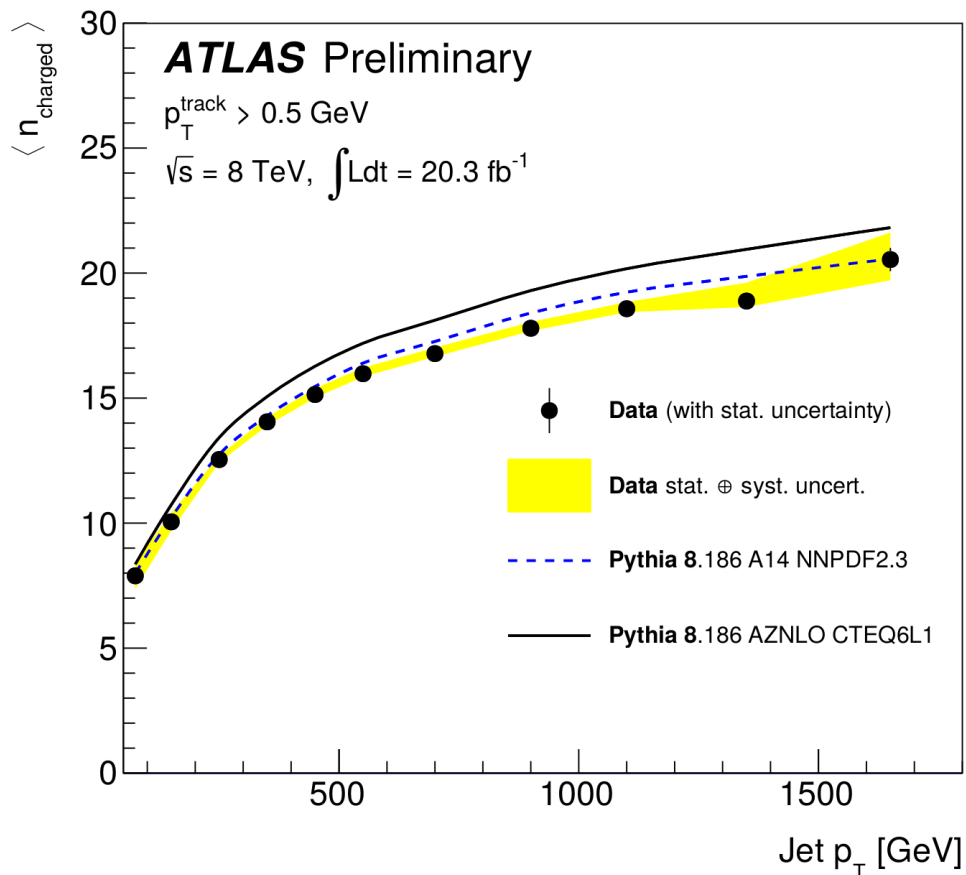


Figure 6.18: A comparison of the particle-level charged particle multiplicity for the more forward jet from data and PYTHIA 8 with the A14 and AZNLO tunes from Ref. [4]. The data and uncertainties are from Ref. [5] via HEPData [6].

Another consideration in assessing modelling uncertainties is the topological dependence of the tagging procedure. This is unavoidable, since quarks and gluons carry colour charge, while the hadrons in jets do not. It has been found in previous studies [110] that this topology dependence is small when tagging based on  $n_{\text{track}}$ .

### Experimental Uncertainties

The uncertainties presented above are detector independent, relying on the modelling of the charged-particle constituents of the jets. Additional detector-specific uncertainties must be considered when relating the charged-particle multiplicity to the observed track multiplicity. Three categories of experimental uncertainty are considered: reconstruction efficiency, fake rate, track fit parameter bias (scale) and resolution.

The reconstruction efficiency uncertainty comes from the imperfect description of the ID material in simulation and from lost tracks in volumes with high particle density. The uncertainty arising from the modelling of particle interactions with the ID material is measured by varying the GEANT4 physics list [111]. The fraction of lost tracks in the core of jets where ID clusters can merge is measured by considering one-track clusters in the core of jets which have a deposited charge consistent with two minimum ionising particles [112].

Fake tracks are particle trajectories which cannot be (mostly) associated to a single charged particle. The rate at which these fake tracks appear increases with pile-up due to the higher hit rate in the ID. The fake rate has been measured for various track selections [111] and can be mitigated with various quality criteria.

Track fit parameter scale and resolution uncertainties are mostly negligible for track counting. A small uncertainty on track  $p_T$  exists from a potential sagitta bias<sup>1</sup> from weak modes<sup>2</sup> [111].

---

<sup>1</sup>Sagitta deformations are movements of the detector orthogonal to the track trajectory, and affect the reconstructed track curvature oppositely for positively and negatively charged particles [113].

<sup>2</sup>The ID is aligned using a track-based technique [114, 115]. This approach is confronted with some modes to which the fitted tracks have limited sensitivity. These weak modes of alignment are detector deformations that preserve a helical trajectory of the tracks and hence do not affect the  $\chi^2$  of the track fit. Such weak modes are the principal source of systematic effects related to the alignment procedure.

The impact of these experimental uncertainties on quark-gluon tagging efficiency are summarised in Figure 6.19 for a 60% quark jet efficiency working point. Fake and poorly measured tracks are rejected with a set of quality criteria and  $p_T > 0.5$  GeV [111].

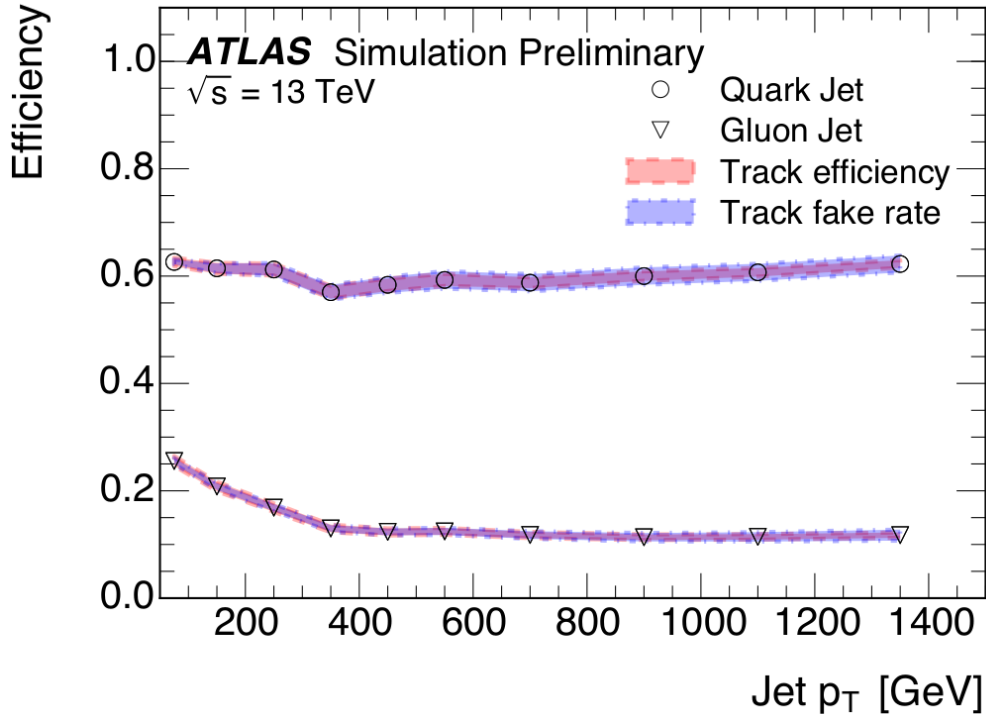


Figure 6.19: Experimental systematic uncertainties on the track reconstruction for the 60% quark jet efficiency working point of the quark-gluon tagger. From Ref. [4]

Considering the modelling and experimental uncertainties as uncorrelated, and summing in quadrature provides the total systematic uncertainty. This is shown in Figure 6.20 for the illustrative 60% quark jet efficiency working point.

### Uncertainties at High $p_T$

Uncertainties are highest at low and high  $p_T$ . At low  $p_T$ , the minimum jet  $p_T$  cut requirement limits the impact of the systematic uncertainties on the analysis. At high  $p_T$ , the statistics available from data is limited, especially in the case of gluon-initiated jets which are typically lower in  $p_T$  than quark-initiated jets. The use of equations 6.9 requires different fractions of

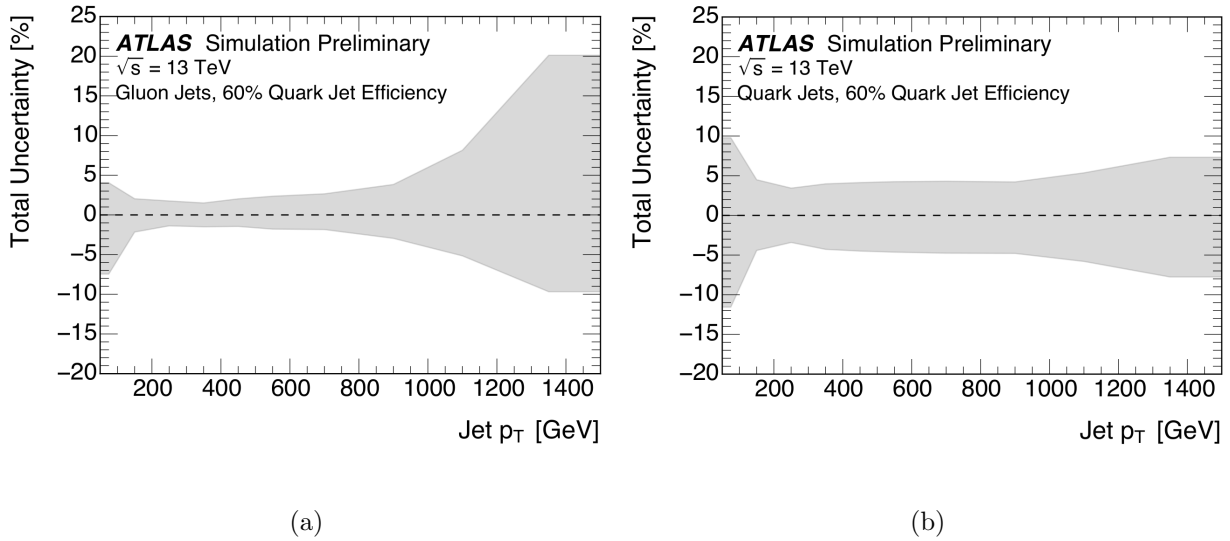


Figure 6.20: The total systematic uncertainty for the 60% quark jet efficiency working point for the quark-gluon tagger for (a) gluon jets and (b) quark jets. From Ref. [4]

quark- and gluon- initiated jets in the forward and central regions, thus the lack of gluon-initiated jets at high  $p_T$  becomes a limiting factor.

Uncertainties can also be extracted using only simulation, considering the variations in hadronisation models in the various event generators, see for example Section 2.3. Comparisons of the distributions of track multiplicity versus jet  $p_T$  between different event generators are currently being made to investigate these variations and define systematic uncertainties beyond the current  $p_T$  range.

# Chapter 7

## Limit Setting

### 7.1 Limit Setting

To quantify the effect of quark-gluon tagging on the dijet search, interaction cross section limits must be produced for the simulated signal models. A frequentist method is used to perform hypothesis tests and the profile likelihood ratio is used as test statistic.

The test statistic,  $q_{\mu_{sig}}$

$$q_{\mu_{sig}} = -2\ln\lambda(\mu_{sig}) \quad (7.1)$$

where  $\lambda(\mu)$  is the profile likelihood ratio, with nuisance parameters  $\boldsymbol{\theta}$ :

$$\lambda(\mu_{sig}) = \frac{L(\mu_{sig}, \hat{\boldsymbol{\theta}})}{L(\hat{\mu}_{sig}, \hat{\boldsymbol{\theta}})} \quad (7.2)$$

$\hat{\mu}_{sig}$  and  $\hat{\boldsymbol{\theta}}$  maximise the likelihood function, and  $\hat{\boldsymbol{\theta}}$  maximises the likelihood for a specific, fixed value of the signal strength  $\mu_{sig}$  i.e., is the conditional maximum-likelihood (ML) estimator of  $\boldsymbol{\theta}$ .

The likelihood function is the product of Poisson probabilities over all of the bins,

$$L(\mu_{sig}, \boldsymbol{\theta}) = \prod_{i=1}^N \frac{(\mu_{sig} s_i + b_i)^{n_i}}{n_i!} e^{-(\mu_{sig} s_i + b_i)} \quad (7.3)$$

To test the exclusion of BSM physics models, the  $CL_s$  method [116, 117] is employed. Approximations using asymptotic formulae are used in order to speed up the evaluation process [118].

Prior Run I dijet analyses employed a Bayesian approach to limit setting, however since Run II, consolidation of the tools used in the analysis community has led to the adoption of frequentist methods. These were already more popular among ATLAS analyses and have several advantages: the calculations used tend to converge more quickly, and equations exist to predict the distributions of the posterior quantiles [118]. There are slightly different interpretations of the upper limits in the Bayesian vs Frequentist cases. A Bayesian reports an upper limit on the signal strength as the cross-section above which one is 95% certain that no new physics process occurs. A Frequentist upper limit is the upper edge of a 95% CL interval with a lower edge at  $-\infty$ .

The use of frequentist statistics removes an element of subjectivity introduced by the Bayesian prior probability distribution. frequentists suffer from the possible misinterpretation of results: one draws conclusions about the compatibility of the data with the theoretical model under consideration, whilst physicists tend to misinterpret the frequentist results as a statement about the theory given the data [117]. Both Bayesian credible intervals and frequentist confidence intervals tend to converge with large statistics and small backgrounds.

Feldman and Cousins [119] advocate an approach utilising frequentist confidence intervals, however the use of such intervals raises the possibility of apparently unintuitive results. A common example is that of two searches with identical efficiencies and observations, but

different backgrounds. Here, the lowest (strongest) limit is found by the experiment with the largest expected background.

A widely accepted solution to these problems is the  $CL_s$  method, used accross HEP experiments and intended to generalise Zech’s classical derivation [120] of upper limits for single channel counting experiments which corresponded to the Bayesian result with uniform prior. One normalises the confidence level observed for the signal plus background hypothesis,  $CL_{s+b}$  to that of the background-only hypothesis,  $CL_b$  (equivalent to  $\mu_{sig} = 0$ ). This makes possible sensible exclusion limits on the signal even when the observed number of events is sufficiently small to doubt the background hypothesis. This is sometimes referred to as a *modified frequentist* procedure.

This modified frequentist renormalisation is simply

$$CL_s \equiv \frac{CL_{s+b}}{CL_b} \quad (7.4)$$

$CL_s$  is stricky speaking a ratio of confidences, not a confidence itself. The signal hypothesis is nonetheless considered excluded at the confidence level CL when

$$1 - CL_s \leq CL \quad (7.5)$$

A result of  $CL_s$  not being a true confidence is that the hypothetical false exclusion rate is now lower than in the nominal rate (1 - CL). The difference between these rates increases as the p.d.f.’s of the signal plus background and background-only hypotheses become similar.  $CL_s$  is inherently conservative - this has the effect of reducing the range of model parameters for which an exclusion result is possible - increasing the “coverage” of the analysis.  $CL_s$  however also avoids the situation of having the experiment with larger background reporting the stronger limit in the case of two experiments with the same signal rate.

The  $CL_s$  method is executed using the HistFitter software framework [121]. The p-value is calculated using a distribution of the test statistic,  $f(q_{\mu_{sig}}|\mu_{sig}, \theta)$ , obtained by running multiple pseudo-experiments to randomise the number of observed events and the central values of the auxiliary measurements around which  $\theta$  can be varied.

An initial scan consisting of multiple hypothesis tests executed using the asymptotic calculator [118] is conducted to evaluate the  $CL_s$  values for a wide range of signal strength values. A second scan is then conducted on a refined interval using the expected upper limit obtained from the initial scan.

## 7.2 Results

The MC and data samples show similar agreement for the mass spectra in each of the sub-samples compared to the untagged spectrum, Figure 7.1. All  $m_{jj}$  distributions are smoothly falling, with no sudden shape changes for either data or MC, as seen in Figure 6.2a. The SWiFT background obtained from the untagged PYTHIA sample is shown in Figure 7.2. The instability of the kind seen in Figure 5.1, where the fit swings from overestimating to underestimating the events is not observed. Large variation between individual bins can be seen, due to the statistical variations in the generated MC itself. This illustrates the purpose of smoothing the MC, and shows that even with this procedure, the MC still exhibits such fluctuations. The effect of such fluctuations is most pronounced at low  $m_{jj}$ . Above 2 TeV, the fit is stable, and SWiFT produces a good fit to the simulated data. Results are therefore presented for masses above 2 TeV only.

95% limits found for each generated mass point of the excited quark signal are displayed in Figure 7.3. Selections used are  $Sel_{\text{Tight}}^{QG}$  and  $Sel_{\text{Loose}}^{QG}$ , as defined in Chapter 6. The plots are representative of efforts to improve the limits obtained with the untagged jet-jet samples, displayed with the solid black lines. Slight improvements can be seen at higher mass with the loose selection, Figure 7.3a, while no improvements are obtained with the tight selection, Figure 7.3b.

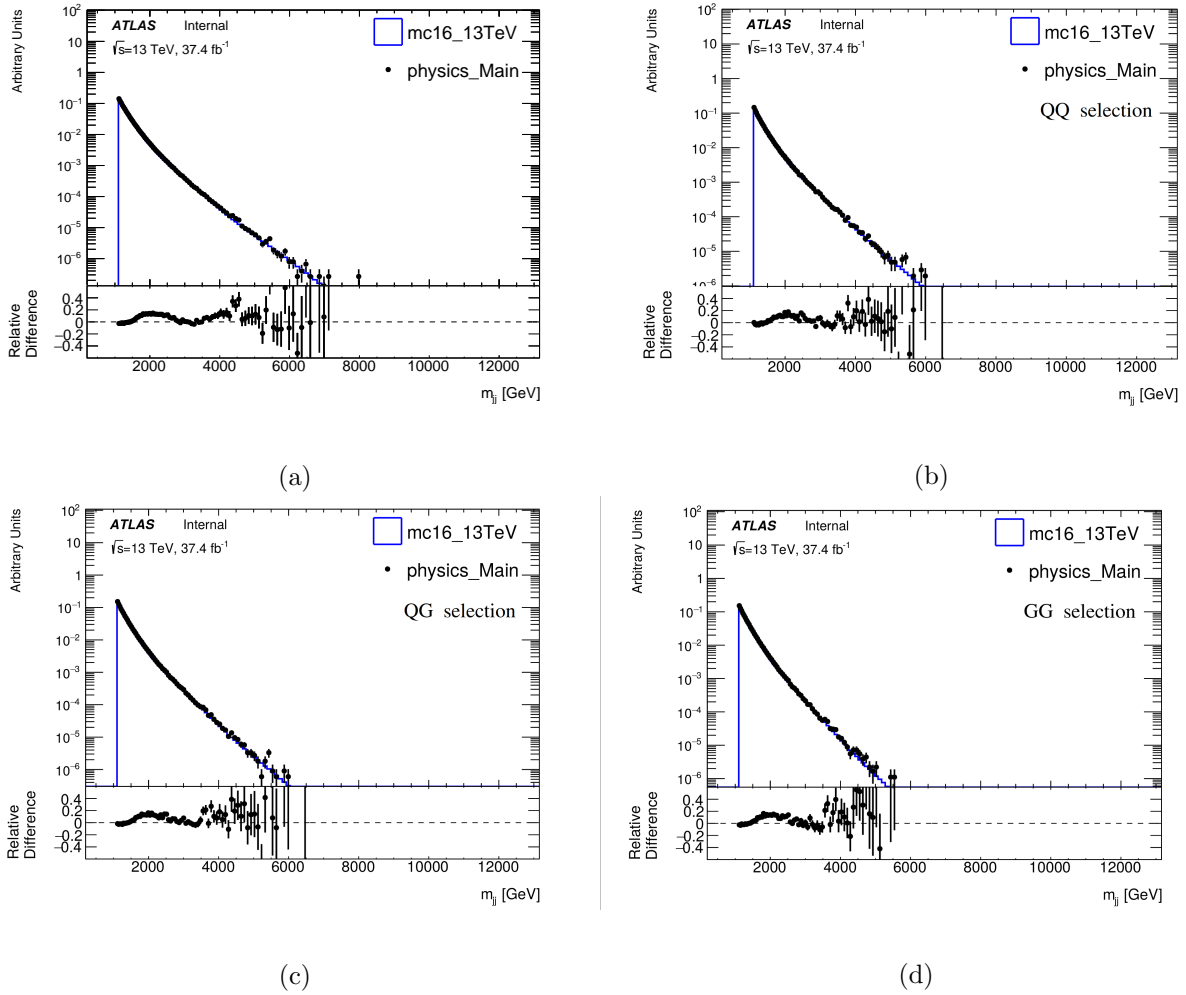


Figure 7.1: Data/MC comparison of  $m_{jj}$  distributions for (a) all events, (b) QQ tagged events, (c) QG tagged events, and (d) GG tagged events. Jets used in these plots were tagged using the  $Sel_{\text{Loose}}^{QG}$  selection.

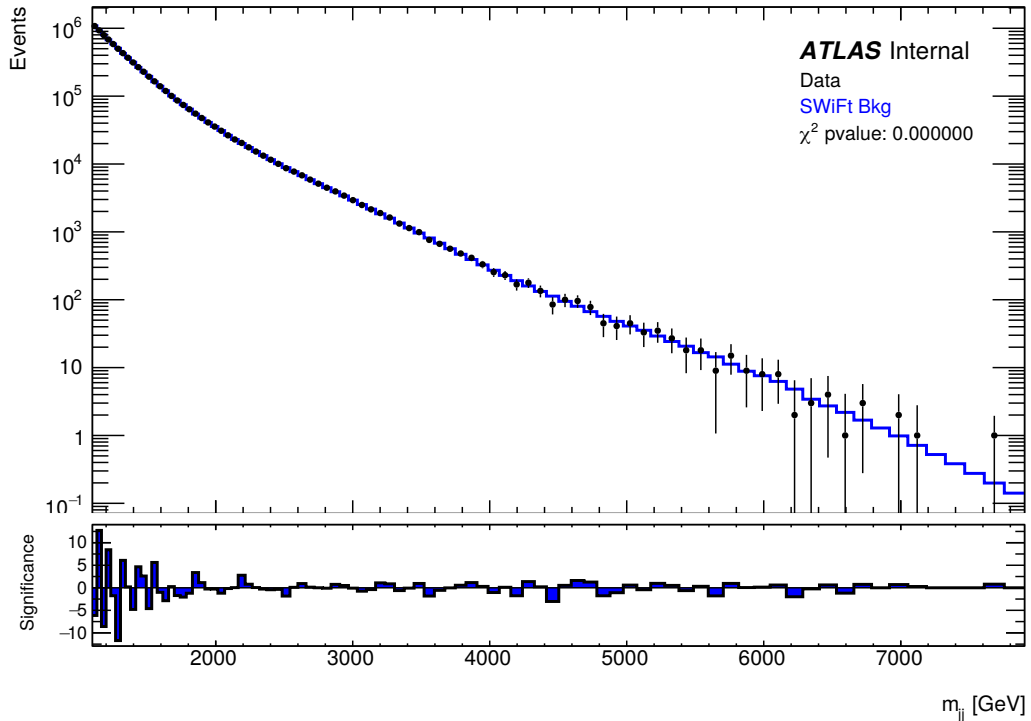


Figure 7.2: SWIFT background obtained from untagged PYTHIA sample.

Unfortunately, the HistFitter program encountered difficulty with some of the fits failing to converge. This prevented me from producing cross section limits for several of the selections. The plots in Figures 7.3a and 7.3b represent the best limits obtained from the subset that succeeded. It is anticipated that better limits could be obtained with further refinements. This includes a better understanding of the  $q^*$  modelling, and consideration of the appropriate significance calculations. Even with these limitations, an improvement in cross section limits is observed for the  $Sel_{\text{Loose}}^{QG}$  selection at high mass.

Limits obtained for the  $H'$  signal are shown in Figure 7.5. These are produced using a  $\sim 90\%$  gluon-jet selection efficiency. The expected significance shown in Fig. 6.9 suggests this is the optimum selection. Unlike the QG tagging of the excited quark samples, the GG tagging shows consistent improvement in the obtained limits. The selection used to obtain these limits is based on Equation 7.6,

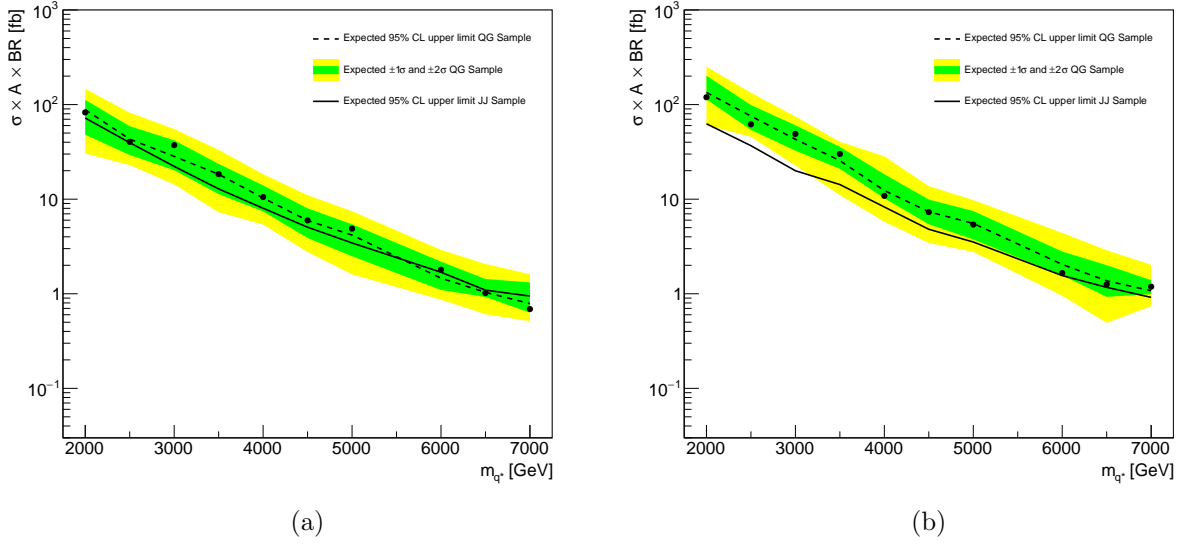


Figure 7.3: Upper limit to the cross section  $\times$  acceptance  $\times$  branching ratio obtained from the QG selection for the  $q^*$  signal (green and yellow bands) compared to no selection (solid line). Possible improvements to the limits are seen above 6 TeV in (a) the loose selection,  $Sel_{Loose}^{QG}$ . No improvements are seen with (b) the tight selection  $Sel_{Tight}^{QG}$ .

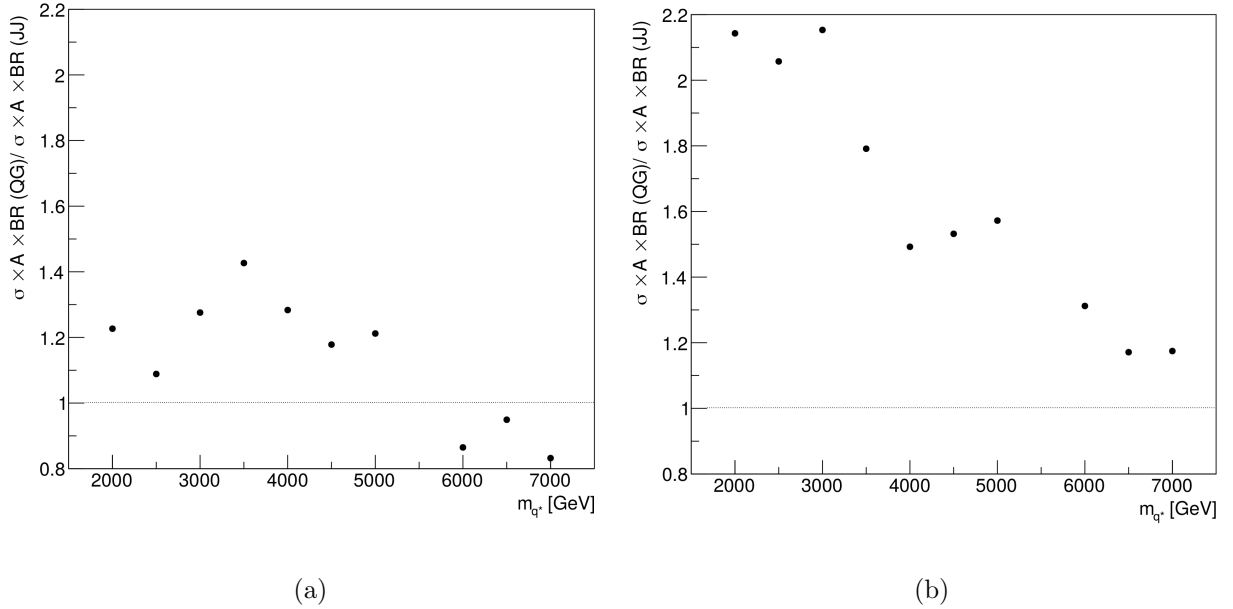


Figure 7.4: Ratio of cross section  $\times$  acceptance  $\times$  branching ratio obtained from the (a)  $Sel_{Loose}^{QG}$  and (b)  $Sel_{Tight}^{QG}$  QG selections and JJ selection for the  $q^*$  signal.

$$n_q = n_g = \text{int}[3.59 \ln(p_T) - 7.55] \quad (7.6)$$

The cross section improvements are significant from 3.5 TeV to 7 TeV, where improvements start to become harder due to a lack of data.

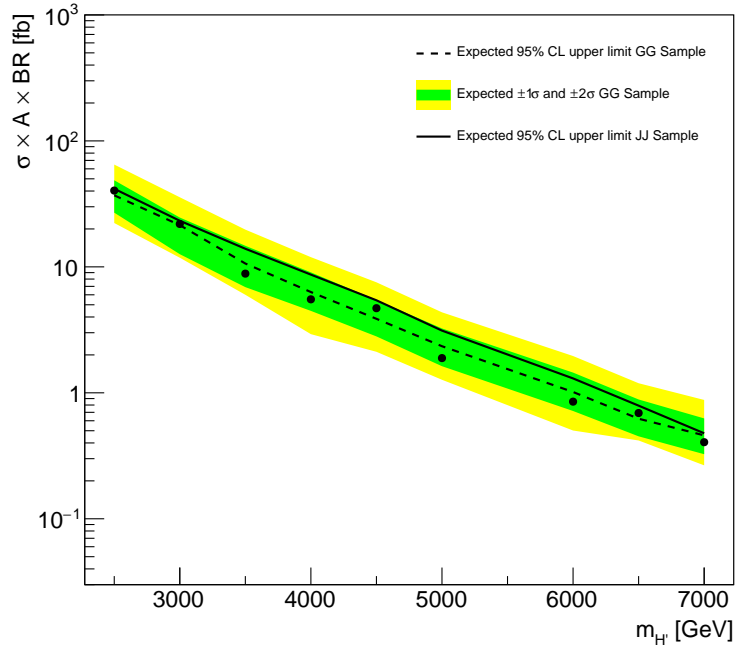


Figure 7.5: Upper limit to the cross section  $\times$  acceptance  $\times$  branching ratio obtained from the GG selection for the  $H'$  signal (green and yellow bands) compared to no selection (solid line). Limits are improved across the mass range.

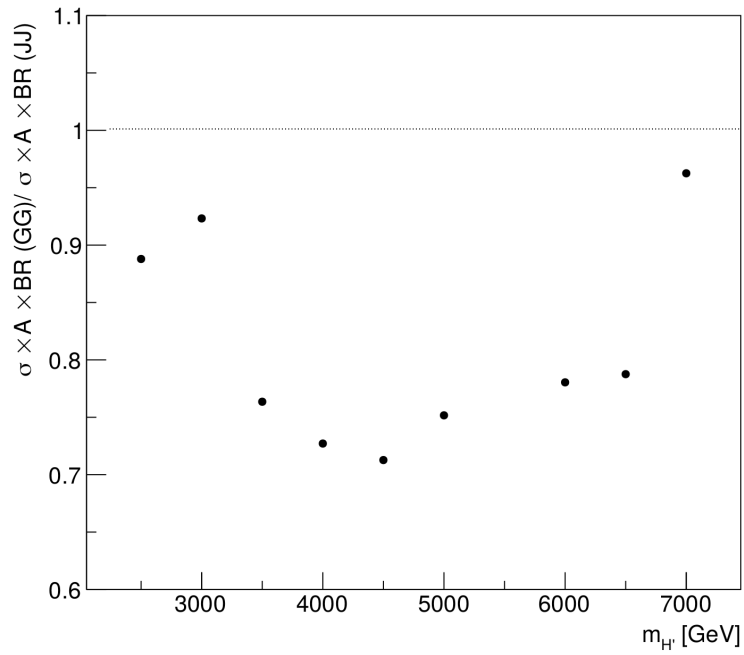


Figure 7.6: Ratio of cross section  $\times$  acceptance  $\times$  branching ratio obtained from the GG selection and JJ selection for the  $H'$  signal.

## Chapter 8

# Conclusion

This thesis has presented a first look at implementing quark-gluon tagging in a high mass dijet search. In such a high- $p_T$  regime, the discriminating power of a simple cut on charged track multiplicity has been shown to provide improved cross section limits for the signal models considered. This follows previous work into tagging jets at low- $p_T$ . Expected limits have been obtained for both an excited quark signal decaying to a qg final state, and a singlet scalar model decaying to a gg final state.

The excited quark limits show slight improvements over previous methods using the untagged dijet mass spectrum, of  $\sim 10\%$  at masses over 6 TeV, whilst far more significant improvements are found at high mass with the singlet scalar model.

Limitations to this analysis include the lack of quark-gluon tagging specific systematic uncertainties extending to the high- $p_T$  regime. Studies into this are ongoing, and should provide a clear indication into the benefits of quark-gluon tagging. Even so, improvements to the interaction cross section limits of  $\sim 30\%$  are observed in some mass bins, suggesting that even with these additional uncertainties, QG tagging can be especially useful for a gg final state model. Further optimisations are likely possible through consideration of the significance obtained with different selections.

This thesis represents the first work aimed at applying quark-gluon tagging to the dijet

search, and as such, there are many improvements which have been suggested. Originally part of the high mass dijet search team, this work has proved far more complex, and a new group has been set up to investigate and implement these changes. Discovered during the analysis was the inability of current PYTHIA generators to reproduce accurate  $q^*$  hadronisation due to the presence of colour dipoles. With updated PYTHIA generators now available, it should be possible to validate this approach and produce reliable cross section limits for this model. If these models behave as expected, and the separation of the quark and gluon jets is increased, improved results over those presented here should be possible with newer selection criteria.

Additional motivation for tagging comes from benchmark signals decaying to two quarks, such as new massive  $Z'$  bosons. Since gluon-initiated jets dominate the background at low- $m_{jj}$ , it would be expected that quark-gluon tagging could improve cross section limits at low masses. Additional signal models such as this are therefore being investigated.

As the LHC prepares to enter a period of higher luminosity, the increased statistics available promise to improve the limits obtained, especially at high- $m_{jj}$ . This is where quark-initiated jets dominate the background, and the significance calculations suggest  $qg$  and  $gg$  final state models will benefit especially from quark-gluon tagging in this regime.

# Bibliography

- [1] U. Baur, M. Spira, and P. M. Zerwas. Excited-quark and -lepton production at hadron colliders. *Phys. Rev. D*, 42:815–824, Aug 1990.
- [2] ATLAS collaboration. Approved Tile Calorimeter Plots (Cosmics/Single beam, Calibrations, Testbeam, Upgrades). <https://twiki.cern.ch/twiki/bin/view/AtlasPublic/ApprovedPlotsTile>, 2008.
- [3] The ATLAS Collaboration. Selection of jets produced in 13TeV proton-proton collisions with the ATLAS detector. Technical Report ATLAS-CONF-2015-029, CERN, Geneva, Jul 2015.
- [4] ATLAS Collaboration. Quark versus Gluon Jet Tagging Using Charged Particle Multiplicity with the ATLAS Detector. Technical Report ATL-PHYS-PUB-2017-009, CERN, Geneva, May 2017.
- [5] Georges Aad et al. Measurement of the charged-particle multiplicity inside jets from  $\sqrt{s} = 8$  TeV  $pp$  collisions with the ATLAS detector. *Eur. Phys. J.*, C76(6):322, 2016.
- [6] HEPData. Durham high-energy physics database. <https://www.hepdata.net>.
- [7] Vera C. Rubin and W. Kent Ford, Jr. Rotation of the Andromeda Nebula from a Spectroscopic Survey of Emission Regions. *Astrophys. J.*, 159:379–403, 1970.
- [8] E. Eichten, I. Hinchliffe, K. Lane, and C. Quigg. Supercollider physics. *Rev. Mod. Phys.*, 56:579–707, Oct 1984.

- [9] The ATLAS Collaboration. Search for new phenomena in dijet events using  $37 \text{ fb}^{-1}$  of pp collision data collected at  $s = 13 \text{ TeV}$  with the ATLAS detector. *Phys Rev D*, 2017.
- [10] U. Baur, I. Hinchliffe, and D. Zeppenfeld. Excited quark production at hadron colliders. *Int. J. Mod. Phys.*, A2:1285, 1987.
- [11] ATLAS and CMS collaborations. ATLAS and CMS physics results from Run 2. <https://indico.cern.ch/event/442432>.
- [12] Yuichiro Nakai, Ryosuke Sato, and Kohsaku Tobioka. Footprints of New Strong Dynamics via Anomaly and the 750 GeV Diphoton. *Phys. Rev. Lett.*, 116(15):151802, 2016.
- [13] Georg G. Raffelt. Astrophysical axion bounds. *Lect. Notes Phys.*, 741:51–71, 2008. [,51(2006)].
- [14] R. M. Harris and K Kousouris. Searches for dijet resonances at hadron colliders. *Int. J. Mod. Phys. A*, 26:5005, 2011.
- [15] Jason Gallicchio and Matthew D. Schwartz. Quark and Gluon Jet Substructure. *JHEP*, 04:090, 2013.
- [16] Daniele Amati and Gabriele Veneziano. Preconfinement as a property of perturbative QCD. *Phys. Lett. B*, 83(CERN-TH-2620):87–92. 13 p, Feb 1979.
- [17] B. R. Webber. Fragmentation and hadronization. *Int. J. Mod. Phys.*, A15S1:577–606, 2000. [eConfC990809,577(2000)].
- [18] Stefan Gieseke, Frashër Loshaj, and Patrick Kirchgaerber. Soft and diffractive scattering with the cluster model in Herwig. *Eur. Phys. J.*, C77(3):156, 2017.
- [19] B. Andersson, G. Gustafson, G. Ingelman, and T. Sjöstrand. Parton fragmentation and string dynamics. *Physics Reports*, 97(2):31 – 145, 1983.

- [20] Torbjörn Sjöstrand, Stefan Ask, Jesper R. Christiansen, Richard Corke, Nishita Desai, Philip Ilten, Stephen Mrenna, Stefan Prestel, Christine O. Rasmussen, and Peter Z. Skands. An Introduction to PYTHIA 8.2. *Comput. Phys. Commun.*, 191:159–177, 2015.
- [21] Bo Andersson, G. Gustafson, G. Ingelman, and T. Sjostrand. Parton Fragmentation and String Dynamics. *Phys. Rept.*, 97:31–145, 1983.
- [22] Torbjorn Sjostrand. Jet Fragmentation of Nearby Partons. *Nucl. Phys.*, B248:469–502, 1984.
- [23] A Banfi et al Science & Technology Facilities Council. Lecture notes for the 2016 HEP School for Experimental High Energy Physics Students RAL-TR-2016-007. <http://purl.org/net/epubs/work/30198951>, 2016.
- [24] Gavin P. Salam. Towards Jetography. *Eur. Phys. J.*, C67:637–686, 2010.
- [25] Stephen D. Ellis, Zoltan Kunszt, and Davison E. Soper. One-jet inclusive cross section at order  $\alpha_s^3$ . gluons only. *Phys. Rev. D*, 40:2188–2222, Oct 1989.
- [26] John E. Huth et al. Toward a standardization of jet definitions. In *1990 DPF Summer Study on High-energy Physics: Research Directions for the Decade (Snowmass 90) Snowmass, Colorado, June 25-July 13, 1990*, pages 0134–136, 1990.
- [27] George Sterman and Steven Weinberg. Jets from quantum chromodynamics. *Phys. Rev. Lett.*, 39:1436–1439, Dec 1977.
- [28] M.H. Seymour. Jet shapes in hadron collisions: Higher orders, resummation and hadronization. *Nuclear Physics B*, 513(1-2):269–300, Mar 1998.
- [29] Ryan Atkin. Review of jet reconstruction algorithms. *JoP Conf. Ser.*, 645(012008), 2015.

- [30] Matteo Cacciari, Gavin P. Salam, and Gregory Soyez. The anti- $k_t$  jet clustering algorithm. *JHEP*, 04:063, 2008.
- [31] Matteo Cacciari and Gavin P. Salam. Dispelling the  $n^3$  myth for the  $k_t$  jet-finder. *Phys Let B*, 57(641), August 2006.
- [32] G. Corcella, I. G. Knowles, G. Marchesini, S. Moretti, K. Odagiri, P. Richardson, M. H. Seymour, and B. R. Webber. HERWIG 6.5 release note. Technical report, CAVENDISH-HEP-02-17, DAMTP-2002-124, KEK-TH-850, MPI-PHT-2002-55, CERN-TH-2002-270, IPPP-02-58, MC-TH-2002-7, 2002.
- [33] Guido Altarelli and G. Parisi. Asymptotic Freedom in Parton Language. *Nucl. Phys.*, B126:298–318, 1977.
- [34] Christopher Frye, Andrew J. Larkoski, Jesse Thaler, and Kevin Zhou. Casimir Meets Poisson: Improved Quark/Gluon Discrimination with Counting Observables. *JHEP*, 09:083, 2017.
- [35] Marek Tasevsky. Differences between quark and gluon jets as seen at LEP. In *New trends in high-energy physics: Experiment, phenomenology, theory. Proceedings, International Conference, Yalta, Crimea, Ukraine, September 22-29, 2001*, pages 116–126, 2001.
- [36] D. Buskulic et al. Quark and gluon jet properties in symmetric three-jet events. *Physics Letters B*, 384(1):353 – 364, 1996.
- [37] Oliver Sim Brüning, Paul Collier, P Lebrun, Stephen Myers, Ranko Ostojic, John Poole, and Paul Proudlock. *LHC Design Report*. CERN Yellow Reports: Monographs. CERN, Geneva, 2004.
- [38] The ATLAS Collaboration. Luminosity determination in  $pp$  collisions at  $\sqrt{s} = 13$  TeV using the ATLAS detector at the LHC. Technical Report ATLAS-CONF-2019-021, CERN, Geneva, Jun 2019.

- [39] S van der Meer. Calibration of the effective beam height in the ISR. Technical Report CERN-ISR-PO-68-31. ISR-PO-68-31, CERN, Geneva, 1968.
- [40] P. Grafström and W. Kozanecki. Luminosity determination at proton colliders. *Progress in Particle and Nuclear Physics*, 81:97 – 148, 2015.
- [41] G. Avoni, M. Bruschi, G. Cabras, D. Caforio, N. Dehghanian, A. Floderus, B. Giacobbe, F. Giannuzzi, F. Giorgi, P. Grafström, V. Hedberg, F. Lasagni Manghi, S. Meneghini, J. Pinfold, E. Richards, C. Sbarra, N. Semprini Cesari, A. Sbrizzi, R. Soluk, G. Uccielli, S. Valentinetti, O. Viazlo, M. Villa, C. Vittori, R. Vuillermet, and A. Zoccoli. The new LUCID-2 detector for luminosity measurement and monitoring in ATLAS. *Journal of Instrumentation*, 13(07):P07017–P07017, jul 2018.
- [42] G. Aad et al. The ATLAS Experiment at the CERN Large Hadron Collider. *JINST*, 3:S08003, 2008.
- [43] The ATLAS Collaboration. Luminosity Public Results Run 2. <https://twiki.cern.ch/twiki/bin/view/AtlasPublic/LuminosityPublicResultsRun2>. Accessed: 2019-06-10.
- [44] Lyndon Evans and Philip Bryant. LHC Machine. *JINST*, 3:S08001, 2008.
- [45] Joao Pequeno. Computer generated image of the whole ATLAS detector. accessed 21-12-2019, Mar 2008.
- [46] M.L Andrieux et al. Construction and test of the first two sectors of the atlas barrel liquid argon presampler. *Nuclear Instruments and Methods in Physics Research Section A: Accelerators, Spectrometers, Detectors and Associated Equipment*, 479(2):316 – 333, 2002.
- [47] M Aleksa et al. Construction, assembly and tests of the ATLAS electromagnetic end-cap calorimeters. *Journal of Instrumentation*, 3(06):P06002–P06002, jun 2008.

- [48] Claude Leroy and Pier-Giorgio Rancoita. *Principles of Radiation Interaction in Matter and Detection*. WORLD SCIENTIFIC, 2nd edition, 2009.
- [49] L. Cerda Alberich. Calibration and performance of the ATLAS tile calorimeter during the LHC run 2. *Journal of Instrumentation*, 13(02):C02031–C02031, feb 2018.
- [50] K. Anderson, A. Gupta, F. Merritt, M. Oreglia, J. Pilcher, H. Sanders, M. Shochet, F. Tang, R. Teuscher, H. Wu, G. Blanchot, M. Cavalli-Sforza, and I. Korolkov. Design of the front-end analog electronics for the ATLAS tile calorimeter. *Nuclear Instruments and Methods in Physics Research Section A: Accelerators, Spectrometers, Detectors and Associated Equipment*, 551(2):469 – 476, 2005.
- [51] E Starchenko, G Blanchot, M Bosman, M Cavalli-Sforza, A Karyukhin, S Kopikov, A Miagkov, M Nessi, A Shalimov, N Shalanda, M Soldatov, A Solodkov, A Soloviev, V Tsoupko-Sitnikov, and A Zaitsev. Cesium monitoring system for ATLAS Tile Hadron Calorimeter. *Nuclear Instruments and Methods in Physics Research Section A: Accelerators, Spectrometers, Detectors and Associated Equipment*, 494(1):381 – 384, 2002. Proceedings of the 8th International Conference on Instrumentation for Colliding Beam Physics.
- [52] J. Abdallah et al. The Laser calibration of the ATLAS Tile Calorimeter during the LHC run 1. *JINST*, 11(10):T10005, 2016.
- [53] Georges Aad et al. Improved luminosity determination in pp collisions at  $\sqrt{s} = 7$  TeV using the ATLAS detector at the LHC. *Eur. Phys. J.*, C73(8):2518, 2013.
- [54] P. Adragna et al. Testbeam studies of production modules of the ATLAS Tile Calorimeter. *Nuclear Instruments and Methods in Physics Research Section A: Accelerators, Spectrometers, Detectors and Associated Equipment*, 606(3):362 – 394, 2009.

- [55] Aad et al. Technical Design Report for the Phase-I Upgrade of the ATLAS TDAQ System. Technical Report CERN-LHCC-2013-018. ATLAS-TDR-023, CERN, Sep 2013. Final version presented to December 2013 LHCC.
- [56] The ATLAS Collaboration. Search for New Phenomena in Dijet Events using  $139 \text{ fb}^{-1}$  of  $pp$  collisions at  $\sqrt{s} = 13\text{TeV}$  collected with the ATLAS Detector. Technical Report ATLAS-CONF-2019-007, CERN, Geneva, Mar 2019.
- [57] G. Aad, B. Abbott, Jasmin Abdallah, Ahmed Abdelalim, Abdesselam Abdelouahab, O. Abdinov, B. Abi, M. Abolins, H. Abramowicz, Heather Abreu, E. Acerbi, Bobby Acharya, M. Ackers, D.L. Adams, Tetteh Addy, J. Adelman, M. Aderholz, S. Adomeit, C. Adorisio, and Jennifer Alison. Search for quark contact interactions in dijet angular distributions in  $pp$  collisions at  $s=7 \text{ TeV}$  measured with the ATLAS detector. *Physics Letters B*, 694:327–345, 01 2011.
- [58] G. Aad et al. Data quality from the detector control system at the ATLAS experiment. *J. Phys. Conf. Ser.*, 219:022037, 2010.
- [59] Georges Aad et al. Topological cell clustering in the ATLAS calorimeters and its performance in LHC Run 1. *Eur. Phys. J.*, C77:490, 2017.
- [60] W Lampl, S Laplace, D Lelas, P Loch, H Ma, S Menke, S Rajagopalan, D Rousseau, S Snyder, and G Unal. Calorimeter Clustering Algorithms: Description and Performance. Technical Report ATL-LARG-PUB-2008-002. ATL-COM-LARG-2008-003, CERN, Geneva, Apr 2008.
- [61] Matteo Cacciari, Gavin P. Salam, and Gregory Soyez. FastJet User Manual. *Eur. Phys. J.*, C72:1896, 2012.
- [62] Matteo Cacciari and Gavin P. Salam. Dispelling the  $N^3$  myth for the  $k_t$  jet-finder. *Phys. Lett.*, B641:57–61, 2006.

- [63] M. Aaboud et al. Jet energy scale measurements and their systematic uncertainties in proton-proton collisions at  $\sqrt{s} = 13$  TeV with the ATLAS detector. *Phys. Rev.*, D96(7):072002, 2017.
- [64] Georges Aad et al. Performance of pile-up mitigation techniques for jets in  $pp$  collisions at  $\sqrt{s} = 8$  TeV using the ATLAS detector. *Eur. Phys. J.*, C76(11):581, 2016.
- [65] Matteo Cacciari and Gavin P. Salam. Pileup subtraction using jet areas. *Phys. Lett.*, B659:119–126, 2008.
- [66] The ATLAS collaboration. Jet Calibration and Systematic Uncertainties for Jets Reconstructed in the ATLAS Detector at  $\sqrt{s} = 13$  TeV. Technical Report ATL-PHYS-PUB-2015-015, CERN, Geneva, Jul 2015.
- [67] Georges Aad et al. Jet energy measurement and its systematic uncertainty in proton-proton collisions at  $\sqrt{s} = 7$  TeV with the ATLAS detector. *Eur. Phys. J.*, C75:17, 2015.
- [68] Georges Aad et al. Jet energy measurement with the ATLAS detector in proton-proton collisions at  $\sqrt{s} = 7$  TeV. *Eur. Phys. J.*, C73(3):2304, 2013.
- [69] The ATLAS Collaboration. JES Public Plots for Moriond 2017. <https://atlas.web.cern.ch/Atlas/GROUPS/PHYSICS/PLOTS/JETM-2017-003/>.
- [70] Georges Aad et al. Muon reconstruction performance of the ATLAS detector in proton-proton collision data at  $\sqrt{s} = 13$  TeV. *Eur. Phys. J.*, C76(5):292, 2016.
- [71] Georges Aad et al. Electron and photon energy calibration with the ATLAS detector using LHC Run 1 data. *Eur. Phys. J.*, C74(10):3071, 2014.
- [72] Coll ATLAS, M Beckingham, M Duehrssen, E Schmidt, M Shapiro, M Venturi, J Virzi, I Vivarelli, M Werner, S Yamamoto, and T Yamanaka. The simulation principle and performance of the ATLAS fast calorimeter simulation FastCaloSim. Technical Report ATL-PHYS-PUB-2010-013, CERN, Geneva, Oct 2010.

- [73] S. Agostinelli et al. Geant4—a simulation toolkit. *Nuclear Instruments and Methods in Physics Research Section A: Accelerators, Spectrometers, Detectors and Associated Equipment*, 506(3):250 – 303, 2003.
- [74] Morad Aaboud et al. A measurement of the calorimeter response to single hadrons and determination of the jet energy scale uncertainty using LHC Run-1  $pp$ -collision data with the ATLAS detector. *Eur. Phys. J.*, C77(1):26, 2017.
- [75] P. Bagnaia, M. Banner, R. Battiston, P. Bloch, K. Borer, M. Borghini, J. Bürger, P. Cenci, J.-C. Chollet, A. G. Clark, C. Conta, P. Darriulat, L. Di Lella, J. Dines-Hansen, R. Engelmann, L. Fayard, M. Fraternali, D. Froidevaux, J.-M. Gaillard, O. Gildemeister, V. G. Goggi, C. Gössling, B. Hahn, H. Hänni, J. R. Hansen, P. Hansen, N. Harnew, T. Himel, P. Jenni, O. Kofoed-Hansen, E. Lançon, M. Livan, S. Loucatos, B. Madsen, P. Mani, B. Mansoulié, G. C. Mantovani, L. Mapelli, B. Merkel, R. Mollerud, C. Onions, G. Parrou, F. Pastore, H. Plochow-Besch, M. Polverel, J.-P. Repellin, A. Rothenberg, A. Roussarie, G. Sauvage, J. Schacher, J. L. Siegrist, G. Stimpfl, F. Stocker, M. Swartz, J. Teiger, S. Tovey, V. Vercesi, A. R. Weidberg, H. Zaccane, J. A. Zakrzewski, W. Zeller, and UA2 Collaboration. Measurement of jet production properties at the CERN  $\bar{p}p$  Collider. *Physics Letters B*, 144:283–290, August 1984.
- [76] Georges Aad et al. Jet energy resolution in proton-proton collisions at  $\sqrt{s} = 7$  TeV recorded in 2010 with the ATLAS detector. *Eur. Phys. J.*, C73(3):2306, 2013.
- [77] G Romeo, A Schwartzman, R Piegaglia, T Carli, and R Teuscher. Jet Energy Resolution from In-situ Techniques with the ATLAS Detector Using Proton-Proton Collisions at a Center of Mass Energy  $\sqrt{s} = 7$  TeV. Technical Report ATL-COM-PHYS-2011-240, CERN, Geneva, Mar 2011.
- [78] Julia Gonski. Jet Cleaning in 2016 and the Event Level Cleaning Tool. Technical Report ATL-COM-PHYS-2017-982, CERN, Geneva, Jun 2017.

- [79] Georges Aad et al. Characterisation and mitigation of beam-induced backgrounds observed in the ATLAS detector during the 2011 proton-proton run. *JINST*, 8:P07004, 2013.
- [80] G. Aad et al. Readiness of the ATLAS Liquid Argon Calorimeter for LHC Collisions. *Eur. Phys. J.*, C70:723–753, 2010.
- [81] The ATLAS Collaboration. ATLAS Run 1 PYTHIA8 tunes. Technical Report ATL-PHYS-PUB-2014-021, CERN, Geneva, Nov 2014.
- [82] J. Pumplin, D. R. Stump, J. Huston, H. L. Lai, Pavel M. Nadolsky, and W. K. Tung. New generation of parton distributions with uncertainties from global QCD analysis. *JHEP*, 07:012, 2002.
- [83] G. Watt and R. S. Thorne. Study of Monte Carlo approach to experimental uncertainty propagation with MSTW 2008 PDFs. *JHEP*, 08:052, 2012.
- [84] Stefano Carrazza, Stefano Forte, and Juan Rojo. Parton Distributions and Event Generators. In *Proceedings, 43rd International Symposium on Multiparticle Dynamics (ISMD 13)*, pages 89–096, 2013.
- [85] Amanda M. Cooper-Sarkar. HERAPDF1.5LO PDF Set with Experimental Uncertainties. *PoS*, DIS2014:032, 2014.
- [86] The ATLAS Collaboration. ATLAS tunes of PYTHIA6 and PYTHIA8 for MC11. Technical Report ATL-PHYS-PUB-2011-009, CERN, Geneva, Jul 2011.
- [87] Georges Aad et al. Properties of jets measured from tracks in proton-proton collisions at center-of-mass energy  $\sqrt{s} = 7$  TeV with the ATLAS detector. *Phys. Rev.*, D84:054001, 2011.
- [88] Georges Aad et al. Jet mass and substructure of inclusive jets in  $\sqrt{s} = 7$  TeV  $pp$  collisions with the ATLAS experiment. *JHEP*, 05:128, 2012.

- [89] 1974 CERN School of Computing, Godoyssund, Norway, 11-24 Aug 1974: Proceedings. <http://www.slac.stanford.edu/spires/find/books/www?cl=QA76:C2:1974>, 1974.
- [90] Georges Aad et al. Search for new phenomena in dijet mass and angular distributions from  $pp$  collisions at  $\sqrt{s} = 13$  TeV with the ATLAS detector. *Phys. Lett.*, B754:302–322, 2016.
- [91] T. Aaltonen et al. Search for new particles decaying into dijets in proton-antiproton collisions at  $s^{**}(1/2) = 1.96$ -TeV. *Phys. Rev.*, D79:112002, 2009.
- [92] G. Aad et al. Search for New Particles in Two-Jet Final States in 7 TeV Proton-Proton Collisions with the ATLAS Detector at the LHC. *Phys. Rev. Lett.*, 105:161801, 2010.
- [93] Serguei Chatrchyan et al. Search for Resonances in the Dijet Mass Spectrum from 7 TeV  $pp$  Collisions at CMS. *Phys. Lett.*, B704:123–142, 2011.
- [94] Georges Aad et al. Search for New Physics in Dijet Mass and Angular Distributions in  $pp$  Collisions at  $\sqrt{s} = 7$  TeV Measured with the ATLAS Detector. *New J. Phys.*, 13:053044, 2011.
- [95] Albert M Sirunyan et al. Search for dijet resonances in proton–proton collisions at  $\sqrt{s} = 13$  TeV and constraints on dark matter and other models. *Phys. Lett.*, B769:520–542, 2017. [Erratum: *Phys. Lett.*B772,882(2017)].
- [96] Georges Aad et al. Search for new phenomena in the dijet mass distribution using  $p-p$  collision data at  $\sqrt{s} = 8$  TeV with the ATLAS detector. *Phys. Rev.*, D91(5):052007, 2015.
- [97] The ATLAS Collaboration. Search for light dijet resonances with the ATLAS detector using a Trigger-Level Analysis in LHC  $pp$  collisions at  $\sqrt{s} = 13$  TeV. Technical Report ATLAS-CONF-2016-030, CERN, Geneva, Jun 2016.

- [98] Karishma Sekhon, Ryan Christopher Edgar, and Dante Amidei. SWiFt: Sliding Window Fit Method for Resonance Searches. Technical Report ATL-COM-PHYS-2018-161, CERN, Geneva, Feb 2018.
- [99] Karishma Sekhon. *Search for New Particles Decaying to Hadronic Jets in Proton-Proton Collision at  $\sqrt{s} = 13$  TeV*. PhD thesis, Michigan State U, May 2018. Presented 04 May 2018.
- [100] F James and M Roos. MINUIT—a system for function minimization and analysis of the parameter errors and correlations. *Comput. Phys. Commun.*, 10(6):343–67, 1975.
- [101] J. A. Nelder and R. Mead. A Simplex Method for Function Minimization. *The Computer Journal*, 7(4):308–313, 01 1965.
- [102] W. C. Davidon. Variable metric method for minimization. *SIAM Journal on Optimization*, 1(1):1–17, 1990.
- [103] Helen Brooks and Peter Skands. Coherent showers in decays of colored resonances. *Phys. Rev.*, D100(7):076006, 2019.
- [104] Torbjorn Sjostrand, Stephen Mrenna, and Peter Z. Skands. A Brief Introduction to PYTHIA 8.1. *Comput. Phys. Commun.*, 178:852–867, 2008.
- [105] Jun Gao, Marco Guzzi, Joey Huston, Hung-Liang Lai, Zhao Li, Pavel Nadolsky, Jon Pumplin, Daniel Stump, and C.-P. Yuan. Ct10 next-to-next-to-leading order global analysis of qcd. *Phys. Rev. D*, 89:033009, Feb 2014.
- [106] Manuel Bähr, Stefan Gieseke, and Michael H Seymour. Simulation of multiple partonic interactions in herwig++. *Journal of High Energy Physics*, 2008(07):076–076, jul 2008.
- [107] Pavel M. Nadolsky, Hung-Liang Lai, Qing-Hong Cao, Joey Huston, Jon Pumplin, Daniel Stump, Wu-Ki Tung, and C.-P. Yuan. Implications of CTEQ global analysis for collider observables. *Phys. Rev. D*, 78:013004, Jul 2008.

- [108] Andy Buckley, James Ferrando, Stephen Lloyd, Karl Nordström, Ben Page, Martin Rüfenacht, Marek Schönherr, and Graeme Watt. LHAPDF6: parton density access in the LHC precision era. *The European Physical Journal C*, 75(3):132, Mar 2015.
- [109] The ATLAS Collaboration. Example ATLAS tunes of PYTHIA8, PYTHIA6 and Powheg to an observable sensitive to  $Z$  boson transverse momentum. Technical Report ATL-PHYS-PUB-2013-017, CERN, Geneva, Nov 2013.
- [110] Georges Aad et al. Light-quark and gluon jet discrimination in  $pp$  collisions at  $\sqrt{s} = 7$  TeV with the ATLAS detector. *Eur. Phys. J.*, C74(8):3023, 2014.
- [111] The ATLAS Collaboration. Early Inner Detector Tracking Performance in the 2015 data at  $\sqrt{s} = 13$  TeV. Technical Report ATL-PHYS-PUB-2015-051, CERN, Geneva, Dec 2015.
- [112] M. Aaboud et al. Performance of the ATLAS Track Reconstruction Algorithms in Dense Environments in LHC Run 2. *Eur. Phys. J.*, C77(10):673, 2017.
- [113] The ATLAS Collaboration. Study of alignment-related systematic effects on the ATLAS Inner Detector tracking. Technical Report ATLAS-CONF-2012-141, CERN, Geneva, Oct 2012.
- [114] The ATLAS Collaboration. Alignment Performance of the ATLAS Inner Detector Tracking System in 7 TeV proton-proton collisions at the LHC. Technical Report ATLAS-CONF-2010-067, CERN, Geneva, Jul 2010.
- [115] The ATLAS Collaboration. Alignment of the ATLAS Inner Detector Tracking System with 2010 LHC proton-proton collisions at  $\sqrt{s} = 7$  TeV. Technical Report ATLAS-CONF-2011-012, CERN, Geneva, Mar 2011.
- [116] A L Read. Modified frequentist analysis of search results (the  $CL_s$  method). In *1st Workshop on Confidence Limits, CERN, Geneva, Switzerland, 17 - 18 Jan 2000*, pp.81-101, 2000.

- [117] A L Read. Presentation of search results: theCLstechnique. *Journal of Physics G: Nuclear and Particle Physics*, 28(10):2693–2704, sep 2002.
- [118] Glen Cowan, Kyle Cranmer, Eilam Gross, and Ofer Vitells. Asymptotic formulae for likelihood-based tests of new physics. *Eur. Phys. J.*, C71:1554, 2011. [Erratum: *Eur. Phys. J.*C73,2501(2013)].
- [119] Gary J. Feldman and Robert D. Cousins. A Unified approach to the classical statistical analysis of small signals. *Phys. Rev.*, D57:3873–3889, 1998.
- [120] G Zech. Upper limits in experiments with background or measurement errors. *Nucl. Instrum. Methods Phys. Res., A*, 277(CERN-EP-88-164):608. 6 p, Nov 1988.
- [121] M. Baak, G. J. Besjes, D. Côte, A. Koutsman, J. Lorenz, and D. Short. HistFitter software framework for statistical data analysis. *Eur. Phys. J.*, C75:153, 2015.